Technical Physics Letters, Vol. 30, No. 7, 2004, pp. 529–531. Translated from Pis’ma v Zhurnal Tekhnicheskoĭ Fiziki, Vol. 30, No. 13, 2004, pp. 1–6.
Original Russian Text Copyright © 2004 by Parkhomenko, Astakhova, Grebenshchikova, Ivanov, Kunitsyna, Yakovlev.

Light-Emitting Diodes Based on $Ga_{1-x}In_xAs_ySb_{1-y}$ Solid Solutions Grown from Lead-Containing Melts

Ya. A. Parkhomenko, A. P. Astakhova, E. A. Grebenshchikova, É. V. Ivanov, E. V. Kunitsyna, and Yu. P. Yakovlev

Ioffe Physicotechnical Institute, Russian Academy of Sciences, St. Petersburg, 194021 Russia
e-mail: www.ioffe.ru

Received February 5, 2004

Abstract—Light-emitting diodes (LEDs) with the maximum emission at λ = 2.3 and 2.44 μm are obtained and characterized. The active region of LEDs is based on $Ga_{1-x}In_xAs_ySb_{1-y}$ solid solutions ($x = 0.21$ and 0.25, respectively) grown by liquid phase epitaxy from lead-containing melts. The room-temperature external quantum yield of the 2.3 and 2.44 μm LEDs is 1.6 and 0.11%, respectively. *© 2004 MAIK “Nauka/Interperiodica”.*

Introduction. In recent years, much effort has been devoted to the development and investigation of semiconductor optoelectronic devices emitting in the middle IR range (2–5 μm). This wavelength interval is of interest for environmental monitoring and in some medical applications.

The most promising materials for both sources and detectors of radiation in the 1.8–3.0 μm wavelength range are multicomponent solid solutions of the $Ga_{1-x}In_xAs_ySb_{1-y}$ type based on gallium antimonide (GaSb). In this solid solution system, it is possible to vary composition at a constant crystal lattice constant, thus controlling the bandgap width and, hence, the working wavelength of devices. The problem of increasing the working wavelength of devices based on $Ga_{1-x}In_xAs_ySb_{1-y}$ solid solutions is still among the most important tasks in optoelectronic technology.

It was established [1, 2] that the density of natural defect complexes $V_{Ga}Ga_{Sb}$ in GaSb- and InAS-based solid solutions can be significantly reduced by growing epitaxial layers of these solutions from lead-containing melts. Lead does not form compounds with other components of the melt and is not included into the solid phase. Previously [3, 4], we have studied the role of lead in the growth of $Ga_{1-x}In_xAs_ySb_{1-y}$ solid solutions. Investigation of the galvanomagnetic properties of undoped, as well as Ge- and Te-doped, $Ga_{1-x}In_xAs_ySb_{1-y}$ solid solutions grown from lead-containing melts confirmed good prospects of using such materials in optoelectronic devices operating in the 1.8–3 μm range.

This Letter reports for the first time on light-emitting diodes (LEDs) with the maximum emission at $\lambda_{max} = 2.3$ and 2.44 μm, based on $Ga_{1-x}In_xAs_ySb_{1-y}$ solid solutions grown from lead-containing melts, and presents the results of investigation of the electroluminescence spectra of these LEDs.

Methods of growth and investigation of LED structures. The LED heterostructures were grown by liquid phase epitaxy (LPE) on *n*- and *p*-type GaSb(100) substrates. The wide-bandgap emitters were obtained using a 2.5-μm-thick layer of GaSb. All layers in the LED heterostructure were matched with respect to the lattice period with GaSb substrate ($\Delta a/a < 1.0 \times 10^{-3}$). Equilibrium values of the molar fractions of solid solution components in the liquid and solid phases for the Pb–InAs–InSb–GaAs–GaSb system for selected growth temperature (560°C) and supercooling (ΔT = 3 K) were calculated as described in [5, 6].

LEDs based on the LPE-grown $Ga_{1-x}In_xAs_ySb_{1-y}$ solid solutions were obtained using conventional photolithographic technology. The mesa (300-μm-diam) and point (100-μm-diam) contacts were formed on the wide-bandgap GaSb layer, and a continuous contact was formed on the GaSb substrate (Fig. 1a). The contacts on *n*- and *p*-type GaSb were made of Cr/Au + Te/Au and Cr/Au + Ge/Au layers, respectively. Finally, 500 × 500-μm chips were mounted in standard TO-18 cases.

The electroluminescence (EL) characteristics of LEDs were studied using an automated setup based on a DK-480 monochromator (CVI Laser Corp., USA) and a liquid-nitrogen-cooled InSb photodiode (Judson Technologies, USA). Signals from the photodetector were processed using a synchronous detection scheme based on an SR 810 lock-in amplifier (SRS Inc., USA). The room-temperature (T = 300 K) EL spectra were measured for LEDs powered by a pulsed current with an on-off ratio of $Q = 2$ at a frequency of 512 Hz.

LEDs with λ_{max} = 2.3 μm. The active region in these LEDs was a 2-μm-thick $Ga_{1-x}In_xAs_ySb_{1-y}$ solid solution layer with the indium content $x = 0.21$ (E_g = 0.53 eV, T = 300 K) grown on a *p*-GaSb(100) substrate. The energy band diagram of the device heterostructure

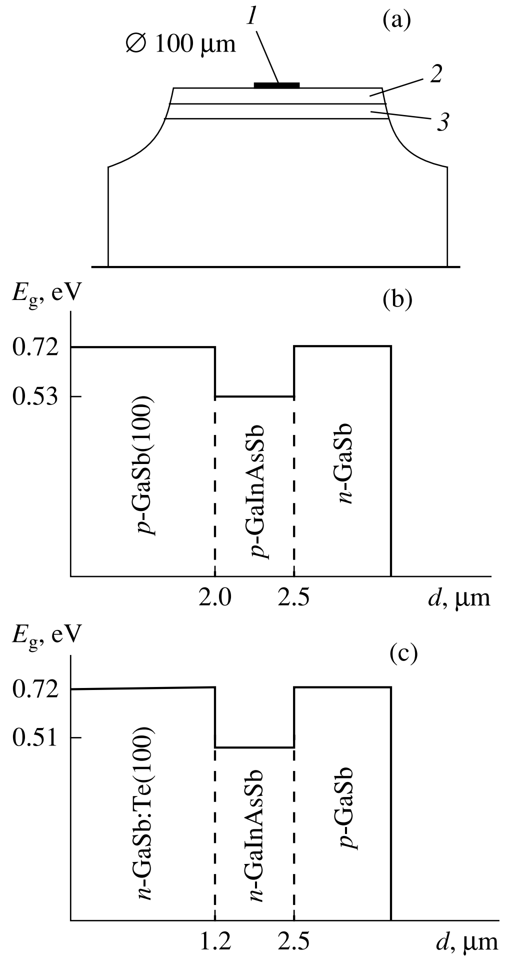

Fig. 1. LEDs based on GaSb/$Ga_{1-x}In_xAs_ySb_{1-y}$/GaSb heterostructures: (a) schematic diagram of a mesa structure showing (*1*) upper contact, (*2*) emitter, and (*3*) active region; (b, c) energy band diagrams of LEDs with the indium content in the active region $x = 0.21$ and 0.25, respectively.

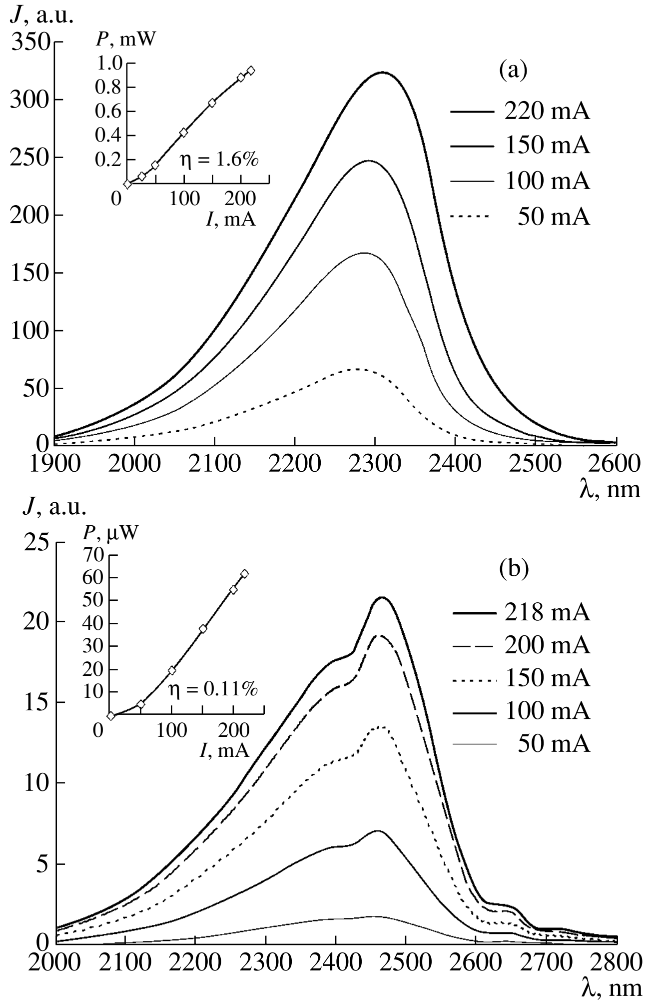

Fig. 2. Room-temperature EL spectra of LEDs with the indium content in the active region $x = 0.21$ (a) and 0.25 (b) measured for various diode currents *I*. The insets show plots of the output emission power *P* versus current *I* for $T = 300$ K.

is depicted in Fig. 1b. The EL spectra with the most intense signals of radiative recombination were obtained for LEDs with undoped active regions. The charge carrier density determined from the Hall effect measurements was $p = 3 \times 10^{18}$ cm^{-3} at $T = 300$ K ($p = 4.6 \times 10^{16}$ cm^{-3} at $T = 77$ K). The upper GaSb layer in these LEDs was doped with tellurium to $n \sim (1–4) \times 10^{18}$ cm^{-3} ($T = 300$ K).

The current–voltage characteristics of these LEDs exhibited a diode character with a room-temperature cutoff voltage of 0.35 V. The serial resistance of direct-biased diodes was ~3.1 Ω.

Figure 2a shows the spectral characteristics of such LEDs measured at $T = 300$ K. As can be seen, the EL spectrum exhibits a single band with the maximum at 2.29 μm ($E_g = 0.54$ eV) at a diode current of $I = 100$ mA. The full width at half maximum (FWHM) of this EL spectrum is 0.20 μm and exhibits growth with the current and reaches 0.23 μm at $I = 220$ mA. The emission maximum slightly shifts toward longer wavelengths with increasing diode current. At a current of 220 mA, the shift amounts to 0.02 μm, which is evidence of an insignificant effect of the current-induced structure heating on the EL characteristics. This conclusion was confirmed by the absence of pronounced saturation in the plot of the integral optical output power versus current (see inset in Fig. 2a) for *I* up to 220 mA, at which the output power reaches 0.937 mW and the external quantum yield is $\eta = 1.6\%$.

LEDs with λ_{max} = 2.44 μm. The active region in these LEDs was a 1.2-μm-thick $Ga_{1-x}In_xAs_ySb_{1-y}$ solid solution layer with the indium content $x = 0.247$ ($E_g = 0.51$ eV, $T = 300$ K) grown on an *n*-GaSb(100) substrate. The energy band diagram of the device heterostructure is depicted in Fig. 1c. The EL spectra with the most intense signals of radiative recombination were observed for LEDs in which the active region was doped with Te to $n = 3 \times 10^{18}$ cm^{-3} ($T = 300$ K). The wide-bandgap emitter was an epitaxial GaSb layer doped with Ge to $p \sim 5 \times 10^{18}$ cm^{-3} ($T = 300$ K).

The current–voltage characteristics of these LEDs exhibited a diode character with a cutoff voltage of 0.4 V at $T = 300$ K. The serial resistance of direct-biased diodes was ~1.7 Ω.

Figure 2b shows the spectral characteristics of such LEDs measured at $T = 300$ K. As can be seen, the EL spectrum exhibit a maximum at 2.44 μm corresponding to the bandgap width in the active region (E_g = 0.51 eV). The FWHM of the EL spectrum measured at $I = 100$ mA was ~0.26 μm. Neither the position nor the FWHM of the emission peak change when the diode current is varied from 50 to 200 mA. This is evidence of the absence of effects related to the current-induced heating of the LED structure. The EL spectrum displays a dip (inflection) at $\lambda \sim 2.42$ μm (Fig. 2b), which is related to a peculiarity in the spectral characteristic of the diffraction grating (300 lines/mm) used for the EL measurements. In addition, there are intense features due to the optical absorption of water and carbon dioxide in the region of 2.6–2.72 μm.

The inset in Fig. 2b shows a plot of the integral optical output power versus current. For $I = 218$ mA, the output power reaches 61.6 μW and the external quantum yield is η = ~0.11%.

Conclusions. We have succeeded for the first time in obtaining LEDs with the maximum emission at $\lambda_{\max} = 2.3$ and 2.44 μm based on $Ga_{1-x}In_xAs_ySb_{1-y}$ solid solution layers grown by LPE from lead-containing melts. The room-temperature external quantum yield of the 2.3 and 2.44 μm LEDs is 1.6 and 0.11%, respectively. These LEDs can find wide use in systems of ecological monitoring and medical diagnostics.

REFERENCES

1. A. N. Baranov, T. I. Voronina, T. S. Lagunova, *et al.*, Fiz. Tekh. Poluprovodn. (Leningrad) **23**, 780 (1989) [Sov. Phys. Semicond. **23**, 490 (1989)].
2. A. M. Grebenyuk, A. M. Litvak, N. A. Charykov, *et al.*, Zh. Neorg. Khim. **35**, 2941 (1990).
3. T. I. Voronina, T. S. Lagunova, E. V. Kunitsyna, *et al.*, Fiz. Tekh. Poluprovodn. (St. Petersburg) **35**, 941 (2001) [Semiconductors **35**, 904 (2001)].
4. T. I. Voronina, T. S. Lagunova, E. V. Kunitsyna, *et al.*, Fiz. Tekh. Poluprovodn. (St. Petersburg) **36**, 917 (2002) [Semiconductors **36**, 855 (2002)].
5. A. M. Litvak and A. N. Charykov, Zh. Fiz. Khim. **64**, 2331 (1990).
6. N. A. Charykov, V. V. Sherstnev, and A. Krier, J. Cryst. Growth **234**, 762 (2002).

Translated by P. Pozdeev

Technical Physics Letters, Vol. 30, No. 7, 2004, pp. 532–534. Translated from Pis’ma v Zhurnal Tekhnicheskoĭ Fiziki, Vol. 30, No. 13, 2004, pp. 7–11.
Original Russian Text Copyright © 2004 by Markov.

Computer Simulation of the Load Characteristics of Low-Temperature Thermoelectric Coolers

O. I. Markov
Orel State Technical University, Orel, Russia
e-mail: Markov@e-mail.ru

Received January 9, 2004

Abstract—The load characteristics of low-temperature thermoelectric coolers have been studied by means of computer simulation using the differential equation of stationary thermal conductivity with temperature-dependent kinetic coefficients. Based on the obtained results, the branches of characteristics of the thermoelements employing bismuth telluride and a bismuth-based superconductor are compared. *© 2004 MAIK “Nauka/Interperiodica”.*

In recent years, increasing effort has been devoted to the creation of thermoelectric coolers for obtaining temperatures below 120 K. The main difficulty encountered in the development of highly effective low-temperature coolers is related to the fact that the thermoelectric efficiency of most thermoelectric materials drops with decreasing temperature. For example, the thermoelectric quality (figure of merit) of a cooler employing bismuth telluride decreases to 0.8×10^{-3} K^{-1} at the boiling temperature of nitrogen. The only thermoelectric material retaining high efficiency at low temperatures is a semiconducting bismuth–antimony solid solution [1]. However, this material ensures high thermoelectric efficiency only for the *n* branch, while no satisfactory results were obtained for the *p* branch. Kuznetsov *et al.* [2] studied the limits of thermoelectric cooling at liquid nitrogen temperature for a system with a bismuth-based superconductor in the passive branch. Unfortunately, the study was restricted to the regime of maximum temperature drop. From the practical standpoint, it would be of interest to study the regime of maximum cold production.

This study was aimed at numerically modeling the load characteristics of low-temperature coolers operating in the regime of maximum cold production. We have also compared the possibilities of coolers employing different thermoelectric materials.

According to the commonly accepted approach [3], the efficiency of a thermoelement is expressed in terms of thermoelectric quality defined as

$$Z = \frac{(\alpha_p - \alpha_n)^2}{[\sqrt{\chi_p \rho_p} + \sqrt{\chi_n \rho_n}]^2}. \qquad (1)$$

Here, α_i, χ_i, and ρ_i ($i = n, p$) are the thermo emf, thermal conductivity, and electric resistivity of the material in the *n* and *p* branches, respectively. It should be noted that the introduction of this parameter is justified only in a rough zero approximation. At low temperatures, where the maximum achievable rate of temperature decrease sharply drops, it is especially important to optimize parameters of the thermoelectric cooler taking into account the temperature dependence of thermoelectric parameters, including the Thomson effect. Moreover, formula (1) does not characterize the quality of a thermoelement with a superconductor. Indeed, for $\alpha = \rho = 0$, this formula gives the Z value of only one branch, although it is obvious that the thermal conductivity of the superconductor will also contribute to the thermoelectric quality of the whole thermoelement.

In order to provide for a more adequate description of thermal processes in branches of a thermoelement, it is necessary to use a consistent approach based on the solution of a boundary-value problem [4]. In solving this problem, we will ignore thermal losses and the Joule effect in the junction and contacts. The temperature field of a one-dimensional adiabatically insulated branch of a thermoelement operating in a steady-state regime with allowance of the Thomson effect is described by the stationary thermal conductivity equation

$$\frac{d}{dx}\left(\chi_i(T)S_i\frac{dT}{dx}\right) + \frac{J^2\rho_i(T)}{S_i} - JT\frac{d\alpha_i(T)}{dT}\frac{dT}{dx} = 0 \qquad (2)$$

with the boundary conditions

$$\chi_i(T_0)S_i\frac{dT}{dx}\bigg|_{x=0} = \alpha_i(T_0)JT_0 - Q_{0i}, \quad T\big|_{x=l_i} = T_{\text{hot}}, \qquad (3)$$

where $\alpha_i(T)$, $\rho_i(T)$, and $\chi_i(T)$ ($i = n, p$) are the thermo emf, resistivity, and thermal conductivity of the *i* branch, respectively, as functions of the temperature; J is the electric current; S_i and l_i are the cross section

1063-7850/04/3007-0532$26.00 © 2004 MAIK “Nauka/Interperiodica”

and length of the *i* branch, respectively; T_0 and T_{hot} are the temperature of the cold and hot ends of the branch, respectively; and Q_{0i} is the cold production of the *i* branch. The experimental temperature dependences of the thermo emf, resistivity, and thermal conductivity for a $Bi_{85}Sb_{15}$ alloy in the direction of a trigonal axis were approximated by power polynomials. The geometry of branches is selected the same as in [2].

The branch is usually called passive in cases of small thermoelectric efficiency. However, the cold production in a given branch can be negative even for a rather high thermoelectric efficiency, provided that the efficiency of the second branch is still higher. In this case, we may speak of a passive operation of the branch. This situation is most frequently realized in thermoelements operating in the regime of maximum temperature drop. Because of the nonequivalence of the two branches, one branch of a thermoelement operating in such a regime works predominantly in the active regime, while the other branch works mostly in the passive regime. The temperature distributions in the branches operating in these regimes are substantially different. According to the results of calculations performed within the framework of this study, the temperature profile of a branch operating in the active regime exhibits a maximum in the vicinity of the hot end, while no such maximum is observed on the passive branch. In a thermoelement operating in the regime of maximum cold production, both branches become active at a sufficiently high load.

The passive *p* branch in [2] was a superconductor of the $BiSrCaCu_2O_x$ type. In this branch, the Joule effect is absent and the Thomson heat can be ignored. As a result, the boundary-value problem is formulated as

$$\frac{d}{dx}\left(\chi_s(T)S_s\frac{dT}{dx}\right) = 0, \tag{4}$$

$$\chi_s(T_0)S_s\frac{dT}{dx}\bigg|_{x=0} = -Q_{0s}, \quad T\big|_{x=l_s} = T_{\text{hot}}, \tag{5}$$

where χ_s is the specific thermal conductivity of the superconductor; S_s and l_s are the cross section and length of the superconductor, respectively; and Q_{0s} is the heat supplied to the cold junction of the superconductor ($Q_{0s} < 0$). The passive branch geometry adopted in [2] was retained in this model calculation. The temperature dependence of the thermal conductivity of a superconductor of the aforementioned type [5] was also approximated by a power polynomial. The cold production of the thermoelement under consideration was defined as a sum for the two branches:

$$Q_0 = Q_{0n} + Q_{0p}. \tag{6}$$

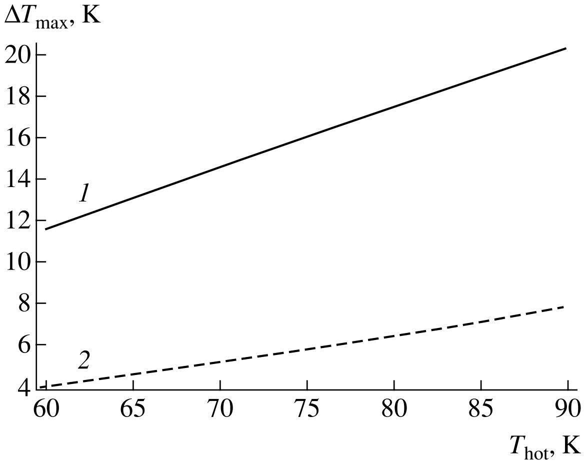

Fig. 1. Plots of the maximum temperature drop ΔT_{max} versus hot junction temperature T_{hot} for a thermoelement with the passive branch made of (*1*) superconductor and (*2*) bismuth telluride.

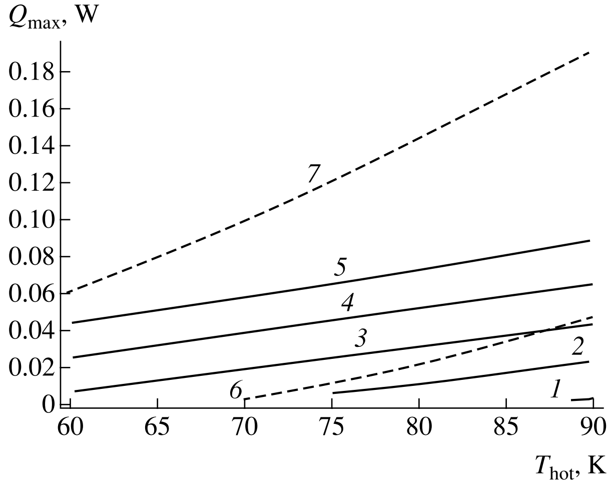

Fig. 2. Load characteristics representing maximum power Q_{max} versus hot junction temperature T_{hot} for a thermoelement with the passive branch made of a superconductor (solid curves *1–5*) and bismuth telluride (dashed curves *6* and *7*) operating at various temperature drops ΔT(K): (*1*) 20; (*2*) 15, (*3*) 10, (*4*, *6*) 5; (*5*, *7*) 0.

The load characteristics of the thermoelement were calculated for the regimes of maximum temperature drop and maximum cold production, with optimization with respect to the current. For comparison, a model calculation was also performed for a thermoelement with bismuth telluride in the *p* branch. Figure 1 shows the calculated plots of the maximum temperature drop in a thermoelement with the superconductor (curve *1*) and bismuth telluride (curve *2*) branches. The corresponding load characteristics are presented in Fig. 2. As can be seen from the latter figure, the cold production of the thermoelement with a bismuth telluride branch operating at a temperature drop of $\Delta T = 5$ K in the entire temperature interval is lower than that of the thermoelement with a superconductor passive branch at $\Delta T = 10$ K. However, the cold production of the thermoelement with the bismuth telluride branch sharply increases at a zero temperature drop.

Obviously, the cold production in a superconductor branch is negative in all regimes. For the bismuth telluride branch, the value of cold production becomes positive for large loads and small temperature drops (below 5 K). As can be seen, a superconductor in the *p* branch is preferred for thermoelectric coolers aimed at obtaining considerable temperature drops, and bismuth telluride, for heat pumps operating at small temperature drops. This circumstance has to be borne in mind in designing coolers for various applications.

As the temperature at the hot end of the branch decreases, the optimum current drops. Therefore, the cross section of the superconducting branch can be reduced, which provides for an additional, albeit small, decrease in the temperature.

REFERENCES

1. G. E. Smith and R. Wolf, J. Appl. Phys. **33**, 841 (1962).
2. V. L. Kuznetsov, M. V. Vedernikov, P. Yandl’, and U. Birkhgol’ts, Pis’ma Zh. Tekh. Fiz. **20** (18), 75 (1994) [Tech. Phys. Lett. **20**, 757 (1994)].
3. A. F. Ioffe, *Semiconductor Thermoelements* (Akad. Nauk SSSR, Moscow, 1960).
4. O. I. Markov, Inzh.-Fiz. Zh. **76**, 185 (2003).
5. Yu. A. Kirichenko, K. V. Rusanov, and E. G. Tyurina, Sverkhprovodimost: Fiz. Khim. Tekh. **3**, 1385 (1990).

Translated by P. Pozdeev

Technical Physics Letters, Vol. 30, No. 7, 2004, pp. 535–537. Translated from Pis'ma v Zhurnal Tekhnicheskoĭ Fiziki, Vol. 30, No. 13, 2004, pp. 12–18.
Original Russian Text Copyright © 2004 by Boikov, Danilov.

Electric Resistance of $La_{0.67}Ca_{0.33}MnO_3$ Films Biaxially Strained during Growth on Lattice-Mismatched Substrates

Yu. A. Boikov* and V. A. Danilov
Ioffe Physicotechnical Institute, Russian Academy of Sciences, St. Petersburg, 194021 Russia
**e-mail: Yu.Boikov@mail.ioffe.ru*

Received January 23, 2004

Abstract—We have studied the electric resistance of 20-nm-thick $La_{0.67}Ca_{0.33}MnO_3$ films coherently grown on single crystal substrates with considerable (negative) and almost zero lattice mismatch. The unit cell volume in the growing film depends on the substrate lattice parameter. At $T < 200$ K and $\mu_0 H = 0$, the resistance of manganite films on (001)$LaAlO_3$ substrates was several orders of magnitude greater than the value for an analogous film grown on (001)$La_{0.29}Sr_{0.71}Al_{0.65}Ta_{0.35}O_3$. The observed decrease in resistance of the elastically strained (biaxial compression) manganite films is related to a superstoichiometric (≈45%) relative concentration of Mn^{4+} ions in the film volume. *© 2004 MAIK "Nauka/Interperiodica".*

Thin films of $La_{0.67}(Sr,Ca)_{0.33}MnO_3$ are promising materials for readout heads in magnetic memory devices [1], IR radiation sensors [2], etc. The electron transport in both bulk samples and thin films of such perovskite-like manganites depends on the degree of delocalization of e_g electrons which, in turn, is determined by the character of orbital, charge, and spin ordering [1]. Biaxial mechanical stresses and external magnetic fields significantly affect the structural and magnetic ordering in $La_{0.67}(Sr,Ca)_{0.33}MnO_3$ films and influence the density of nonferromagnetic phase inclusions in their volume at temperatures $T < T_{\text{Curie}}$ (where T_{Curie} is the temperature of the ferromagnetic phase transition) [3, 4]. Mechanical stresses are considered as a possible mechanism of controlled action upon thin manganite films, aimed at optimization of the electron characteristics of the material [5].

This Letter presents the results of experimental investigation of the temperature dependence of the resistivity ρ of thin $La_{0.67}Ca_{0.33}MnO_3$ (LCMO) manganite films coherently grown on substrates of two types: (a) $LaAlO_3$ (LAO) with a considerable (~1.8%) negative mismatch between crystal lattice parameters of the film and substrate and (b) $La_{0.29}Sr_{0.71}Al_{0.65}Ta_{0.35}O_3$ (LSATO) with a small (~0.3%) positive lattice mismatch.

LCMO manganite films with a thickness of d = 20 nm were grown by laser ablation (KrF, λ = 248 nm, τ = 30 ns) on polished LAO and LSATO substrates heated to 760°C in an oxygen atmosphere (P_0 = 0.3 mbar). The growth conditions and the structural features of thin manganite films grown on (001)LAO and (001)LSATO substrates were considered in detail elsewhere [6, 7].

The phase composition, orientation, and crystal lattice parameters of the grown films were determined by X-ray diffraction (Philips X'pert MRD; ω/2θ and ϕ scans; rocking curves) as described in [7]. The film thickness d was determined from data on the width of the satellite Laue peaks (Fig. 1). The resistance R of the LCMO manganite films was measured in the Van der Pauw geometry in a magnetic field of $\mu_0 H$ = 0–5 T and then the resistivity ρ was calculated as $\rho = \pi R d/\ln 2$ [8].

The results of the X-ray diffraction measurements (ω/2θ and ϕ scans) showed that 20-nm-thick LCMO

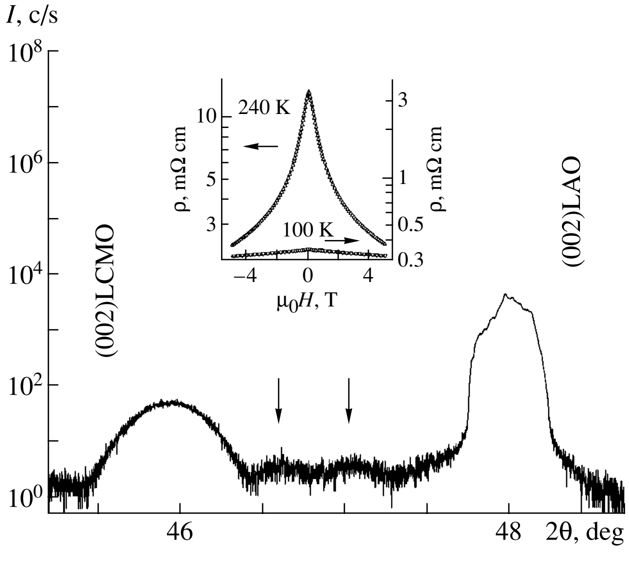

Fig. 1. The X-ray diffractogram (Cu$K_{\alpha 1}$, ω/2θ scan) of a 20-nm-thick LCMO film grown on a (001)LAO substrate. Arrows indicate the satellite Laue peaks. The inset shows plots of the resistivity ρ versus magnetic field H for a 20-nm-thick LCMO/LSATO film measured at 240 and 100 K (the magnetic field was parallel to the substrate plane and the current direction).

1063-7850/04/3007-0535$26.00 © 2004 MAIK "Nauka/Interperiodica"

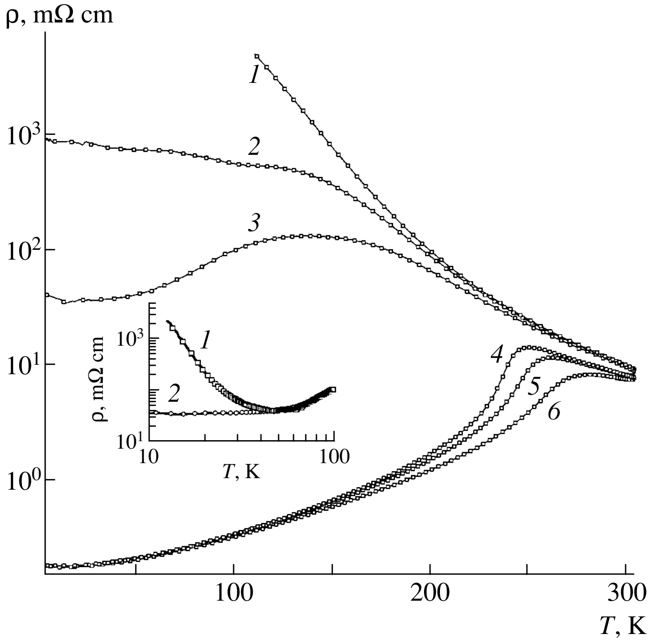

Fig. 2. Temperature dependences of the resistivity ρ for 20-nm-thick LCMO films grown on (*1*–*3*) (001)LAO and (*4*–*6*) (001)LSATO substrates, measured in the cooling mode in various magnetic fields: μ_0H = 0 (*1*, *4*), 2 (*2*), 4 (*3*), 1 (*5*), 3 T (*6*). The magnetic field was parallel to the substrate plane and the current direction. The inset shows the ρ(*T*) curves for the 20-nm-thick LCMO/LAO film measured in the magnetic field μ_0H = 4 T in the (*1*) heating and (*2*) cooling mode (curve *1* was measured for the sample cooled in a zero magnetic field).

films were formed by the cube-on-cube epitaxy on the substrates of both types. The full width at half maximum (FWHM) of the rocking curve for the (002) reflection of an LCMO/LAO film was 0.25°, which is about twice the value for the corresponding reflection of an LCMO/LSATO film. The unit cell parameter of a 20-nm-thick LCMO/LAO film measured along the normal to the substrate surface, $a_\perp = 3.945 \pm 0.003$ Å, was significantly greater than the value measured in the film plane, $a_\parallel = 3.786 \pm 0.003$ Å. The large difference between $a_\perp$ and $a_\parallel$ indicates that the 20-nm-thick LCMO/LAO film was subjected to considerable compressive biaxial stresses acting in the substrate plane in the course of nucleation and growth. This factor accounts [7] for the considerable decrease in the unit cell volume of this film, $V_{\text{eff}} = (a_\parallel^2 x a_\perp) = 56.55$ Å^3, as compared to the value for the bulk stoichiometric LCMO crystals ($V_{\text{eff}} = 57.40$ Å^3) [9]. For a 20-nm-thick LCMO/LSATO film, the values of lattice parameters were $a_\perp = 3.838 \pm 0.003$ Å and $a_\parallel = 3.868 \pm 0.003$ Å, while the unit cell volume V_{eff} was virtually the same as that in the bulk LCMO crystals. The parameters of a pseudocubic unit cell of both substrates, $a_{\text{LAO}} = 3.785 \pm 0.003$ Å and $a_{\text{LSATO}} = 3.869 \pm 0.003$ Å, coincided with the values of $a_\parallel$ of the LCMO films grown on these substrates.

The decrease in the unit cell volume of the LCMO film as compared to the value of V_{eff} in the bulk crystal can be related to enrichment of the film with calcium and/or oxygen (in the latter case, vacancies appear in the cation sublattice). Such a decrease in the unit cell volume for both films and bulk samples of LCMO is accompanied by an increase in the concentration of tetravalent manganese ions (Mn^{4+}) [10]. The decrease of V_{eff} in our 20-nm-thick LCMO/LAO films corresponds to an increase in the density of Mn^{4+} ions up to ~45%.

Figure 2 shows the temperature dependences of the resistivities of 20-nm-thick LCMO films grown on (001)LAO and (001)LSATO. The curve of $\rho(T, H = 0)$ for the 20-nm-thick LCMO/LSATO film agrees well with the temperature dependence of ρ observed previously for the bulk stoichiometric samples and thick epitaxial films of LCMO [6]. In particular, the $\rho(T, H = 0)$ curve for the 20-nm-thick LCMO/LSATO film exhibits a maximum at $T_M \approx 250$ K. The application of a magnetic field favors magnetic ordering of the spins of manganese ions, which is accompanied by an increase in the effective mobility of holes in the film, a decrease in the resistivity ρ, and a shift of the resistivity maximum toward higher temperatures (Fig. 2). The most pronounced decrease in the resistivity of the LCMO/LSATO film in a magnetic field was observed at temperatures close to T_M (see the inset in Fig. 1). The negative magnetoresistance $MR = [\rho(\mu_0H = 5\text{ T}) - \rho(H = 0)]/\rho(H = 0)$ amounted to 83% at $T = 240$ K and decreased to 9 and 3% at $T = 100$ and 4.2 K, respectively.

In the temperature interval from 300 K to T_M (corresponding to the paramagnetic phase), both the absolute values of resistivities and the shapes of the temperature dependences of ρ for the 20-nm-thick LCMO/LAO and LCMO/LSATO films are very close (Fig. 2). For $T < T_M$, however, the behavior of $\rho(T)$ in these films is sharply different: in contrast to the temperature dependence of ρ in the LCMO/LSATO film, the $\rho(T, H = 0)$ curve of the LCMO/LAO film has no maximum (T = 100–300 K) and exhibits a significant increase in the slope $d\rho/dT$ in the vicinity of $T = 230$ K.

At $H = 0$, the temperature dependence of resistivity ρ for the 20-nm-thick LCMO films on both LAO and LSATO substrates was well reproduced after multiply repeated thermal cycles in the 4.2–300 K range. The curves of $\rho(T, \mu_0H = 5\text{ T})$ for the 20-nm-thick LCMO/LAO film measured in the course of cooling from 300 to 4.2 K and subsequent heating in the same temperature range also virtually coincided.

The increase in the resistance of the 20-nm-thick LCMO/LAO films with decreasing temperature at $T < T_M$ is explained by the formation ($T \approx 230$ K) of inclusions (interlayers) of a ferromagnetic phase with low conductivity in the volume of these films. At

$T \approx 150$ K, this phase transforms into an antiferromagnetic phase [11]. The presence of antiferromagnetic inclusions in the bulk samples of $La_{1-x}Ca_xMnO_3$ with a concentration of Mn^{4+} ions above 44% was established using neutron diffraction data [10]. Degradation of the conductivity of 20-nm-thick LCMO/LAO films in comparison to that of the manganite layers on LSATO is explained by the relatively high concentration of antiferromagnetic inclusions (interlayers) in the volume of the former films. In the 20-nm-thick LCMO/LSATO films, the inclusions of nonferromagnetic phases are also present, but in a lower concentration, and their influence on the electron transport is insignificant.

Magnetic field decreases the disorientation of spins in magnetic domains of the 20-nm-thick LCMO/LAO film and reduces the probability of nucleation of the aforementioned antiferromagnetic inclusions in the volume of this film. In the magnetic field, the energy barrier determining the rate of formation of stable nuclei of the antiferromagnetic phase in the manganite film increases by an amount equal to the Zeeman energy [12] proportional to the product MH, where M is the spontaneous magnetization. This favors a decrease in the fraction of antiferromagnetic phase in the volume of the film, which is accompanied by a significant decrease in resistivity ρ. At $T = 10$–50 K, the resistivity of a 20-nm-thick LCMO/LAO film cooled in a magnetic field of $\mu_0 H = 4$ T was significantly lower than ρ of the same film cooled at $H = 0$ and then exposed to the magnetic field $\mu_0 H = 4$ T (see the inset in Fig. 2). At $T > 50$ K, the curves of $\rho(T, \mu_0 H = 4\text{ T})$ of the 20-nm-thick LCMO/LAO film measured on cooling and heating (upon cooling at $H = 0$) coincided. The rate of sample heating and cooling in the course of $\rho(T)$ measurements was 10 K/min.

The process of the magnetic-field-induced "melting" of the antiferromagnetic inclusions in the 20-nm-thick LCMO/LAO film cooled at $\mu_0 H = 0$ was activated by the temperature. At $T = 4.2$ K, an increase in $\mu_0 H$ from 0 to 5 T was accompanied by a sharp (40–80%) drop in the electric resistance of this film, which was caused by the spatial ordering of spins in ferromagnetic domains. This was followed by a slow (≈2% for 5 min) decrease in ρ as a result of "melting" of the antiferromagnetic inclusions.

At $T < 180$ K, the negative magnetoresistance of the 20-nm-thick LCMO/LAO films was significantly greater than that of manganite films of the same thickness grown on (001)LSATO.

Acknowledgments. This study was supported by the Presidium of the Russian Academy of Sciences within the framework of the Program "Low-Dimensional Quantum Nanostructures" (project no. 9B19).

REFERENCES

1. Y. Tokura, *Colossal Magnetoresistive Oxides*, Ed. by Y. Tokura (Gordon and Breach, Amsterdam, 2000), p. 2.
2. A. Goyal, M. Rajeswari, R. Shreekala, *et al.*, Appl. Phys. Lett. **71**, 2535 (1997).
3. L. Alff, J. Philipp, D. Reisinger, *et al.*, Physica B **329–333**, 965 (2003).
4. N. D. Mathur and P. B. Littlewood, Phys. Today **56**, 25 (2003).
5. N. D. Mathur and P. B. Littlewood, Solid State Commun. **119**, 271 (2001).
6. Yu. A. Boikov, T. Klaeson, and A. Yu. Boĭkov, Zh. Tekh. Fiz. **71** (10), 54 (2001) [Tech. Phys. **46**, 1260 (2001)].
7. Yu. A. Boikov, T. Klaeson, and A. Yu. Boĭkov, Fiz. Tverd. Tela (St. Petersburg) **45**, 1040 (2003) [Phys. Solid State **45**, 1090 (2003)].
8. T. I. Kamins, J. Appl. Phys. **42**, 4357 (1971).
9. J. Aarts, S. Freisem, R. Hendrikx, and H. W. Zandbergen, Appl. Phys. Lett. **72**, 2975 (1998).
10. E. O. Wollan and W. C. Koehler, Phys. Rev. **100**, 545 (1955).
11. P. G. Radaelli, D. E. Cox, M. Marezio, *et al.*, Phys. Rev. Lett. **75**, 4488 (1995).
12. Y. Tomioka and Y. Tokura, in *Colossal Magnetoresistive Oxides*, Ed. by Y. Tokura (Gordon and Breach, Amsterdam, 2000), p. 286.

Translated by P. Pozdeev

Technical Physics Letters, Vol. 30, No. 7, 2004, pp. 538–540. Translated from Pis'ma v Zhurnal Tekhnicheskoĭ Fiziki, Vol. 30, No. 13, 2004, pp. 19–24.
Original Russian Text Copyright © 2004 by Kaveeva, Rozhansky.

Poloidal and Toroidal Flows in Tokamak Plasma near Magnetic Islands

E. G. Kaveeva* and V. A. Rozhansky
St. Petersburg State Technical University, St. Petersburg, 195251 Russia
**e-mail: lisa@phtf.stu.neva.ru*

Received January 29, 2004

Abstract—The radial electric field and toroidal rotation of tokamak plasma near a magnetic island have been calculated. Outside the magnetic island, the radial electric field varies from a value determined by the rotation of this island to the neoclassical value over a scale dependent on the anomalous viscosity and collisionality of the plasma. Inside the magnetic island, the radial electric field is constant. © *2004 MAIK “Nauka/Interperiodica”.*

Introduction. In recent years, it was experimentally demonstrated that the appearance of internal transport barriers in tokamak plasma is related to the q profile, in particular, to the rational flux surfaces with integer q values [1]. Since magnetic islands are formed in the vicinity of such surfaces, we may suggest that the barrier formation is related to variations in the radial electric field near the island and to the turbulence suppression by the $E \times B$ drift. Guenter *et al.* [2] attributed an increase in the radial electric field to the appearance of a radial current caused by the fishbone activity. However, a change in the electric field may arise even in the absence of additional currents, merely due to the presence of a magnetic island. Shaing [3] calculated the electric field near the island with neglect of a toroidal rotation and anomalous momentum transport in the plasma. However, both these factors are highly important.

In this context, we have calculated the electric field and the toroidal rotation near the magnetic island in the fluid regime. It is established that the radial electric field outside the island varies from a value determined by the rotation of this island to the neoclassical value over a scale δ dependent on the anomalous viscosity and collisionality of the plasma.

Description of model. Let us consider a rational flux surface in the tokamak with a circular cross section, large aspect ratio ($\varepsilon = r/R \ll 1$), $q = m/n$, and $b_\theta = B_\theta/B = \text{const}$ (θ and ϕ denote poloidal and toroidal angles, respectively). The radial perturbation of the magnetic field caused by the magnetic island is $\delta B = \delta B^{(0)}\exp(-i\omega t + im(\theta - \varepsilon\sin\theta) - in\phi)$; x, y, and z are the coordinates in the island, whereby the y axis is perpendicular to the flux surface in the island, the z axis is directed along the unperturbed magnetic field on the rational surface, and the x axis is perpendicular to the yz plane (Fig. 1). Below, the symbol $\perp$ will refer to the direction perpendicular to the magnetic field $\mathbf{B}$ and the y axis. We assume that the island width Δ is greater than the poloidal gyroradius ρ_s/b_θ and the scale δ/ε (the latter is determined below).

First, let us consider a stationary magnetic island ($\omega = 0$). The plasma is described in terms of the Braginskii equations with the perpendicular transport coefficients replaced by their anomalous values. The parallel velocity averaged over the flux surface, as well as the poloidal drift, can be determined from the equations

$$\langle \mathbf{B} \cdot \nabla(\overleftrightarrow{\pi}^{(0)} + \overleftrightarrow{\pi}^{(\mathrm{AN})})\rangle = 0, \tag{1}$$

$$\langle\langle j_y \rangle\rangle = 0. \tag{2}$$

where $\langle f \rangle = \oint f\sqrt{g}\,dxdz/\oint\sqrt{g}\,dxdz$ and $\langle\langle f \rangle\rangle = \oint f\, h_x h_z dxdz/\oint h_x\, h_z dxdz$; h_x, h_y, and h_z are the metric coefficients; and $\sqrt{g} = h_x h_y h_z$. Equation (1) for the toroidally symmetric case in the absence of anomalous viscosity is well known in the neoclassical theory [4],

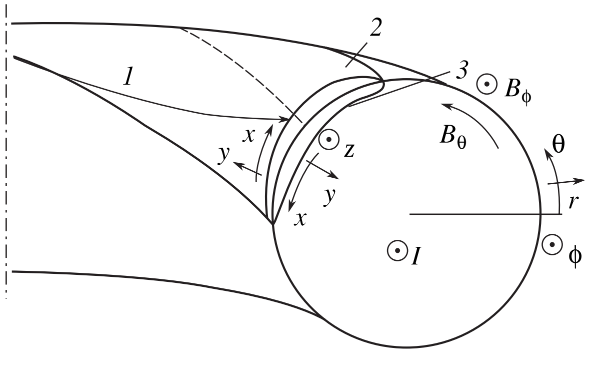

Fig. 1. Magnetic island geometry and coordinate system: (*1*) field line; (*2*) outer side; (*3*) inner side.

1063-7850/04/3007-0538$26.00 © 2004 MAIK “Nauka/Interperiodica”

while Eq. (2) reflects quasi-neutrality of the plasma. In these equations, $\overset{\leftrightarrow}{\pi}^{(0)}$ is the classical parallel viscosity tensor determined according to Braginskii. The anomalous viscosity is taken in the simplest form:

$$-(\nabla\cdot\pi^{(\mathrm{AN})})_{\parallel} = \frac{1}{\sqrt{g}}\frac{\partial}{\partial y}\left(\frac{\sqrt{g}}{h_y^2}\eta^{(\mathrm{AN})}\frac{\partial V_{\parallel}}{\partial y}\right).$$

Inside the island, Eq. (1) can be transformed to

$$\frac{d^2(b_\theta\langle V_{\parallel}\rangle)}{\langle h_y^2\rangle dy^2} - \varepsilon^2\delta^{-2}\left(b_\theta\langle V_{\parallel}\rangle + \alpha\frac{B_x}{B_\theta}\langle V_{\perp}\rangle\right) = 0, \quad \alpha \sim 1, \quad (3)$$

$$\delta = \sqrt{\frac{2}{3}\frac{\eta^{(\mathrm{AN})}r^2}{\eta_0 b_\theta^2}}, \quad \eta_0 = 0.96nT_i/\nu_i. \quad (4)$$

In contrast to the situation in the tokamak without islands, where the contribution due to poloidal $E \times B$ and diamagnetic drift in Eq. (1) is significant, the value of $\langle V_{\perp}\rangle$ inside the island is multiplied by a small coefficient $B_x/B_\theta \sim \Delta/r \ll 1$. This is related to the fact that poloidal drifts have opposite directions on different (inner and outer, Fig. 1) sides of the island. At the same time, the contribution of $\langle V_{\parallel}\rangle$ to Eq. (1) upon averaging is the same on both sides.

Determining the radial current in Eq. (2) using the x-component of the momentum balance and the pressure profile found from the parallel momentum balance, we obtain

$$\frac{d^2\langle V_{\perp}\rangle}{\langle h_y^2\rangle dy^2} - \frac{1}{2\delta^2}\left(\langle V_{\perp}\rangle + \beta\frac{B_x}{B_\theta}b_\theta\langle V_{\parallel}\rangle\right) = 0, \quad \beta \sim 1. \quad (5)$$

For the current through a flux surface inside the island to be zero, the poloidal drift velocity must be significantly smaller than the poloidal projection of the parallel velocity. The Pfirsch–Schlüter flows, the Braginskii parallel viscosity, and related poloidal perturbations in the pressure (caused by the variations of $\langle V_{\parallel}\rangle$) are almost identical inside and outside the island. Therefore, the difference between currents related to ∇p and $\nabla\cdot\overset{\leftrightarrow}{\pi}$ (caused by $\langle V_{\parallel}\rangle$)—flowing in and out of the island, respectively—is proportional to Δ/r. At the same time, the term of the radial current related to the drift velocity $V_{\perp}$ has opposite signs inside and outside the island and does not contain the small coefficient Δ/r.

Ignoring small terms of the order of Δ/r, we may consider relations (3) and (5) as two independent equations for the drifts and parallel velocity, determining their typical decay length toward the center of the island. A boundary condition must set the velocity at the island separatrix. Proceeding from symmetry considerations, the poloidal velocity near the separatrix outside the island has to be almost constant, since the form of equations for the poloidal velocity and the neoclassical poloidal rotation values are the same on the inner and outer sides of the island (Fig. 2). The poloidal rotation in the island has opposite directions on the two sides of the separatrix, since the electrostatic potential on a flux surface inside the island is constant. The only symmetric solution for $\langle V_{\perp}\rangle$ appears at $\langle V_{\perp}\rangle = 0$ on the separatrix. According to Eq. (5), $\langle V_{\perp}\rangle = 0$ everywhere inside the island. We may also consider various asymmetric solutions, for which the rotation on the opposite sides of the island is different. However, such solutions are inconsistent with Eq. (2) because asymmetric transition zone at the separatrix causes asymmetric pressure perturbations, gives rise to asymmetric anomalous viscous forces, and eventually leads to nonzero net current through the separatrix.

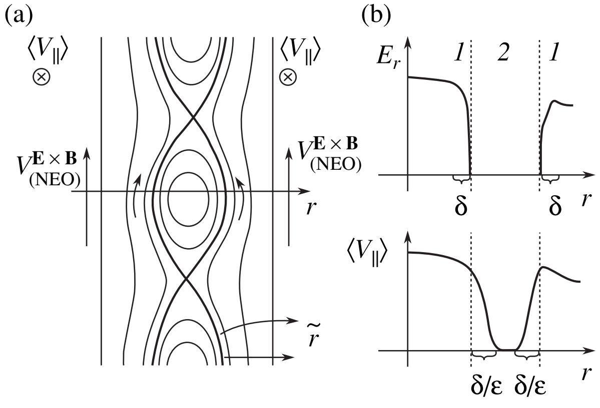

Fig. 2. Schematic diagrams of (a) flux surfaces and flow directions near the magnetic island and (b) radial profiles of the radial electric field and average parallel velocity for a stationary island (r axis passes through the center of the island): (*1*) separatrix; (*2*) magnetic island.

Outside the island, we use the coordinates $\tilde{r}$, θ, and ϕ. The $\tilde{r}$ axis is perpendicular to the perturbed flux surface (Fig. 2) and the $\tilde{r}$ value is equal to the mean minor radius of the surface. Using the toroidal momentum balance and the condition of zero current through the surface expressed by Eq. (2), we obtain

$$-\left\langle\!\!\left\langle\frac{1}{B_\theta\sqrt{g}}\frac{\partial}{\partial\tilde{r}}\left(\frac{\sqrt{g}}{h_r^2}\eta^{(\mathrm{AN})}\frac{\partial V_{\parallel}}{\partial\tilde{r}}\right)\right\rangle\!\!\right\rangle + \left\langle\!\!\left\langle\frac{(\nabla p + \nabla\cdot\pi^{(0)})_\phi}{B_\theta}\right\rangle\!\!\right\rangle = 0. \quad (6)$$

In the case of a toroidally symmetric flux surface, the second term in this equation vanishes [4]. In the presence of a magnetic island, the toroidal symmetry is broken and the second term appears with the factor Δ/r. Using Eq. (6), we determine the small perturbation in the parallel velocity caused by the appearance of the island: $(\langle V_{\parallel}\rangle - \langle V_{\parallel}\rangle_{\text{without island}})/\langle V_{\parallel}\rangle \sim b_\theta^{-1}\varepsilon^2\Delta/r \ll 1$. Subtracting Eq. (1) from Eq. (6), we obtain an equation for the poloidal velocity outside the island:

$$\frac{\partial^2}{\partial \tilde{r}^2}\langle V_\theta\rangle = \frac{\langle V_\theta\rangle}{2\delta^2}. \qquad (7)$$

Poloidal rotation varies over the scale δ from the value on the island separatrix to the neoclassical value:

$$E_{\tilde{r}} = E_{\tilde{r}}^{(\mathrm{NEO})}\{1 - \exp[(\tilde{r} - \tilde{r}_{\mathrm{sep}})/\sqrt{2}\delta]\},$$
$$E_{\tilde{r}}^{(\mathrm{NEO})} = \frac{T_i}{e}\left(\frac{d\ln n}{h_{\tilde{r}}d\tilde{r}} + k_T\frac{d\ln T_i}{h_{\tilde{r}}d\tilde{r}}\right) + \langle V_\parallel B_\theta\rangle\frac{\langle\langle h_{\tilde{r}}\rangle\rangle}{h_{\tilde{r}}}. \qquad (8)$$

When the island rotates ($\omega \neq 0$), the resulting vortex electric field acquires a component along the magnetic field. By virtue of a large parallel conductivity of the plasma, there must arise a potential field such that the total electric field in the parallel direction would become zero, $E_r = -\langle B\rangle\omega r/m$. This radial field induces poloidal rotation of the plasma at a velocity equal to that of the island rotation $V_\theta^{\mathrm{island}} = (1 + \varepsilon\cos\theta)\omega r/m$. In this case, Eq. (3) should be replaced by

$$\frac{d^2(b_\theta\langle V_\parallel\rangle)}{\langle h_y^2\rangle dy^2} - \varepsilon^2\delta^{-2}(b_\theta\langle V_\parallel\rangle + \langle V_\theta^{\mathrm{island}}\rangle) = 0. \qquad (9)$$

The radial electric field near the rotating island decreases over the scale δ from the neoclassical value to $E_r = -\langle B\rangle\omega r/m$ on the separatrix.

Conclusions. We have demonstrated that the electric field inside a stationary magnetic island is zero, while the toroidal rotation decreases from a value on the separatrix to zero over the scale δ/ε, where δ depends on the anomalous transverse viscosity and collisionality of the plasma. Outside the island separatrix, the radial electric field varies from zero to the neoclassical value over the scale δ, while the toroidal velocity remains almost constant. Rotation of the island gives rise to an additional radial electric field. The field profile near the island is much like that near the divertor tokamak separatrix [5].

Acknowledgments. This study was supported by the Russian Foundation for Basic Research, project no. 03-02-16196.

REFERENCES

1. R. C. Wolf, Plasma Phys. Controlled Fusion **45**, R1 (2003).
2. S. Guenter *et al.*, in *Proceedings of the 28th EPS Conference on Plasma Physics and Controlled Fusion, Funchal, 2001*, Vol. 25A, p. 1006.
3. K. C. Shaing, Phys. Plasmas **9**, 3470 (2002).
4. S. P. Hirshman and D. J. Sigmar, Nucl. Fusion **21**, 1079 (1981).
5. V. Rozhansky *et al.*, Nucl. Fusion **42**, 1110 (2002).

Translated by P. Pozdeev

Technical Physics Letters, Vol. 30, No. 7, 2004, pp. 541–544. Translated from Pis'ma v Zhurnal Tekhnicheskoĭ Fiziki, Vol. 30, No. 13, 2004, pp. 25–33.
Original Russian Text Copyright © 2004 by Kadmenskiĭ, Tulinov.

Anomalies in Multiple Scattering of Charged Particles in a Thick Crystal

A. G. Kadmenskiĭ[a],* and A. F. Tulinov[b]
[a]*Central Institute of Machine Building, Korolev, Moscow oblast, Russia*
[b]*Research Institute of Nuclear Physics, Moscow State University, Moscow, 119899 Russia*
**e-mail: Akadm@rambler.ru*

Received September 3, 2003; in final form, December 23, 2003

Abstract—The dynamics of charged particle channeling in a crystal consisting of atomic chains is considered. The multiple scattering of charged particles, introduced by the trajectory integral method, leads to transitions between dynamical modes of the axial channeling, whereby double channeling is a sink for the normal channeling. Volume rechanneling takes place under the conditions of random motion. In this case, up to ~20% of incident charged particles move in the channeling regime over a depth equal to the normal range, and a considerable fraction of these particles are involved in the double channeling regime. *© 2004 MAIK “Nauka/Interperiodica”.*

Introduction. Investigation of the dynamics of fast positively charged particles and ions (referred to below as particles) [1, 2] in a model crystal composed of Lindhard atomic chains [3] showed the existence of a regular motion in the continuous transverse potential for the initial conditions corresponding to the incidence angles simultaneously small relative to the crystallographic axis z (polar angle θ_0) and the atomic plane containing this axis (azimuthal angle φ_0). Since the autocorrelation function for the transverse momenta of particles does not decay with the traveled distance, we may speak of a new stable regime analogous to channeling between the rows of atomic chains (i.e., between atomic planes as the “chains of atomic chains” in Lindhard's terminology). This regime was called double channeling (DCh).

Under different initial conditions—corresponding to the same small θ_0 but somewhat increased φ_0 (characteristic values, 0.3–0.4)—the autocorrelation function rapidly decays with the depth z. The decay (in contrast to the behavior observed for a model medium representing the “gas” of atomic chains [3, 4]) is nonmonotonic. This is accompanied by a rapid azimuthal expansion of the flow and filling [inhomogeneous (!)] of the azimuthal ring distribution (characteristic of the channeling) with an average value of the transverse momentum rapidly approaching zero. Since these properties were postulated in the Lindhard hypothesis [3] for the entire flow of channeled particles, this regime was referred to as normal channeling (NCh).

Both DCh and NCh regimes differ substantially from the description of channeling within the framework of the statistical equilibrium model [3] and demonstrate anomalous values of the rate of multiple scattering, with a twofold increase (relative to equilibrium statistical values) for NCh and approximately the same decrease for DCh [2]. The two regimes are also at variance with the statistical theory of channeling based on the chain of Bogoliubov–Born–Green–Kirkwood–Yvon equations.

For $\varphi = 0$, the DCh regime corresponds to the well-known experimental behavior on the transition from axial to planar channeling (see, e.g., [6]). Sharp drops in the number of particles penetrating through a thin crystal observed in this regime for certain initial polar angles θ_0 correspond to the so-called resonance dechanneling. For the other azimuthal angles, $\varphi^{cr} > \varphi_0 > 0$ [2], the DCh regime also exhibits peculiarities (resonance) in the dependence on θ_0, which are even more pronounced than the features for $\varphi_0 = 0$. Because of the two-dimensional character of motion and the region of existence in the transverse space, as well as the presence of resonance peculiarities, the DCh regime differs from the well-known planar channeling.

In this Letter, we will consider the influence of the multiple scattering effects on the behavior of a beam of channeled particles in a crystal.

Theoretical analysis. In order to include the effects of multiple scattering of particles on the nuclei with allowance of lattice vibrations at a given temperature T, we used the results of calculations of the average square polar angle of particle scattering relative to the channel axis along the trajectory with preset invariants of motion in the field of an atomic chain. These invariants include the dimensionless transverse energy $\varepsilon_\perp$ and the transverse momentum (determined by the impact parameter $b_\perp$ of the particle collision with the atomic

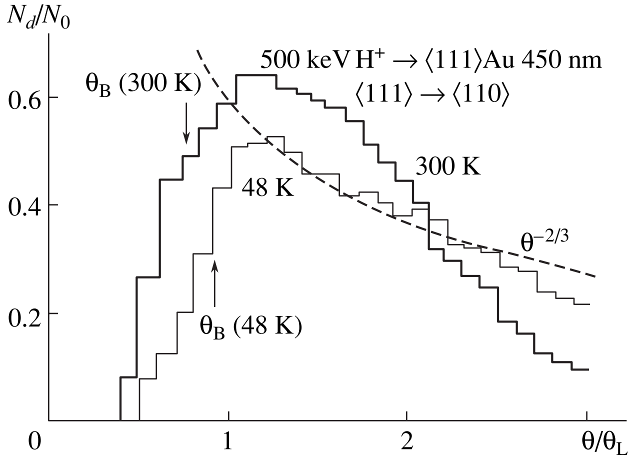

Fig. 1. Angular dependence of the relative number of particles moving in the DCh regime ⟨111⟩ ⟶ (110) for 500-keV protons in 450-nm-thick Au crystal at 48 K (thin solid line) and 300 K (thick solid line). Arrows indicate the temperature-dependent boundary Barrett angles θ_B. Dashed curve shows the relation $\varphi^{cr} \sim \theta^{-2/3}$ valid for particle dynamics in the DCh regime [2].

chain). Within the framework of the trajectory integral method [5] for nuclear scattering, we obtain

$$\Omega_n^2(\varepsilon_\perp, b_\perp, u_\perp) = \left\{\frac{\delta\Omega_n^2}{\delta z}\right\}_{\mathrm{R}} m_{\Omega n}\Delta z;$$

$$m_{\Omega n} = \frac{\langle\Delta z\rangle}{\Delta z}\left[\eta_1\frac{9u_\perp^2 a_{\mathrm{TF}}^2}{L_n}(p_1 + p_2 + p_3) + \frac{2r_0\eta_2}{\sqrt{\pi u_\perp^2}}\exp\left(-\frac{b_\perp^2}{u_\perp^2}\right)\right], \quad (1)$$

$$p_1 = \frac{2r_{\mathrm{mb}}^2 + 3a_{\mathrm{TF}}^2 + 3r_{\mathrm{mb}}^2 R_c}{2R_c^3 r_{\mathrm{mb}}^3 (r_{\mathrm{mb}} + R_c)^3},$$

$$p_2 = \frac{11r_{\mathrm{mb}}^2 + 24a_{\mathrm{TF}}^2 + 9r_{\mathrm{mb}}^2 R_c}{4R_c^5 r_{\mathrm{mb}}(r_{\mathrm{mb}} + R_c)^3},$$

$$p_3 = \frac{5}{8R_c^7}; \quad R_c = r_{\mathrm{mb}}^2 + 3a_{\mathrm{TF}}^2,$$

where $u_\perp$ is the rms amplitude of transverse oscillations of atoms in the crystal at a given temperature T; $\{\delta\Omega_n^2/\delta z\}_{\mathrm{R}}$ is the average rate of multiple nuclear scattering of ions in the regime of random motion in the crystal; a_{TF} is the Thomas–Fermi screening length; and Δz is the length of ion interaction with the atomic chain along its z axis. The value of $m_{\Omega n}$ is represented as a sum of contributions due to the many-body and monoatomic mechanisms of particle scattering in the crystal, with the coefficients $\eta_1(r_{\mathrm{m}}) = 1 - \eta_2(1 + r_{\mathrm{m}}^2/u_\perp^2)$ and $\eta_2 = \exp(-r_{\mathrm{m}}^2/u_\perp^2)$. The maximum approach (minimum distance) $r_{\mathrm{m}}(\varepsilon_\perp)$ to the axis of the atomic chain for $b_\perp = 0$ in the case of a continuous Lindhard potential of this chain, with allowance for this potential being zero at the boundary of the Wigner–Seitz cell (i.e., at $r_\perp = r_0 = 1/\sqrt{\pi N d}$, where N is the number density of atoms in the crystal, d is the period of the atomic chain), for the transverse energy $\varepsilon_\perp = \varepsilon_{\perp 0} = 2\theta_0^2/\theta_{\mathrm{L}}^2$ (where $\theta_{\mathrm{L}} \equiv \psi_1$ is the Lindhard critical angle [3]) is given by the formula

$$r_{\mathrm{m}}^2(\varepsilon_\perp) = \frac{3a_{\mathrm{TF}}^2}{\beta\exp(\varepsilon_\perp) - 1}, \quad \beta \approx 1 - \frac{3a_{\mathrm{TF}}^2}{r_0^2}. \quad (2)$$

Previously [5], analogous formulas were obtained for the drag and multiple scattering of electrons characterized by the mean square angle Ω_e^2 dependent on the trajectory integrals. These formulas and Eqs. (1) were checked by simulation of the electron scattering from an isolated atomic chain using the method of binary collisions with atoms and showed acceptable accuracy for variation of the parameters within broad limits. In the calculations presented below, the random angle of multiple scattering was realized assuming that the above mean square angles can be added to obtain the dispersion $\Omega^2 = \Omega_n^2 + \Omega_e^2$ of the normal Gaussian noise when playing the random angular deviation from the particle trajectory in the continuous potential. It was shown [5] that this quantity serves the so-called fractal trajectory (in terms of Migdal, see [6]). Along with the angular deviation, we have considered the random spatial deviation during the multiple scattering of particles in accordance with the Fermi formula (see [6]). These values, together with Eqs. (1), were taken into account at the moments when particles pass from one Wigner–Seitz cell to another.

The elastic scattering of particles in the continuous potential was described analytically [5] as rotation about the atomic chain axis (i.e., as variation of the azimuthal angle with conservation of the transverse particle energy $\varepsilon_\perp$). This allowed us to model the transport of particles in the crystal in the adopted approximation of binary collisions with atomic chains at a considerable velocity, making it possible to study the case of “thick” crystals (i.e., with thickness comparable with the normal projected range R_{p}).

Calculation results. Temperature-dependent calculations for 500-keV protons in the ⟨111⟩ axial channel of a 450-nm-thick gold (Au) crystal (Fig. 1) showed that, in a broad range of initial polar angles, the number of particles (selected from the total flow) moving in the DCh regime at 300 K is significantly greater than that at 48 K. Therefore, an increase in the crystal temperature favors the transitions from the NCh to DCh regime. Such transitions, referred to below as volume rechan-

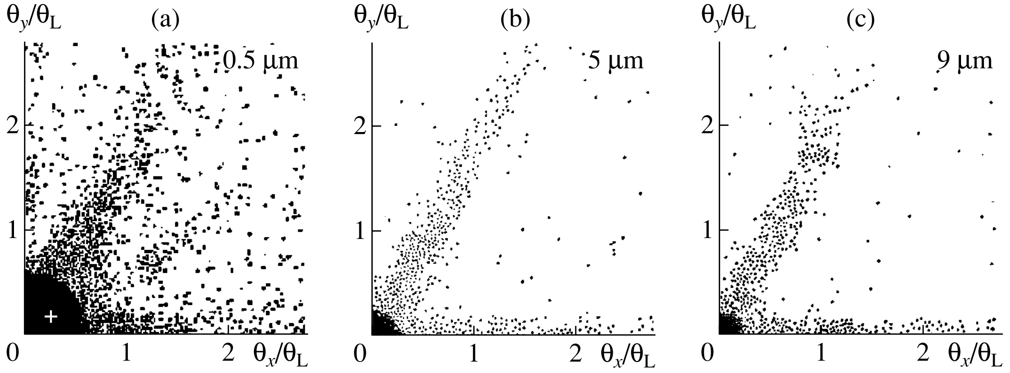

Fig. 2. Fragments of the angular distributions of 1-MeV protons scattered at 300 K in a gold single crystal at various depths (μm): (a) 0.5; (b) 5; (c) 9. The beam is incident at $\theta_0 = 0.32\theta_L$ relative to the ⟨111⟩ axis and $\varphi_0 = 20°$ relative to the (110) plane (the direction of incidence is indicated by the cross in (a); statistics, $N_0 = 9000$).

neling to double channeling regime, are manifested for the motion of particles at all depths in the crystal, thus significantly modifying the observed scenario of dechanneling.

As an example, let us consider the evolution of the angular distributions of protons with an initial energy of 1.0 MeV in the ⟨111⟩Au axial channel at 300 K for incidence angles within the region of axial channeling angles but outside the region of the DCh regime ($\theta_0 = 0.32\theta_L$, $\varphi_0 \sim 0.4$). Figure 2 shows a sequence of two-dimensional angular distributions corresponding to increasing thickness of the penetrated layer (in one quadrant). The origin of coordinates in Fig. 2 corresponds to the ⟨111⟩ axis. In addition to superchanneling and NCh regime (a spot at the origin), the distribution reveals a DCh regime at the {110} planes observed at the azimuthal angles $\varphi = \arctan(\theta_y/\theta_x) = 0$ and 60°. The manifestation of {211} planes, observed in the distribution for a relatively small depth of 0.5 μm at $\varphi = 30°$ and 90°, is absent in the patterns for the greater depths. An increase in the depth up to $1.5R_p$ ($R_p = 5.5$ μm [7]) is accompanied by angular diffusion and increase in the average transverse energy of particles, their dechanneling (in terms of the existing statistical theory) and stopping and by a new phenomenon: the appearance and accumulation of particles in the DCh regime at a strong plane, including particles moving at the angles $\theta > \theta_L$.

Figure 3 shows another example for 2-MeV protons moving in the vicinity of the ⟨111⟩ direction in tungsten (W) for the initial condition $\varepsilon_{\perp 0} \sim 8$. According to the existing theory, this corresponds to a regime of motion not controlled by the crystal lattice. Here, it is interesting to note the effect of superstrong scattering (Fig. 3a), which was previously interpreted within the framework of the statistical equilibrium model [8] and beyond this framework, with allowance for NCh at higher transverse energies [2]. At the same time, the pattern for a depth on the order of one-third of the projected range reveals the population of the channeled states where, besides well-channeled particles, there is a considerable amount of particles moving in the DCh regime. At a still greater depth ($\sim R_p$), the total number of particles in the channeled state amounts to about 20% of the total incident number, which corresponds to the experimental distribution of stopped ions in the case of boron ran-

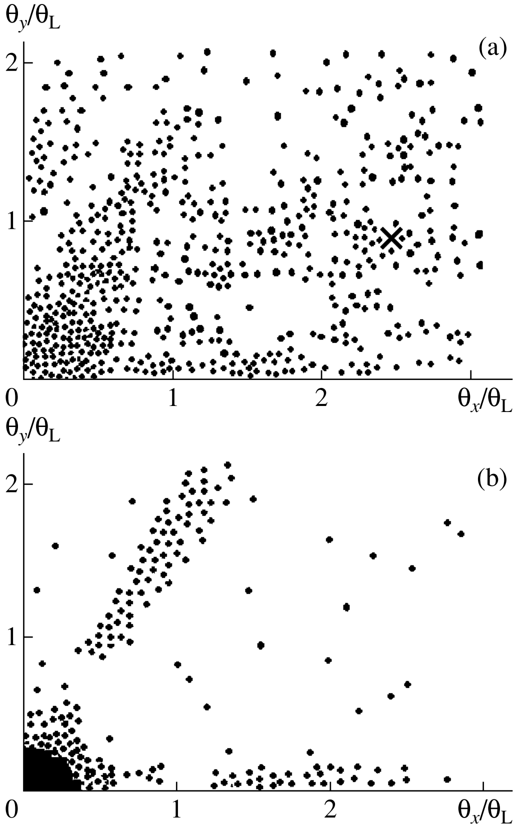

Fig. 3. Fragments of the angular distributions of 2-MeV protons scattered at room temperature in a tungsten single crystal at various depths (μm): (a) 1; (b) 20 ($\sim 1.4R_p$ [10]). The direction of incidence indicated by the ross in (a) corresponds to the dimensionless energy $\varepsilon_{\perp 0} = 2\theta_0^2/\theta_L^2 \sim 8$; statistics, $N_0 = 3000$.

domly implanted into silicon [9]. Note also that, for superlarge depths ~1.5R_p (Fig. 3b), only the channeled fraction is observed in various regimes and, in the region of resonance dechanneling angles, there is a clearly pronounced dip in population of the DCh regime for angles in the vicinity of the atomic plane.

The existence of the transition from random motion to channeling substantially distinguishes the random motion in a crystal from that in an amorphous body, in addition to the aforementioned volume rechanneling manifestations. The existence of this phenomenon is confirmed by experimental data on the profiles of randomly implanted ions observed in the implantation-doped semiconductors (see, e.g., [9]), where the so-called supertails were observed (in contrast to amorphous targets) in the concentration–depth profiles of stopped ions. However, these peculiarities were traditionally explained in terms of the radiation-stimulated impurity diffusion.

It should be also noted that purely planar channeling is virtually unperturbed in the study of particle channeling dynamics in the crystal consisting of atomic chains. However, there is a significant (in Au, almost twofold) increase in population of the angular vicinity of the atomic plane when the direction of incidence approaches the crystallographic axis, that is, in the DCh regime. This phenomenon may increase the transmission of a bent single crystal for high-energy particles in the regime of atomic plane control (see, e.g., [10]).

Another important conclusion is that the volume rechanneling in a straight crystal is related to a nonlinear dynamics of particles in the crystal and is initiated by the scattering of particles from nuclei of the oscillating atoms (and defects), increasing in intensity with the temperature. This behavior distinguishes volume rechanneling from the well-known and widely used (in experiments with relativistic beams) volume trapping of angle-diverging beams into the regime of channeling in a bent crystal [11, 12].

Thus, the results of computer simulation have proved the important role of transitions between channeling modes—from NCh to DCh and from random channeling to DCh and superchanneling. These transitions are confirmed by experimental data on the so-called channeled stars observed behind a thin crystal—the effect observed long ago [13] but not given explanation so far. Even greater experimental evidence is provided by the data for an uncollimated beam of relativistic particles [14], showing characteristic distributions very close to the patterns presented in Figs. 2 and 3b.

The volume trapping of particles into the DCh regime revealed by our calculations and observed in the experimental distributions [14] may shed new light upon the Sumbaev effect [12]. This phenomenon will be considered in detail in the other publication.

Acknowledgments. One of the authors (A.G.K.) is grateful to the St. Petersburg Institute of Nuclear Physics (Russian Academy of Sciences) for kind invitation to the 2003 Winter Workshop and to the staff of the Neutron Physics Laboratory and especially to V.A. Gordeev and V.V. Fedorov for fruitful discussions.

REFERENCES

1. A. G. Kadmenskiĭ, N. Yu. Lebedev, A. F. Tulinov, *et al.*, in *Proceedings of the 11th All-Union Meeting on Physics of Charge Particles Interaction with Crystals* (Izd. Mosk. Gos. Univ., Moscow, 1982), p. 50.
2. A. G. Kadmenskiĭ and A. F. Tulinov, Poverkhnost, No. 2, 43 (2004).
3. J. Lindhard, Mat. Fys. Medd. Kgl. Dan. Vid. Selsk. **34** (14), 1 (1965).
4. Yu. V. Bulgakov, in *Proceedings of the 7th International Conference on Atomic Collisions in Solids, Moscow, 1977* (Izd. Mosk. Gos. Univ., Moscow, 1981), Vol. 1, pp. 41–44.
5. A. G. Kadmenskiĭ and V. V. Samarin, Poverkhnost, No. 5, 98 (2002).
6. A. I. Akhiezer and N. F. Shul’ga, *High-Energy Electrodynamics of Condensed Media* (Nauka, Moscow, 1993).
7. J. F. Janny, At. Data Nucl. Data Tables **27**, 341 (1982).
8. A. G. Kadmenskiĭ, Fiz. Khim. Obrab. Mater., No. 2 (2004).
9. R. G. Wilson, J. Appl. Phys. **54**, 6879 (1983).
10. A. I. Akhiezer, N. F. Shul’ga, V. I. Truten’, *et al.*, Usp. Fiz. Nauk **165**, 1165 (1995) [Phys. Usp. **38**, 1119 (1995)].
11. V. A. Andreev, V. V. Baublis, E. F. Damaskinskiĭ, *et al.*, Pis’ma Zh. Éksp. Teor. Fiz. **36**, 340 (1982) [JETP Lett. **36**, 415 (1982)].
12. O. I. Sumbaev, Zh. Tekh. Fiz. **57**, 2067 (1987) [Sov. Phys. Tech. Phys. **32**, 1251 (1987)].
13. G. Dearnaley, B. W. Farmery, I. V. Mitchell, *et al.*, Philos. Mag. **18**, 985 (1968).
14. H. Esbensen, O. Fich, G. A. Golovchenko, *et al.*, Phys. Rev. B **18**, 1038 (1978).

Translated by P. Pozdeev

Technical Physics Letters, Vol. 30, No. 7, 2004, pp. 545–547. Translated from Pis'ma v Zhurnal Tekhnicheskoĭ Fiziki, Vol. 30, No. 13, 2004, pp. 34–39.
Original Russian Text Copyright © 2004 by Kornich, Betz, Zaporojtchenko, Belaya.

Simulation of Low-Energy Argon Ion Scattering from Surface Copper Clusters

G. V. Kornich*, G. Betz, V. I. Zaporojtchenko, and N. I. Belaya
Zaporozhye National Technical University, 69063 Zaporozhye, Ukraine
Institut für Allgemeine Physik, Technische Universität Wien, A-1040 Wien, Austria
Technische Fakultät, Christian Albrechts Universität, 24143 Kiel, Germany
**e-mail: gkornich@zntu.edu.ua*

Received January 26, 2004

Abstract—The scattering of normally incident 200-eV Ar^+ ions from individual clusters consisting of 13 and 39 copper atoms on a (0001) graphite surface was simulated by the molecular dynamics method. The angular distribution of scattered argon ions and their energies and reflection coefficients are discussed. *© 2004 MAIK “Nauka/Interperiodica”.*

Recently [1, 2], we suggested to evaluate the coverage of a graphite surface by copper clusters using the flux of argon ions scattered from this target. In order to elucidate the mechanisms and laws of the scattering of argon ions from surface clusters of copper, we have used the molecular dynamics (MD) method [3] to simulate the interaction of normally incident 200-eV Ar^+ ions with individual clusters of copper situated on the (0001) graphite surface. The model clusters comprised 13 (13Cu) and 39 (39Cu) copper atoms on graphite substrates consisting of two atomic layers, each containing 792 and 1144 carbon atoms, respectively. The method of creation of a two-component system of the copper cluster–graphite substrate type and the MD algorithm employed were described in [1]. For both clusters, we simulated 2000 events of interaction with incident argon ions and the target, each event being traced for 0.3 ps. During creation of the cluster–substrate system, the free relaxation of atomic planes in the substrate at the stage of cluster rearrangement was allowed (in contrast to [1]) only in the directions along the (0001) planes. A part of Ar^+ ions, which were scattered from the cluster at a polar angle (measured relative to the external normal to the substrate surface) greater than 90°, were not reflected from the model substrate because of its finite size.

The copper clusters of both types, 13Cu and 39Cu, possess substantially different atomic structures. Direct interaction of the 13Cu cluster with the substrate involves only three Cu atoms and virtually does not influence the cluster shape. In contrast, the structure of the 39Cu cluster is modified due to the interaction with the carbon substrate in accordance with the (0001) graphite surface structure [1]. As a result, atoms in the 39Cu cluster were arranged in two to three layers in the direction of normal to the substrate surface.

There are two possible scenarios for the process of ion interaction with a surface cluster of copper: (i) scattering without substantial interaction with the substrate and (ii) scattering on the cluster followed by reflection from the substrate. In both cases, two mechanisms of reflection of an impinging ion from the cluster can be operative: (i) an essentially pair interaction of the ion with one atom in the cluster and (ii) a many-body interaction of the ion (simultaneously or sequentially) with several atoms in the cluster. For the same angle of reflection, the average energy of an ion scattered according to the many-body mechanism is greater than that in the case of the pair mechanism.

Figure 1 shows the model distributions of the probability of Ar^+ ion scattering with respect to the polar angle [number of incident ions scattered within a unit (in this calculation, one degree) polar angle interval normalized to the total number of incident ions] for individual 13Cu (points *1*) and 39Cu (points *2*) clusters (the corresponding curves *1* and *2* were constructed by plotting segments of linear approximations for every 10 sequential points). In addition, Fig. 1 presents the angular dependences of the average energies of scattered ions determined as the total energies of ions scattered within a unit polar angle interval divided by the total number of incident ions scattered within this angular interval (points *4* and *3* and the corresponding curves *1d* and *1c*, respectively). As can be seen from these data, a significant increase in the probability of scattering and the average energy of scattered ions is observed for both clusters in the region of polar angles above 35°–45°.

In order to elucidate the reason for a polar angle of 35°–45° to be critical for scattering, we have simulated the interaction of a clean (0001) graphite surface with Ar^+ ions for various polar angles of incidence between

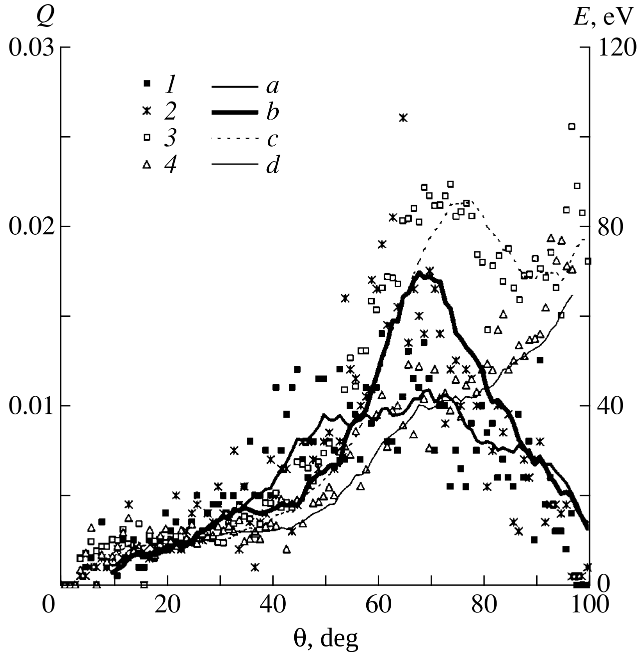

Fig. 1. Plots of the scattering probability Q (left axis, points *1* and *2* and curves *a* and *b*, respectively) and average energy E of scattered ions (right axis, points *3* and *4* and curves *c* and *d*, respectively) versus the polar angle of scattering for 200-eV Ar^+ ions normally incident onto 13Cu (points *1* and *4* and curves *a* and *d*, respectively) and 39Cu (points *2* and *3* and curves *b* and *c*, respectively).

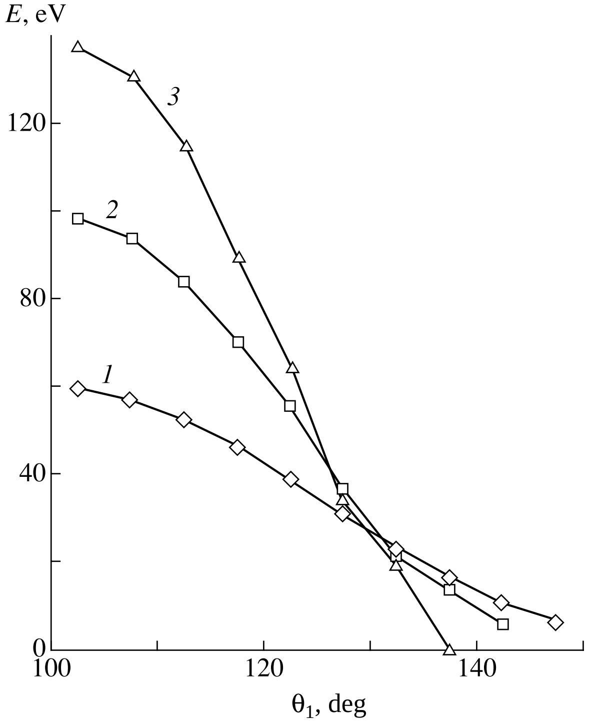

Fig. 2. Plots of the energy E of reflected ions versus the polar angle of incidence θ_1 for Ar^+ ions incident onto the (0001) graphite surface at various initial energies (eV): (*1*) 60; (*2*) 100; (*3*) 140.

100° and 180° (with a 5° step) and various primary ion energies. It was found that the angle of reflection for 60-, 100-, and 140-eV ions only slightly (within ~1°) differs from the angle of incidence below the critical angles 130°, 120°, and 110°, respectively; the final energies of Ar^+ ions monotonically decrease with increasing polar angle (Fig. 2). Increase in the polar angle of incidence above the critical values is accompanied by sharp deviations of the angle of reflection from the angle of incidence and by significantly increased losses in the ion energy. These peculiarities in the ion–substrate interaction are related to local damage of the atomic layer of graphite taking place for the polar angles of incidence exceeding the critical values. Further increase in the polar angle of incidence leads to penetration of ions into the substrate. The results of simulations obtained for the clean graphite surface qualitatively agree with the experimental data [4], according to which 43.5 eV is the threshold energy for penetration of the normally incident Ar^+ ions into a (0001)-oriented graphite layer.

Thus, in the region of the polar angles of reflection below 45°, the probability of ion scattering is determined primarily by the pair interaction between Ar^+ ion and Cu atom, which is accompanied by considerable losses in the ion energy. However, according to Fig. 1, such ions account for only a small fraction of the total number of reflected ions and the scattering intensity. The average energies of ions scattered within this interval of polar angles rather insignificantly differ for the 13Cu and 39Cu clusters. For greater polar angles of scattered ions, a significant contribution is due to the ions with greater energies (up to 80 eV). Considerable kinetic energies retained by the scattered ions are possible, provided that the second (many-body) mechanism of interaction between an incident ion and atoms in the clusters is operative, with a resulting polar angle of scattering above 90° and the subsequent reflection from the substrate surface (also as a result of many-body interaction). This character of scattering is manifested by the resulting maximum of the average energy of reflected ions observed in the region of polar angles 70°–90° (Fig. 1). On the average, the reflected ions retain ~10–20% of their initial energy.

A comparison of the intensity of Ar^+ ion scattering by large angles from the 13Cu and 39Cu clusters (Fig. 1) shows that the average energy of scattered ions is significantly lower for the former cluster than for the latter one. This is related to the fact that the probability of effective many-body interactions (especially, with sequential events) between Ar^+ ions and Cu atoms is lower for the 13Cu cluster than for the 39Cu cluster because the former is much smaller than the latter. An increase in the average energy of scattered ions for polar angles exceeding 90° and significant local deviations of the corresponding points in the probability of scattering from the approximating curves are related to the finite size of the substrates, which results in the absence of reflection for a small fraction of incident ions scattered upon interaction with the clusters. The total coefficients of Ar^+ ion scattering in the model under consideration were 0.6 and 0.68 for 13Cu and 39Cu clusters, respectively. The coefficients of reflection in the range of polar angles below 90° during the simulation time for the 13Cu and 39Cu clusters were 0.56 and 0.64, respectively. The other Ar^+ ions penetrated into the substrate, whereas no argon ions were found in copper clusters after a 0.3-ps evolution of the model system.

REFERENCES

1. G. V. Kornich, G. Betz, V. I. Zaporojtchenko, and A. I. Bazhin, Pis'ma Zh. Tekh. Fiz. **29** (22), 33 (2003) [Tech. Phys. Lett. **29**, 938 (2003)].
2. G. V. Kornich, G. Betz, V. I. Zaporojtchenko, and A. I. Bazhin, in *Proceedings of the 15th International Conference "Interaction of Ions with Surface," Moscow–Zvenigorod, 2003*, Vol. 1, pp. 65–68.
3. J. M. Haile, *Molecular Dynamics Simulation—Elementary Methods* (Wiley, New York, 1992).
4. D. Marton, H. Bu, K. J. Boyd, *et al.*, Surf. Sci. Lett. **326**, 489 (1995).

Translated by P. Pozdeev

Technical Physics Letters, Vol. 30, No. 7, 2004, pp. 548–549. Translated from Pis'ma v Zhurnal Tekhnicheskoĭ Fiziki, Vol. 30, No. 13, 2004, pp. 40–44.
Original Russian Text Copyright © 2004 by Demkin, Dokov, Privalov.

Peculiarities of Using Laser Diodes in Linear Measurements

V. N. Demkin, D. S. Dokov, and V. E. Privalov*
St. Petersburg State Technical University, St. Petersburg, 195251 Russia
**e-mail: VEP@peterlink.ru*

Received January 12, 2004

Abstract—The position of the emitting region of a laser diode depends on the working current. This phenomenon, as well as the polarization of radiation, may influence the accuracy of linear measurements using such lasers. © *2004 MAIK “Nauka/Interperiodica”.*

Linear measurements on the reference level require using the most coherent radiation sources—stabilized gas discharge lasers [1, 2]. In many cases, however, laser diodes can be used as well. Such applications include, in particular, triangulation meters of linear dimensions. The dependence of the accuracy of laser triangulation meters on various factors was considered in [3–5], but the effect of laser radiation parameters remained practically unstudied.

Information about the measured dimension is provided by coordinates of the center of a probing radiation spot, which are determined using the image of this spot on a calibrated charge coupled device (CCD) photodetector scale. The accuracy of coordinate determination depends not only on the method used for this purpose but on the stability of the power density distribution (PDD) in the spot image as well. Variations of the working current significantly influence all characteristics of a laser diode, thus changing the PDD in the laser spot image on the photodetector scale and, accordingly, the measured coordinates of the center of the probing radiation spot. For example, investigation of this effect using laser diodes of the Lumex Company showed (Fig. 1) that a change in the working current within 3 mA may lead to a shift in the spot image center by 0.5 pixel (for a CCD photodetector scale with 2048 pixels, this corresponds to 0.025%).

The most probable factors responsible for the current-dependent shift of the PDD are mode competition and the so-called speckle noise [3]. Sharp variations in coordinates of the laser spot center (Fig. 1) suggest that mode competition is of primary importance. This phenomenon, together with the speckle noise, poses physical limitations on the maximum possible accuracy of laser triangulation measurements.

The output radiation of a semiconductor laser is usually polarized. The orientation of the polarization plane influences the character of reflection from the object surface. The reflection coefficient depends both on the incidence angle and on the azimuthal angle between the polarization vector and the plane of incidence [6, 7]. Calculation of the effect of polarization characteristics on the reflection coefficient is rather difficult because the object surface is not always smooth. The accuracy of such measurements is determined to a considerable extent by the change in the reflection coefficient during scanning of the object surface with a beam of the laser triangulation meter. For this reason, we have experimentally studied the effect of polarization characteristics on the reflection coefficient of the rolling surface of a railway car wheel.

In order to measure the dependences of the reflection coefficient on the angle of incidence and the shape of the wheel surface, we scanned the wheel rim surface with a probing laser beam. As can be seen from the data presented in Fig. 2, the obtained profiles exhibit sharp

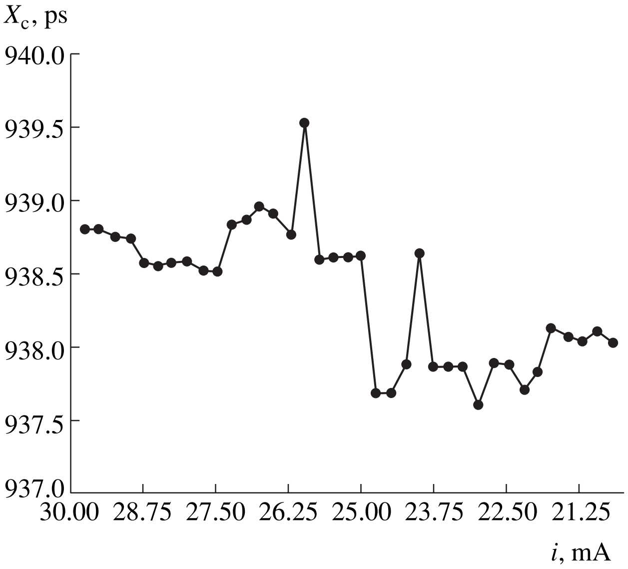

Fig. 1. Plot of the laser spot center coordinate X_c versus laser diode current i.

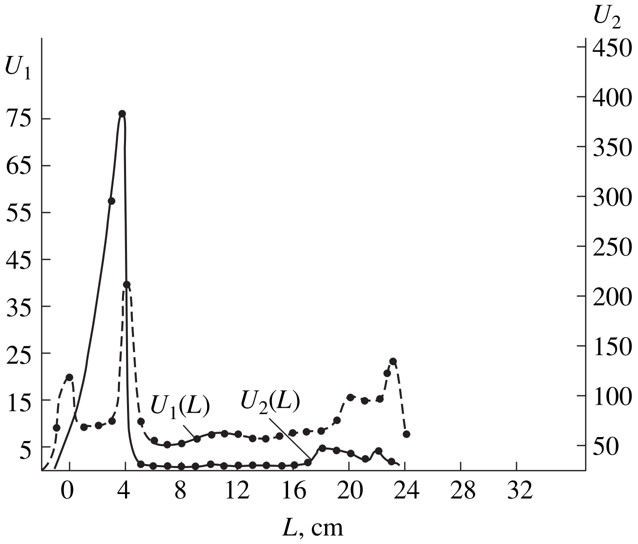

Fig. 2. Profiles of the reflection coefficient R measured by scanning over the rolling surface of a railway car wheel with a laser beam polarized (U_1) in the plane of incidence and (U_2) perpendicularly to this plane.

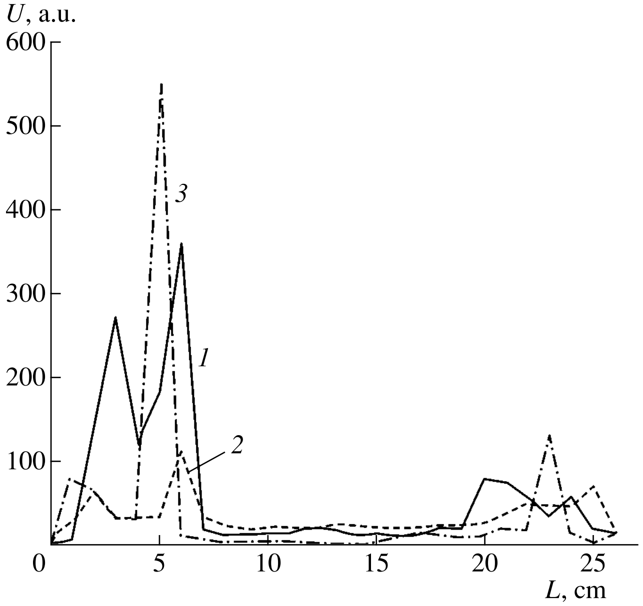

Fig. 3. Profiles of the reflected signal intensity U measured by scanning over the rim surface of a railway car wheel with a laser beam of variable diameter (mm): (*1*) 0.7; (*2*) 3.5; (*3*) 5.

maxima in the region where the angle of incidence is close to the angle of observation. However, the magnitude of this maximum significantly depends on the orientation of polarization plane in the incident laser beam. The maximum peak and minimum variations of intensity of the reflected signal are observed when the incident laser beam is polarized perpendicularly to the plane of incidence.

One of the most important parameters determining the accuracy of laser triangulation measurements is the diameter of the probing laser beam. One may suggest that the smaller this diameter, the higher the measurement accuracy. However, this conclusion is valid only for a surface with isotropic roughness. Real surfaces quite frequently exhibit scars, cleavages, blisters, burrs, etc., that is, possess a fractal character. The results of investigations show that, in such cases, the optimum probing beam diameter depends on the properties of a particular surface. For the rolling surface of a railway car wheel, the profiles of reflected signal intensity measured using laser beams of various diameters are substantially different (Fig. 3). The maximum dynamic range and maximum peak of intensity are observed for a focused laser beam. An increase in the laser beam diameter above 3–4 mm did not lead to a decrease in the dynamic range. The dependence on the beam diameter can be explained by the fractal character of the wheel surface, whereby the roughness dimensions are comparable with the beam spot size. In this particular case, the optimum probing beam diameter is 3–4 mm.

REFERENCES

1. V. E. Privalov, *Gas Discharge Lasers in Naval Measuring Instrumentation* (Sudostroenie, Leningrad, 1977).
2. V. E. Privalov, *Gas Discharge Lasers in Measuring Instrumentation* (Sudostroenie, Leningrad, 1989).
3. R. Dorsch, G. Hausler, and J. Herrmanb, Appl. Opt. **33**, 1306 (1994).
4. S. V. Plotnikov, Avtometriya, No. 6, 58 (1995).
5. V. V. Vertoprakhov, Avtometriya, No. 6, 64 (1995).
6. E. I. Butikov, *Optics* (Vysshaya Shkola, Moscow, 1986).
7. V. I. Butkevich, V. N. Demkin, and V. E. Privalov, Opt. Spektrosk. **62**, 140 (1987) [Opt. Spectrosc. **62**, 86 (1987)].

Translated by P. Pozdeev

Technical Physics Letters, Vol. 30, No. 7, 2004, pp. 550–552. Translated from Pis'ma v Zhurnal Tekhnicheskoĭ Fiziki, Vol. 30, No. 13, 2004, pp. 45–50.
Original Russian Text Copyright © 2004 by Kal'yanov.

Chaotic Attractors Formed Using Bistable Systems

Er. V. Kal'yanov

Institute of Radio Engineering and Electronics (Fryazino Branch), Russian Academy of Sciences, Fryazino, Moscow oblast, Russia

e-mail: erast@ms.ire.rssi.ru

Received November 10, 2003

Abstract—A new method of nonautonomous excitation of chaotic oscillations is proposed which makes use of bistable systems. The formation of an original chaotic attractor in a bistable system, representing decaying motions between two basins of attraction, is demonstrated by numerical methods. © *2004 MAIK "Nauka/Interperiodica".*

Bistable systems are widely used in various fields of science and technology. In recent years, such systems have been extensively studied in view of the possible manifestations of the phenomenon of stochastic resonance (see, e.g., [1]). This study was devoted to the possibility of using bistable systems for the generation of dynamical chaos. The formation of chaotic oscillations in a bistable system was analyzed by numerical methods using a relatively simple algorithm called the chaotization feedback algorithm.

Let us construct a mathematical model describing the formation of chaotic oscillations using normalized equations of a bistable system [2],

$$\begin{aligned} dx/dt &= y - g(x), \\ dy/dt &= -\delta(x+y), \end{aligned} \tag{1}$$

where $g(x)$ is a nonlinear characteristic of the active element and δ is a constant coefficient. In order to provide for the existence of two stable states in system (1), the nonlinear characteristic $g(x)$ can be specified in terms of various functions exhibiting a decaying region, for example, a cubic function [2]. Even simpler approximation for the characteristic of a nonlinear element is offered by a circular function. In this case, system (1) behaves like a usual triggering device in which autooscillations are impossible. Such a system features two singular points of the stable focus type determining the stable states of the system. These points are separated by a separatrix passing through a saddle.

It was established that oscillations (even chaotic) in system (1) can be excited, provided that a feedback is set according to a certain algorithm. Equations of the new system can be obtained using an external harmonic drive signal $f(t)$ determined by the commutation conditions. In this case, approximating nonlinearity $g(x)$ by a circular function, we have

$$\begin{aligned} dx/dt &= y + \mu \arctan(x), \\ dy/dt &= -\delta(x+y) + f(t), \end{aligned} \tag{2}$$

where

$$f(t) = \begin{cases} ax\cos(\omega_0 t), & x > c, \\ bx\cos(\omega_0 t), & x < d; \end{cases} \tag{3}$$

μ, a, b, c, d are positive coefficients, and ω_0 is the harmonic drive signal frequency.

Equations (2) with conditions (3) determine the mathematical model of a nonautonomously excited chaotic system featuring a special kind of feedback—chaotization feedback algorithm—whereby the introduced external signal $f(t)$ depends not only on the external action as such but on the variable $x(t)$ as well. Conditions (3) define the change in the function $f(t)$ on reaching the corresponding values of x. The model described by Eqs. (2) and (3) is sufficient for the excitation of chaos in digital systems. Creation of analog chaotic systems based on a bistable system would require additional investigation including an experimental part, which goes beyond the scope of this study.

The numerical analysis was performed using the fourth-order Runge–Kutta method with an integration time step of $t = 0.02$. The initial values of the variables were taken equal to 0.1. The parameters of a bistable system and the coefficients in Eqs. (2) and (3) for the calculation were set as follows: $\mu = 2$, $\delta = 1.6$, $\omega_0 = 3$, $a = -1.92$, $b = 2.08$, $c = 1.6$, and $d = -1.5$.

Figure 1 shows fragments of the time series of the process of $x(t)$ oscillations in the above system. Figure 2 presents an attractor map (a) and the power S spectrum (b)

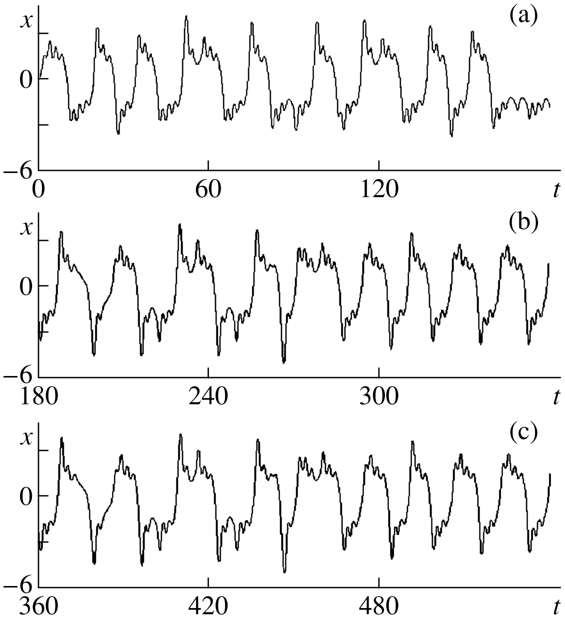

Fig. 1. Fragments of the time series of the oscillatory process $x(t)$ observed in various time intervals $t \in [0, 180]$ (a), [180, 360] (b), and [360, 540] (c).

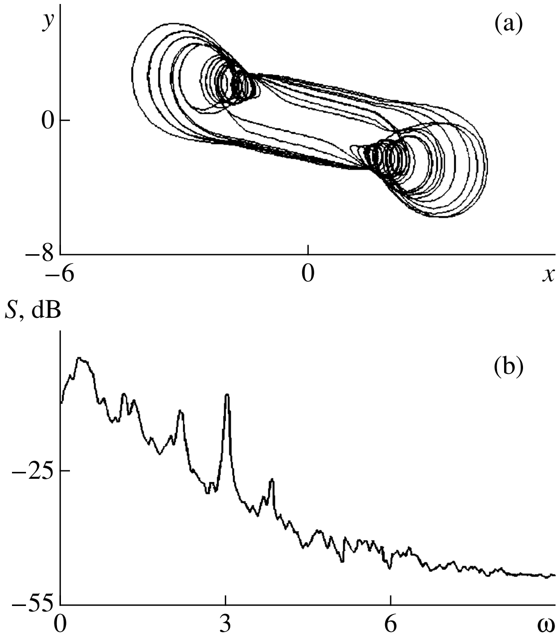

Fig. 2. A bistable system with chaotization feedback algorithm: (a) phase portrait for $t \in [360, 540]$; (b) power spectrum.

of this system. As can be seen from these data, the system described by Eqs. (2) and (3) exhibits complex oscillations. Both the fragments of time series and the attractor and power spectrum show evidence of chaotic motions in this system.

The observed oscillatory process reflects the switching of motions between two basins of attraction, which is a manifestation of bistability. The oscillations are decaying and are switched in an irregular manner between the x_1 and x_2 values representing singular points (stable foci) of the bistable system corresponding to the parameters selected. For the given values of μ and δ, the stable states correspond to $x_1 = 2.33$ and $x_2 = -2.33$.

The chaotic attractor exhibits a structure reflecting the presence of two basins of attraction and is determined by the switching of oscillations between these basins. This switching of decaying motions distinguishes the "bistable" attractor depicted in Fig. 2a from the well-known attractor of the double scroll type [3]. The observed power spectrum is continuous and shows evidence of a good mixing of the phase trajectories, although there is a resonance increase in the spectral power density of chaotic oscillations at a frequency of $\omega = \omega_0 = 3$.

Chaotic motions can also be formed using bistable systems of other types. In particular, it is possible to use an overdamped oscillator, for which a stochastic resonance was studied in [1]. In this case, the equation describing the bistable system has the following form [1, 4]:

$$dx/dt = x(\alpha - \beta x^2) + f(t). \quad (4)$$

This equation determines the motion of a particle in the field with a bistable potential under the action of the external driving force $f(t)$. Parameters α and β characterize the depths of the potential wells.

For a harmonic driving force $f(t)$ of sufficiently large amplitude in Eq. (4), a particle exhibits periodic passages from one potential well to another and vice versa. By setting function $f(t)$ in the form of a chaotization feedback algorithm according to relation (3), it is possible to provide for a chaotic variation of $x(t)$. The chaotization of oscillations in the joint solution of Eqs. (3) and (4) is observed, for example, with the following values of parameters: $\alpha = 1$, $\beta = 0.2$, $a = -4.3$, $b = 4.5$, $c = 1.6$, $d = -1.4$, and $\omega_0 = 3$. This case corresponds to a positive characteristic Lyapunov exponent $\lambda = 0.48$. The time series of chaotic oscillations exhibit irregular Poincaré returns with time.

The results presented above show evidence of the possibility of obtaining chaotic motions in bistable systems. The proposed method, based on the chaotization feedback algorithm, opens prospects for the transformation of regular oscillations into chaotic using various bistable systems.

A natural question arises concerning the possibility of using the proposed feedback algorithm for the chaotization of oscillations in an autooscillatory system operating in the regular regime. This is also possible, as was recently illustrated [5] for an autooscillatory system with inertia, in which only quasi-harmonic oscillations are excited in the absence of the chaotization feedback algorithm.

Acknowledgments. This study was supported by the Russian Foundation for Basic Research, project no. 01-02-17529.

REFERENCES

1. O. V. Gerashchenko, Pis’ma Zh. Tekh. Fiz. **29** (6), 82 (2003) [Tech. Phys. Lett. **29**, 256 (2003)].
2. E. V. Kal’yanov, Pis’ma Zh. Tekh. Fiz. **25** (6), 1 (1999) [Tech. Phys. Lett. **25**, 207 (1999)].
3. C. W. Wu, T. Yang, and L. O. Chua, Int. J. Bifurcation Chaos Appl. Sci. Eng. **6**, 455 (1996).
4. L. S. Pontryagin, A. A. Andronov, and A. A. Vitt, Zh. Éksp. Teor. Fiz. **3**, 165 (1933).
5. E. V. Kal’yanov, Nelin. Mir **1**, 45 (2003).

Translated by P. Pozdeev

Technical Physics Letters, Vol. 30, No. 7, 2004, pp. 553–556. Translated from Pis'ma v Zhurnal Tekhnicheskoĭ Fiziki, Vol. 30, No. 13, 2004, pp. 51–58.
Original Russian Text Copyright © 2004 by Fadeeva, Volyar.

Vectorial Topological Dipole in Output Radiation of a Fiber Optical Coupler

T. A. Fadeeva and A. V. Volyar*
Taurida National University, Simferopol, Ukraine
**e-mail: volyar@ccssu.crimea.ua*

Received October 20, 2003; in final form, February 8, 2004

Abstract—It is experimentally and theoretically demonstrated that a vectorial topological dipole is formed in the radiation field of the main channel of a fiber optical coupler. The dipole consists of two polarization umbilics—of the star and lemon or the star and monstar types—and retains its structure in the course of radiation propagating along the fiber, whereby the topological index remains unchanged. Using a polarization filter, it is possible to select two identically charged vortices corresponding to these polarized umbilics. © *2004 MAIK "Nauka/Interperiodica".*

Recently [1], it was reported that a fiber optic coupler is an optimum device for separating singular beams (*CV* and *IV* modes [2]) and the fundamental mode HE_{11} in the radiation of a weakly guiding optical fiber [3]. Moreover, such a fiber coupler is capable of selecting typical vectorial singularities from a variety of singular optical phenomena, which are usually leveled in single fibers because of virtually equal energy redistribution between eigenmodes.

This Letter reports on the results of an experimental and theoretical investigation of the evolution of vectorial singularities in the channels of a fiber optical coupler. The key idea of this study consisted in suppressing the undesired influence of the fundamental mode on the character of propagation of the optical vortices formed in one of the coupler channels [1]. This possibility is based on the significant difference in the coefficients of coupling between the higher and lower modes in the adjacent branches. At the same time, it was experimentally found that the HE_{11} mode is suppressed incompletely and its "residues" mediate in the formation of a characteristic polarization singularity—a stable vectorial topological dipole. The properties of such dipoles account for the appearance of a coarse speckle structure sensitive to weak external perturbations in the radiation field of few-mode fibers.

Experiment. Let us consider experimental manifestations of the phenomenon of vectorial topological dipole formation. The experiments were performed with a Y-shaped optical coupler made of quartz fibers. Each fiber was capable of guiding a single HE_{11} mode at a wavelength of $\lambda = 1.33$ μm. The same fiber excited by a linearly polarized light with $\lambda = 0.63$ μm can guide 12 eigenmodes. Preliminary tests showed that fibers of the coupler exhibit a weak linear birefringence $\Delta n \propto 10^{-5}$. Each fiber had a core diameter of $D = 8$ μm and an outer cladding diameter of $d = 110$ μm; the length of the region of effective mode coupling was $h = 0.7$ mm.

In the experimental setup, the fiber coupler formed two arms of a modified Mach–Zehnder interferometer. The input was excited by the circularly polarized radiation of a He–Ne laser focused by a $20^{\times}$ microobjective. A polarization filter placed at the output of the main channel was capable of selecting optical vortices formed in the fiber. The filter comprised a λ/4 plate and a polarizer with an angle of π/4 between their axes. It should be emphasized that radiation at the output of the main channel exhibited a complex distribution of intensity and polarization.

In order to elucidate the principal polarization processes occurring in the main channel of the fiber coupler, we developed a differential Stokes polarimeter capable of changing the distribution of the radiation polarization state in all pixels of the image. The corresponding maps could be processed and displayed by a computer. The Stokes parameters were calculated using the following formulas [4],

$$\begin{gathered} S_0 = I_r + I_l, \quad S_1 = 2I_x - S_0, \\ S_2 = 2I_{\pi/4} - S_0, \quad S_3 = I_r - I_l, \end{gathered} \tag{1}$$

where I_r and I_l are the intensities of the right-hand and left-hand polarized components corresponding to the λ/4 plate oriented along the *y* axis and the polarizer axis making an angle of $\alpha = 3\pi/4$ and $\pi/4$ with the *y* axis, respectively; I_x corresponds to $\alpha = \pi/2$ and the λ/4 plate still oriented along the *y* axis; and $I_{\pi/4}$ was measured for the λ/4 plate making an angle of π/4 with the *y* axis and the polarizer oriented at $\alpha = \pi/4$. The degree of ellipticity Q of the radiation and the angle of orientation ψ of

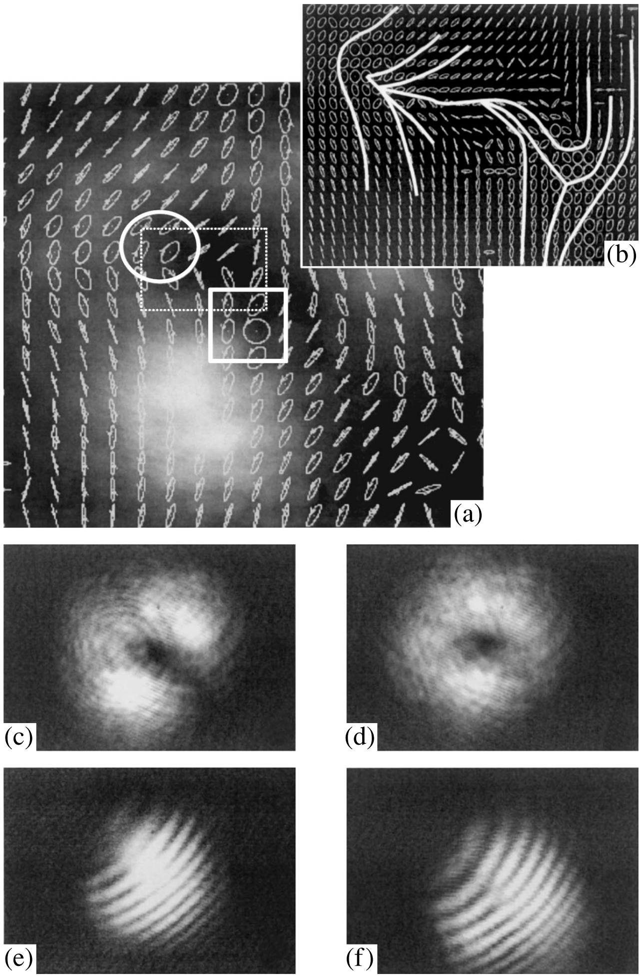

Fig. 1. The typical distribution of polarization states in the radiation field of the main channel of the fiber optical coupler: (a) map of the polarization states (on the background of the light flux intensity distribution); (b) polarization dipole formed by umbilics of the monstar and star types; (c, d) intensity distributions and (e, f) interferograms after a circular polarizer for (c, e) right-hand and (d, f) left-hand circular polarization.

the large semiaxis of the polarization ellipse are given by the formulas

$$Q = \tan\left(\frac{1}{2}\arcsin\left(\frac{S_3}{S_0}\right)\right), \quad \psi = \frac{1}{2}\arctan\left(\frac{S_2}{S_1}\right). \quad (2)$$

Figure 1a shows the typical distribution of polarization in the cross section of radiation field in the main channel on the background of the light flux intensity distribution. The field of the polarization state is conveniently characterized using two regions containing singular points with the right-hand and left-hand circular polarization. In Fig. 1a, these regions (called polarization umbilics [5]) are indicated by the circle and square. Each umbilic comprises a family of integral curves tangent at every point to the large semiaxis of the polarization ellipse. In our case, the umbilics correspond, according to the classification of Nye [5], to singularities of the "star" (situated in the vicinity of the beam axis in Fig. 1a) and "monstar" (situated closer to the topleft corner) types. Using a magnified image in Fig. 1b, it is easy to determine the topological indices of both star (p_s = –1/2) and monstar (p_m = +1/2) umbilics. These singularities form a stable vectorial topological dipole existing (see below) due to the presence of "residues" of the HE_{11} mode incompletely pumped to the second channel. Weak phase perturbations or the field spreading along the fiber lead to rotation of the dipole around the beam axis and induce oscillations of the dipole length, not affecting the general structure of the polarization singularity (the total topological index $s = p_s + p_m = 0$ is constant).

Using the polarization filter comprising a λ/4 plate and a polarizer, it is possible to select the optical vortices corresponding to these umbilics (see the photographs in Figs. 1c and 1d). At first glance, the optical vortices originating from the vectorial topological dipole must possess opposite topological charges. However, the interferograms in Figs. 1e and 1f exhibit the same orientation of the interference "forks," which is evidence that the topological charges are of the same sign. It should also be noted that these vortices cannot be simultaneously selected in the radiation field: they correspond to mutually perpendicular circular polarizations, which cannot be simultaneously attenuated by the same polarization filter.

Theory. The chosen theoretical model corresponds to a weakly guiding step-index fiber with a waveguide parameter of $V < 3.8$, excited by a circularly polarized light. This fiber may guide four eigenmodes: *CV*, TE_{01}, TM_{01}, and (fundamental) HE_{11}. As is known [2], the *CV* mode (or the optical vortex of the fiber) is a superposition of the even and odd HE_{21} modes (in a slightly birefringent fiber, their propagation constants can be considered approximately equal), while the azimuthal symmetric TE_{01} and TM_{01} modes combine into an unstable *IV* vortex. In experiment, the fiber may also feature the modes with an azimuthal index $l = 2$, but their weighing coefficients are negligibly small if the fiber is excited via a coaxial low-aperture microobjective (see Figs. 1c and 1d). For this reason, the theoretical analysis is restricted to the four modes indicated above.

The wave function of the radiation field can be written in the following form [2]:

$$\begin{aligned}\Psi = {} & \mathbf{c}^{+}a_0F_0(R)e^{i\beta_{HE}z} + F_1(R)\{\mathbf{c}^{+}a_1e^{i(\varphi + \beta_{CV}z)} \\ & + a_2[\mathbf{c}^{+}\cos(\delta\beta z)e^{-i\varphi} - i\mathbf{c}^{-}\sin(\delta\beta z)e^{i\varphi}]e^{i(\tilde{\beta} + \delta\beta)z}\},\end{aligned} \quad (3)$$

where $\mathbf{c}^{+}$ and $\mathbf{c}^{-}$ are the unit vectors of the right- and left-hand circular polarization, respectively; a_0, a_1, and a_2 are the weighing coefficients of HE_{11}, *CV*, and *IV*

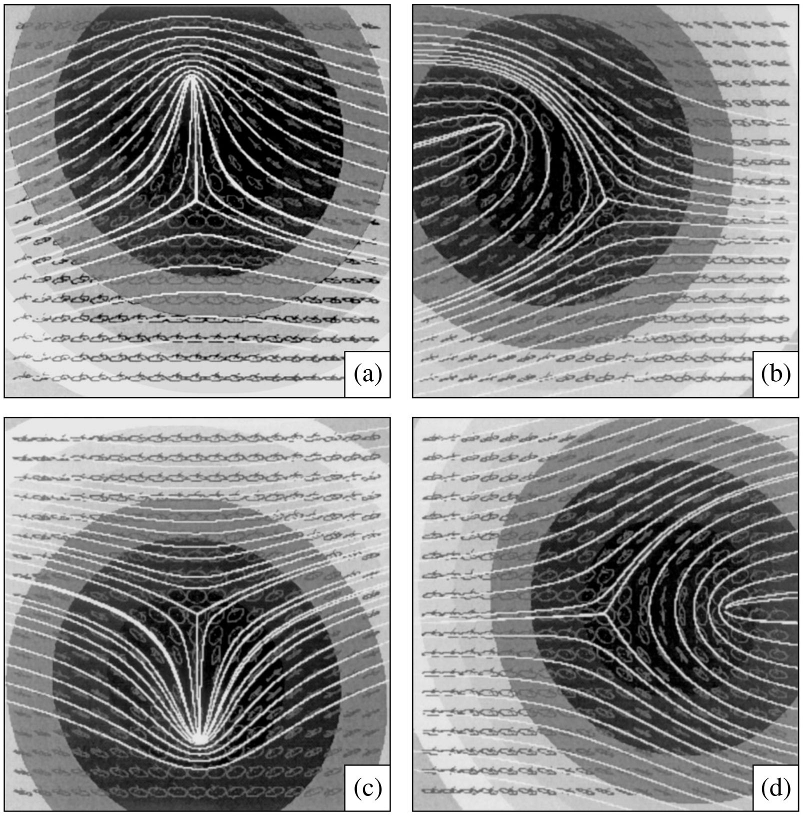

Fig. 2. Evolution of the vectorial topological dipole in the radiation field of the main channel of the fiber optical coupler (the fiber length z was selected so as to provide that the energy of IV mode would be concentrated predominantly in a partial optical vortex with the circular polarization perpendicular to the initial beam polarization). The patterns of polarization umbilics were calculated for the mode weights $a_0 = 0.5$, $a_1 = a_2 = 1$, and the fiber lengths $z = 0.15248$ (a), 0.14955 (b), 0.15143 (c), and 0.15124 m (d).

modes, respectively; β_{HE}, β_{CV}, β_{TE}, β_{TM} are the propagation constants of the corresponding modes; $\delta\beta = (\beta_{TM} - \beta_{TE})/2$, $\tilde{\beta}$ is the scalar propagation constant ($l = 1$);

$$F_0(R) = \begin{cases} \dfrac{J_0(UR)}{J_0(U)}, & R \le 1, \\ \dfrac{K_0(UR)}{K_0(U)}, & R > 1, \end{cases} \qquad F_1(R) = \begin{cases} \dfrac{J_1(UR)}{J_1(U)}, & R \le 1, \\ \dfrac{K_1(WR)}{K_1(W)}, & R > 1, \end{cases}$$

$J_l(x)$ is the lth-order Bessel function of the first kind; $K_l(x)$ is the Macdonald function; $R = r/\rho$; ρ is the radius of the core fiber; and U and W are the waveguide parameters of the core and cladding, respectively, determined from a characteristic equation [3].

Figure 2 illustrates evolution of the vectorial topological dipole upon small variations of the fiber length. It should be noted that the vectorial dipole consists of two polarization umbilics: star–lemon for $z = \pi/(2\delta\beta)$ and star–monstar for the other lengths. Since the topological index of singularity of the lemon type is the same as that of the monstar ($p_l = p_m = +1/2$), the total topological index of the dipole is not changed during the weave propagation. Both these states were established theoretically and observed experimentally. In the above experimental part, we presented data illustrating evolution of the star–monstar dipole. The results of theoretical modeling are presented for fiber lengths corresponding to the star–lemon dipole. As can be seen from Fig. 2, the star umbilic always occurs at the fiber axis, while the lemon umbilic is shifted toward the periphery and rotates around the axis. The distance between these umbilics depends both on the difference $\delta\beta$ of the propagation constants and on the relative weight of the HE_{11} mode. When the fundamental mode is completely pumped to the adjacent channel, the polarization singularities annihilate with the formation of two special lines corresponding to the linear polarization, which are oriented perpendicularly to the optical axis of the fiber [2]. The dynamics of these singularities is described in detail elsewhere [3]. If the weight of HE_{11} mode is comparable with the weight of the other modes, the monstar (or lemon) is displaced to the periphery and not detected in experiment. However, using a fiber coupler, it is possible to control the weighing coefficient of the fundamental mode, thus holding the monstar (or lemon) umbilic in the observation field.

Based on the results of our theoretical and experimental investigation, we have demonstrated that the main structural element in the radiation field of a Y-shaped fiber optical coupler is a vectorial topological dipole consisting of two polarization umbilics—of the star and lemon or the star and monstar types. In the course of propagation, the dipole structure remains unchanged (the total topological index is constant), while the lemon (or monstar) performs oscillatory motions and rotates around the star tightly bound to the fiber axis. The vectorial dipole corresponds to two optical vortices with identical topological charges and mutually perpendicular polarizations, which can be selected using a polarization filter.

REFERENCES

1. A. V. Volyar and T. A. Fadeeva, Pis'ma Zh. Tekh. Fiz. **29** (14), 50 (2003) [Tech. Phys. Lett. **29**, 594 (2003)].
2. A. V. Volyar and T. A. Fadeeva, Opt. Spektrosk. **85**, 295 (1998) [Opt. Spectrosc. **85**, 272 (1998)].
3. A. W. Snyder and J. D. Love, *Optical Waveguide Theory* (Chapman and Hall, London, 1983; Radio i Svyaz', Moscow, 1987).
4. M. Born and E. Wolf, *Principles of Optics*, 4th ed. (Pergamon Press, Oxford, 1969; Nauka, Moscow, 1973).
5. J. F. Nye, *Natural Focusing and Fine Structure of Light* (Inst. Phys., Bristol, 1999).

Translated by P. Pozdeev

Technical Physics Letters, Vol. 30, No. 7, 2004, pp. 557–559. Translated from Pis'ma v Zhurnal Tekhnicheskoĭ Fiziki, Vol. 30, No. 13, 2004, pp. 59–64.
Original Russian Text Copyright © 2004 by Shirotov, Divin.

Optimum Filtration of Broadband Radiation in Hilbert-Transform Spectroscopy

V. V. Shirotov* and Yu. Ya. Divin
Institute of Radio Engineering and Electronics, Russian Academy of Sciences, Moscow, Russia
**e-mail: votoriw@mail.ru*

Received January 22, 2004

Abstract—The possibility of optimum filtration of the radiation of a mercury arc lamp for subterahertz Hilbert-transform spectroscopy with a frequency-selective Josephson detector is demonstrated. Hilbert-transform spectroscopy was used for the first time for measuring the transmission spectrum of a high-pass filter. *© 2004 MAIK “Nauka/Interperiodica”.*

Hilbert-transform spectroscopy [1] is based on the frequency-selective detection of electromagnetic radiation using superconducting Josephson junctions. This spectroscopic technique works in a broad frequency range around the characteristic frequency $f_c = 2eI_cR_n/h$ of the Josephson oscillation, where I_c is the critical current and R_n is the normal state resistance of the junction. In the case of high-T_c Josephson junctions, the operational frequency range extends from several tens of gigahertz to several terahertz [2, 3]. The low-frequency limit f_l related to a finite width δf of the Josephson oscillation line is defined by the formula $f_1 = \delta f(f_l) = (3f_0 f_c^2/2)^{1/3}$, where $f_0 = 4\pi(2e/h)^2kTR_n$ is the Josephson oscillation line width at high voltages ($V \gg I_cR_n$) and T is the junction temperature [3]. The high-frequency limit f_h is related to a decrease in the Josephson oscillation amplitude as a result of the Joule heating [2] or the interaction with optical phonons [3]. Since the classical square-law detection and a bolometric mechanism are operative at frequencies below and above the operational range $[f_l, f_h]$, respectively, the Josephson junction may exhibit responses not containing spectral information and leading to distortions in the results of the Hilbert-transform spectroscopy measurements.

If the radiation spectrum is wider than the operational frequency range of Hilbert-transform spectroscopy, as is the case with mercury arc lamps [4] or transient radiation of relativistic electron beams [5], it is necessary to eliminate the low-frequency ($f < f_l$) and high-frequency ($f > f_h$) components. This study was aimed at determining the possibility of optimum filtration of a broadband radiation in Hilbert-transform spectroscopy.

The experiments were performed with a frequency-selective Josephson detector based on a thin-film bicrystal $YBa_2Cu_3O_{7-x}$ junction [6] situated in an optical cryostat with liquid nitrogen. By pumping nitrogen vapor, it was possible to provide for a working temperature in the interval from 77 down to 50 K.

The broadband radiation source was based on a 200-W low-pressure mercury arc lamp [7]. In the operational frequency range of Hilbert-transform spectroscopy, the spectrum of this source is close to the spectrum of blackbody with an effective temperature of about 4000 K (at higher frequencies, about 1000 K) [4]. The maximum of the spectral power density of the given source occurs in the region of several hundred terahertz; accordingly, radiation in the frequency interval corresponding to the operational frequency range of Hilbert-transform spectroscopy accounts for only about 10^{-3} of the total output radiation power of the lamp. In order to effectively eliminate intense high-frequency components, we used a system of reflection and transmission filters.

The mercury arc lamp was placed in the primary focus of a reflecting ellipsoid. The radiation of this source was first directed to a gold-coated echelette grating [4] oriented at $\alpha = 45°$ relative to the optical axis of the system. The echelette had a blaze angle of $\varphi = 20°$ and a period of $d = 50$ μm. For these parameters, incident radiation with wavelengths $\lambda > 2\lambda_b = 4d\cos\alpha\sin\varphi = 44$ μm exhibits predominantly zero-order diffraction [4]. This circumstance was used to provide for a preliminary cutoff of the high-frequency radiation components. Further attenuation of these components was provided by a fluoroplastic window at the optical input of the cryostat and by a crystal quartz filter situated at the cold screen of the cryostat.

A system of parabolic mirrors arranged between the source and the cryostat formed a radiation beam with a flat front, which was passed through a system of high-pass filters with various cutoff frequencies in the subterahertz range. We used specially designed filters comprising “thick” metal square cell mesh with a thickness equal to the period. The theory of such filters was developed by Chen [8, 9]. The filters are characterized by a

1063-7850/04/3007-0557$26.00 © 2004 MAIK “Nauka/Interperiodica”

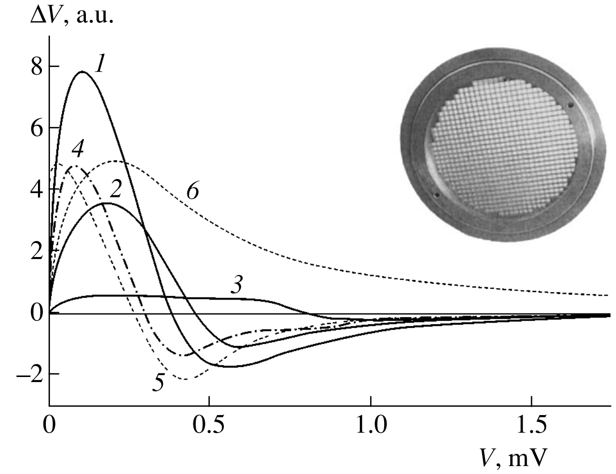

Fig. 1. Plots of the responses ΔV of a Josephson junction versus voltage V applied to the junction detecting broadband radiation of a mercury arc lamp filtered by various "thick" mesh filters: (*1*) without filters; (*2*) 1.0-mm-mesh filter; (*3*) 0.5-mm-mesh filter; (*4*) difference between curves *1* and *2*; (*5*) calculated response corresponding to the classical square-law detection; (*6*) calculated bolometric response. The inset shows the general view of a square cell mesh filter.

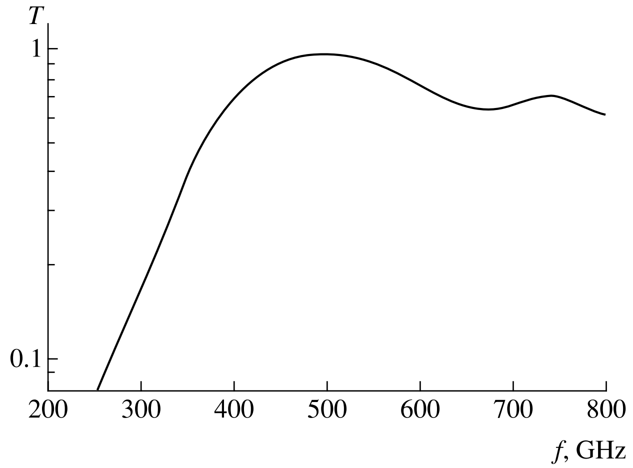

Fig. 2. Transmission spectrum of a "thick" 0.5-mm-mesh filter measured in Hilbert-transform spectroscopy.

low transmission at low frequencies. In the region of the cutoff frequency $f_{\text{cut}} = c/2b$ (where c is the velocity of light and b is the square open mesh cell size), the transmission exponentially increases up to a value on the order of unity and remains close to unity in a certain region above this frequency. Then, in the region of $f_{\text{opt}} = c/a$ (where a is the mesh period), the transmission reaches the level of optical transmission determined by the ratio of open and total mesh areas: $T_{\text{opt}} = b^2/a^2$. For the 1.0- and 0.5-mm-mesh filters, the cutoff frequencies were f_{cut} = 170 and 350 GHz, the optical transmission was 0.77 and 0.64, and the optical transmission frequencies were f_{opt} = 300 and 600 GHz, respectively. The general view of such a filter is presented in the inset in Fig. 1.

Figure 1 (curves *1*–*3*) shows the responses of one of the Josephson junctions ($R_n = 2.5\ \Omega$, $I_cR_n = 1$ mV, $T = 50$ K) to broadband radiation upon various degrees of filtration by thick mesh filters. For comparison, Fig. 1 also shows the plots of response versus voltage applied to the junction for the classical square-law detection (curve *5*) and bolometric mechanism (curve *6*). According to our estimations, the classical response is proportional to the second derivative of the current–voltage characteristic $V(I)$ of the junction: $\Delta V \propto d^2V/dI^2$. The bolometric response (taking into account only the heat-induced decrease in the critical current of the junction) obeys the relation $\Delta V \propto (1/I)dV/dI$.

Evidently, all the responses $\Delta V(V)$ measured for a practically constant level of attenuation of the high-frequency components exhibit sign reversal, in contrast to the behavior of the bolometric response (Fig. 1, curve *6*). This fact indicates the absence of the bolometric response and shows that a system comprising the echelette grating, the fluoroplastic window, and the crystal quartz filter completely eliminated the contribution of high-frequency radiation components. Moreover, the behavior of curves *1*–*3* also significantly differs from that of curve *5* corresponding to the classical square-law detection. From this we may conclude that the observed responses contain a significant contribution due to the frequency-selective Josephson detection mechanism.

For the particular Josephson junction studied, the characteristic frequencies were $f_c \approx 500$ GHz and $f_1 \approx 140$ GHz. Therefore, the cutoff frequency of the first filter is close to the lower limit of the operational frequency range of Hilbert-transform spectroscopy, while the characteristic frequencies of the second filter are in this range.

Figure 1 shows how the response shape changes upon modification of the broadband radiation spectrum as a result of variation in the lower cutoff frequency. The shift of the point of the response sign reversal indicates that the corresponding filter modifies the spectral composition of radiation and shows the possibility of frequency-selective detection using the Josephson detector. The shape of the differential signal (Fig. 1, curve *4*) is most close to the curve representing the classical square-law response. This fact confirms strong attenuation of the low-frequency part of the radiation spectrum (not entering into the operational frequency range of Hilbert-transform spectroscopy) by the first filter. The small difference between the shapes of the differential signal and the classical square-law response can be explained by the fact that the first filter partly attenuates the radiation components falling within the operational frequency range of the given frequency-selective Josephson detector.

Figure 2 shows a transmission spectrum of the second (0.5-mm-mesh) filter determined in Hilbert-transform spectroscopy. In order to construct this curve, the measured responses were used to restore the radiation spectra without and with this filter, after which the second spectrum was normalized to the first one. As can be seen from Fig. 2, the thick mesh filter provides for the exponential attenuation of components below the cutoff frequency of 370 GHz and has a high-frequency transmission close to anticipated.

The transmission spectrum of the thick mesh measured in Hilbert-transform spectroscopy qualitatively agrees with the characteristics of such filters determined using terahertz time-domain spectroscopy employing pulsed broadband radiation sources of greater output power [10].

Thus, we have studied the conditions of optimum filtrations of broadband radiation for Hilbert-transform spectroscopy by measuring the transmission spectra of high-pass filters with various cutoff frequencies in the subterahertz range. It was demonstrated that the transmission spectrum of the filter determined in Hilbert-transform spectroscopy agrees with the published data for the values of cutoff frequencies above the width of the Josephson oscillation line.

Acknowledgments. This study was supported in part by the International Scientific-Technological Center (project no. 1912), the Basic Research Program of the Department of Physical Sciences of the Russian Academy of Sciences, and the Forschungszentrum Julich (Germany).

REFERENCES

1. Yu. Ya. Divin, O. Yu. Polyanskiĭ, and A. Ya. Shul’man, Pis’ma Zh. Tekh. Fiz. **6**, 1056 (1980) [Sov. Tech. Phys. Lett. **6**, 454 (1980)].
2. Y. Divin, O. Volkov, V. Shirotov, *et al.*, Adv. Solid State Phys. **42**, 301 (2001).
3. Y. Divin, O. Volkov, M. V. Liatti, *et al.*, IEEE Trans. Appl. Supercond. **13**, 676 (2003).
4. *Methods of Spectroscopy in Far Infrared, Submillimeter, and Millimeter Spectrum Ranges*, Ed. by T. M. Lifshits (Moscow, 1970).
5. U. Happek, A. J. Sievers, and E. B. Blum, Phys. Rev. Lett. **67**, 2962 (1991).
6. Yu. Ya. Divin, I. M. Kotelyanskiĭ, and V. N. Gubankov, Radiotekh. Élektron. (Moscow) **48**, 1238 (2003).
7. Model no. 6283, LOT-Oriel production.
8. C. C. Chen, IEEE Trans. Microwave Theory Tech. **18**, 627 (1970).
9. C. C. Chen, IEEE Trans. Microwave Theory Tech. **21**, 1 (1973).
10. C. Winnewisser, F. Lewen, and H. Helm, Appl. Phys. A **66**, 593 (1998).

Translated by P. Pozdeev

Technical Physics Letters, Vol. 30, No. 7, 2004, pp. 560–562. Translated from Pis'ma v Zhurnal Tekhnicheskoĭ Fiziki, Vol. 30, No. 13, 2004, pp. 65–70.
Original Russian Text Copyright © 2004 by Dedkov, Kyasov.

Fluctuational-Electromagnetic Interaction between a Neutral Particle and a Flat Surface in the Case of Perpendicular Motion

G. V. Dedkov* and A. A. Kyasov
Kabardino-Balkarian State University, Nal'chik, Kabardino-Balkaria, Russia
**e-mail: gv.dedkov@mail.ru*

Received December 16, 2003

Abstract—Formulas for the rate of heating and the conservative and dissipative forces of interaction between a neutral spherical particle and the surface of a homogeneous semi-infinite polarizable medium are obtained for the first time in a nonrelativistic approximation of the fluctuational electromagnetic field theory for a particle moving in vacuum perpendicularly to the vacuum–medium interface. For equal temperatures of the particle and the medium surface, the coefficient of viscous friction in this system is two times that for the same particle moving parallel to the interface. The same ratio is observed for the dynamic contributions to the conservative force of attraction to the surface and the quadratic (with respect to the particle velocity) corrections to the heating rate. It is shown for the first time that, in contrast to the parallel motion, the heating rate also includes a linear contribution, which is dominating in the case of equal temperatures of the particle and the medium surface. *© 2004 MAIK "Nauka/Interperiodica".*

In recent papers devoted to the theory of fluctuational electromagnetic forces [1–3], we addressed the case of a particle moving in vacuum parallel to the boundary of a polarizable medium. In particular, we obtained the most general expressions for the tangential (nonconservative) force of interaction between the particle and medium and the rate of particle heating for arbitrary initial temperatures of the particle and the medium.

Although the corresponding results for a particle moving perpendicularly to the interface are qualitatively quite evident, no such data were available until now because of considerable mathematical difficulties. In particular, it was known that the coefficients of viscous friction for the perpendicular motion of charged particles and dipole molecules are two to four times greater than those for the parallel motion [1, 4, 5]. On the other hand, according to calculations of the tangential dissipative forces at a zero temperature [5, 6], the friction coefficients for physically adsorbed atoms performing decaying oscillations may differ by a factor of 5 [5] or 6.3 [6]. Thus, the question concerning the exact relation between the friction coefficients in the cases of parallel and perpendicular motion remained open.

The purpose of this study was to develop our nonrelativistic theory [1–3] so as to include the case of a normal motion of particles relative to the vacuum–medium interface. These results are principally necessary for interpretation of the results of atomic force microscopy obtained in the modulated interaction regime, whereby the probe oscillates perpendicularly to the sample surface. Using such a theory and the previous results [2, 3], it would be possible to obtain analogous formulas for a particle moving at an arbitrary angle to the interface.

According to [2, 3], the force of interaction between a moving neutral particle and the surface of a semi-infinite medium is given by the expression

$$\mathbf{F} = \langle(\mathbf{d}^{sp}\nabla)\mathbf{E}^{in}\rangle + \langle(\mathbf{d}^{in}\nabla)\mathbf{E}^{sp}\rangle, \tag{1}$$

where $\mathbf{d}^{sp}$, $\mathbf{d}^{in}$ and $\mathbf{E}^{sp}$, $\mathbf{E}^{in}$ are the spontaneous and induced components of the particle dipole moment and the electric field at the surface, respectively, and angle brackets denote complete quantum-statistical averaging. Projecting Eq. (1) onto the direction of particle motion and assuming for certainty that the particle velocity vector $\mathbf{V}$ is directed toward the surface, we obtain

$$\mathbf{F} = \langle(\mathbf{d}^{sp}\nabla)\mathbf{E}_z^{in}\rangle + \langle(\mathbf{d}^{in}\nabla)\mathbf{E}_z^{sp}\rangle. \tag{2}$$

By the same token, the rate of heating (cooling of the particle) can be expressed as [2, 3]

$$\dot{Q} = \langle\dot{\mathbf{d}}\mathbf{E}\rangle = \langle\dot{\mathbf{d}}^{sp}\mathbf{E}^{in}\rangle + \langle\dot{\mathbf{d}}^{in}\mathbf{E}^{sp}\rangle. \tag{3}$$

Following the method developed in [1–3], calculations are performed upon replacing the quantities in Eqs. (2) and (3) by the corresponding integral Fourier expansions with respect to spatial variables *x*, *y* (in the interface plane) and the time *t*; the field components

$\mathbf{E}^{in}_{\omega\mathbf{k}}(z)$ and $\mathbf{E}^{sp}_{\omega\mathbf{k}}(z)$ are taken at the point $(z_0 - Vt)$ where the particle occurs at the current time moment (z_0 is the particle–surface distance at $t = 0$). Then, the vector $\mathbf{E}^{sp}_{\omega\mathbf{k}}(z)$ is expressed via the electric potential determined from a solution of the Poisson equation $\nabla^2\phi = 4\pi\mathrm{div}\mathbf{P}$. The Fourier components of the polarization vector $\mathbf{P}(x, y, z, t)$ induced by the particle are expressed as the Taylor series in powers of the velocity, in which the first three terms are retained:

$$\begin{aligned}\mathbf{P}_{\omega\mathbf{k}}(z) \; = \; & \mathbf{d}^{sp}(\omega)\delta(z - z_0) - iV \cdot \dot{\mathbf{d}}^{sp}(\omega)\delta'(z - z_0) \\ & -\frac{V^2}{2}\ddot{\mathbf{d}}^{sp}(\omega)\delta''(z - z_0).\end{aligned} \tag{4}$$

Note that expansion (4) implies that $Vt \ll z_0$. An analogous expression is obtained for the field vector $\mathbf{E}^{sp}_{\omega\mathbf{k}}(z_0 - Vt)$ used to calculate the induced dipole moment $\mathbf{d}^{in}(t)$ of the particle via the well-known integral relation

$$\begin{aligned}\mathbf{d}^{in}(t) = \int_0^\infty \alpha(\tau)\mathbf{E}^{sp}(t - \tau)d\tau \; = \; (2\pi)^{-3}\iiint d^2k d\omega \alpha(\omega) \\ \times\left(\mathbf{E}^{sp}_{\omega\mathbf{k}}(z_0) - ikV\dot{\mathbf{E}}^{sp}_{\omega\mathbf{k}}(z_0) - \frac{(kV)^2}{2}\ddot{\mathbf{E}}^{sp}_{\omega\mathbf{k}}(z_0)\right)\exp(-i\omega t),\end{aligned} \tag{5}$$

where dots above the Fourier amplitudes denote differentiation with respect to time.

A solution to the Poisson equation with allowance for relation (4) and the corresponding boundary conditions was obtained previously (see, e.g., [7]). Correlators between the Fourier transforms of the dipole moment and the electric field in Eqs. (2) and (3) are calculated as described in [1–3]. Additional terms with the coefficients Vt arising in these calculations are eliminated by the limiting transition $t \longrightarrow 0$. The proposed approach is justified (besides the adopted approximation $Vt \ll z_0$) by the fact that the same limiting transition has to be performed in obtaining an approximate solution of the problem concerning the parallel motion of a particle (with analogous expansions of the polarization and electric field vectors) in order to obtain results coinciding with the exact solution [1–3].

Finally, an expression for the force of interaction between the particle and the surface appears as

$$\begin{aligned}F_z \; = \; & -\frac{3\hbar}{4\pi z_0^4}\int_0^\infty\left(\alpha''(\omega)\Delta'(\omega)\coth\left(\frac{\omega\hbar}{k_BT_1}\right)\right. \\ & \left.+\alpha'(\omega)\Delta''(\omega)\coth\left(\frac{\omega\hbar}{k_BT_2}\right)\right)d\omega \\ & +\frac{3\hbar V}{2\pi z_0^5}\int_0^\infty\left(\alpha''(\omega)\frac{d\Delta''(\omega)}{d\omega}\coth\left(\frac{\omega\hbar}{k_BT_1}\right)\right. \\ & \left.+\Delta''(\omega)\frac{d\alpha''(\omega)}{d\omega}\coth\left(\frac{\omega\hbar}{k_BT_2}\right)\right)d\omega \\ & -\frac{15\hbar V^2}{8\pi z_0^6}\int_0^\infty\left(\alpha''(\omega)\frac{d^2\Delta'(\omega)}{d\omega^2}\coth\left(\frac{\omega\hbar}{k_BT_1}\right)\right. \\ & \left.+\Delta''(\omega)\frac{d^2\alpha'(\omega)}{d\omega^2}\coth\left(\frac{\omega\hbar}{k_BT_2}\right)\right)d\omega,\end{aligned} \tag{6}$$

where T_1 and T_2 are the temperatures of the particle and the surface, respectively; $\Delta(\omega) = \frac{\varepsilon(\omega) - 1}{\varepsilon(\omega) + 1}$ is the dielectric response function; $\varepsilon(\omega)$ is the permittivity of the medium; $\alpha(\omega)$ is the dynamic polarizability of the particle; and primed and double-primed quantities denote the real and imaginary components. The first and third terms in formula (6) are related to the conservative force of the particle–surface interaction taking into account the static van der Waals attraction and the first dynamic correction, while the second term describes the viscous dissipative force. The next term in the expansion for the dissipative force, which is proportional to V^3/z_0^7, is omitted. The small parameter in this expansion is $V/z_0\omega_0$, where ω_0 is the characteristic absorption frequency in the electromagnetic spectrum.

For a nonlocal dielectric permittivity function $\varepsilon(\mathbf{k}, \omega)$, formula (6) can be generalized using the same approach as that described for the case of parallel motion [3, 8]. For example, the dissipative component of the force is expressed as

$$\begin{aligned}F_z \; = \; & \frac{\hbar V}{\pi^2}\int q^3\exp(-2qz_0)d^2q\int_0^\infty\left(\alpha''(\omega)\frac{d\Delta''(q, \omega)}{d\omega}\right. \\ & \left.\times\coth\left(\frac{\omega\hbar}{k_BT_1}\right) + \Delta''(q, \omega)\frac{d\alpha''(\omega)}{d\omega}\coth\left(\frac{\omega\hbar}{k_BT_2}\right)\right)d\omega,\end{aligned} \tag{7}$$

where q is the two-dimensional projection of the wave vector $\mathbf{k}$ onto the (x, y) plane and

$$\Delta(q, \omega) \; = \; \frac{\pi - qI}{\pi + qI}, \quad I \; = \; \int_{-\infty}^{+\infty}\frac{dk_z}{(q^2 + k_z^2)\varepsilon(\mathbf{k}, \omega)}. \tag{8}$$

By analogy with the above calculation of the fluctuational force, we obtain the following expression for rate of heating determined by formula (3):

$$\dot{Q} = -\frac{\hbar}{\pi z_0^3}\int_0^\infty d\omega\omega\alpha''(\omega)\Delta''(\omega)$$

$$\times\left[\frac{1}{\exp(\hbar\omega/k_BT_1)-1}-\frac{1}{\exp(\hbar\omega/k_BT_2)-1}\right]$$

$$-\frac{3\hbar V}{4\pi z_0^4}\int_0^\infty d\omega\omega\alpha''(\omega)\frac{d\Delta'(\omega)}{d\omega}\coth\left(\frac{\omega\hbar}{k_BT_1}\right)$$

$$-\frac{3\hbar V}{4\pi z_0^4}\int_0^\infty d\omega\Delta''(\omega)\frac{d}{d\omega}(\omega\alpha'(\omega))\coth\left(\frac{\omega\hbar}{2k_BT_2}\right) \qquad (9)$$

$$-\frac{3\hbar V^2}{4\pi z_0^5}\int_0^\infty d\omega\left\{\coth\left(\frac{\omega\hbar}{2k_BT_1}\right)\omega\alpha''(\omega)\frac{d^2\Delta''}{d\omega^2}\right.$$

$$\left.-\coth\left(\frac{\omega\hbar}{2k_BT_2}\right)\Delta''(\omega)\frac{d^2(\omega\alpha''(\omega))}{d\omega^2}\right\}.$$

A comparison of the numerically calculated coefficients at the terms proportional to the squared velocity in formulas (6) and (9) with the corresponding data for the case of parallel motion [2, 3] shows that the former values are twice as large as the latter ones. A substantially new result is the presence of linear (with respect to the velocity) second and third terms in Eq. (9). As can be readily seen for equal temperatures of the particle and the interface (when the static contribution to the heating rate given by the first term in Eq. (9) is zero), the dominating contribution to $\dot{Q}$ is due to these linear terms.

If the functions determining the dielectric properties of the particle and medium are continuously differentiable, the expansions in powers of the parameter $V/z_0\omega_0$ can be continued. This provides for the principal possibility of restoring the most general form of the frequency functionals for the interaction force and the heating rate.

REFERENCES

1. G. V. Dedkov and A. A. Kyasov, Phys. Lett. A **259**, 38 (1999); Fiz. Tverd. Tela (St. Petersburg) **43**, 169 (2001) [Phys. Solid State **43**, 176 (2001)].
2. G. V. Dedkov and A. A. Kyasov, Fiz. Tverd. Tela (St. Petersburg) **44**, 1729 (2002) [Phys. Solid State **44**, 1809 (2002)].
3. G. V. Dedkov and A. A. Kyasov, Phys. Low-Dimens. Struct. **1–2**, 1 (2003).
4. M. S. Tomassone and A. Widom, Phys. Rev. B **56**, 4938 (1997).
5. A. Liebsch, Phys. Rev. B **55**, 13263 (1997).
6. B. N. J. Persson and A. I. Volokitin, J. Chem. Phys. **103**, 8679 (1995).
7. A. A. Kyasov and G. V. Dedkov, Fiz. Tverd. Tela (St. Petersburg) **44**, 1700 (2002) [Phys. Solid State **44**, 1779 (2002)].
8. G. V. Dedkov and A. A. Kyasov, Pis'ma Zh. Tekh. Fiz. **27** (8), 68 (2001) [Tech. Phys. Lett. **27**, 338 (2001)].

Translated by P. Pozdeev

Technical Physics Letters, Vol. 30, No. 7, 2004, pp. 563–565. Translated from Pis'ma v Zhurnal Tekhnicheskoĭ Fiziki, Vol. 30, No. 13, 2004, pp. 71–76.
Original Russian Text Copyright © 2004 by Aleksandrov, Mikheev.

Effect of Transverse Oscillations on the Vibrational Transport of a Piezoelement along a String

V. A. Aleksandrov and G. M. Mikheev*
Institute of Applied Mechanics, Ural Division, Russian Academy of Sciences, Izhevsk, Udmurtia, Russia
**e-mail: gmmikheev@udmnet.ru*

Received December 22, 2003

Abstract—We have studied conditions admitting the vibrational transport of a piezoelement along a string by means of low-frequency excitation of this piezoelement. Transportation of the piezoelement takes place only in certain regions of the string. The positions of these transport regions correspond to the nodes of standing transverse waves in the string and are determined by the frequencies of excitation and the natural transverse oscillations of the string. The position of the piezoelement on the string can be controlled by smoothly varying the frequency of the applied voltage. *© 2004 MAIK “Nauka/Interperiodica”.*

Introduction. Vibrational wave transportation is used for the transfer of objects over a surface of an elastic resonator excited by impact or by a kinematic action [1]. It is also known that the wave motion can be used for spraying liquids [2] and transferring microscopic particles over the surface of a plate [3]. The vibrational transport of particles is provided by waves excited in the carrying surface by an independent external source.

Previously [4], the effect of transportation was reported for a piezoelement hanging on a string. This effect indicated the possibility of vibrational transportation of a source of oscillations at a velocity significantly exceeding that of the particles occurring far from the source of oscillations on the same surface. It was suggested that this phenomenon is related to the high-frequency repulsion of the piezoelement from the crest of an elastic wave excited in the string. In this context, it was of interest to study the effect of string oscillations propagating in the form of elastic waves on the vibrational motion of a hanging piezoelement.

Experimental arrangement. The experiments were performed using a device with a nichrome string (20Kh80N alloy, density $\rho = 7.72 \times 10^3$ kg/m^3) with a diameter of 0.62 mm (Fig. 1a). The horizontal part of string *1* was stretched between ribs *2* of base *3*. The distance between ribs determined the resonator length (0.6 m). The device was equipped with dynamometer *4* measuring load with an accuracy of ±2% and allowed the string tension to be smoothly varied by control *5*. The source of oscillations was piezoelement *6* comprising two ZP-4 plates (jointed by soldering in order to increase the amplitude of oscillations) with a total mass of 6×10^{-3} kg. The piezoelement was freely hanging on a 45-mm-long bracket *7* made of the string material (nichrome). The piezoelement was excited by a sinusoidal control voltage with an amplitude of 25 V supplied via flexible leads from am audio-frequency oscillator with an amplifier. The frequency of the driving voltage was monitored by a digital frequency meter and the amplitude was measured by a two-channel oscillograph *11*. The piezoelement was excited in the range of low frequencies from 0.1 to 2 kHz; the string tension was F = 50, 75, 80, 90, or 100 N.

Oscillations of the string were monitored in various regions using the optical (shadow) technique (Fig. 1b). For this purpose, a beam of laser *8* was focused by lens *9* on the string surface perpendicularly to the plane of oscillations. Oscillating string modulated the light flux incident onto the surface of photodiode *10* situated

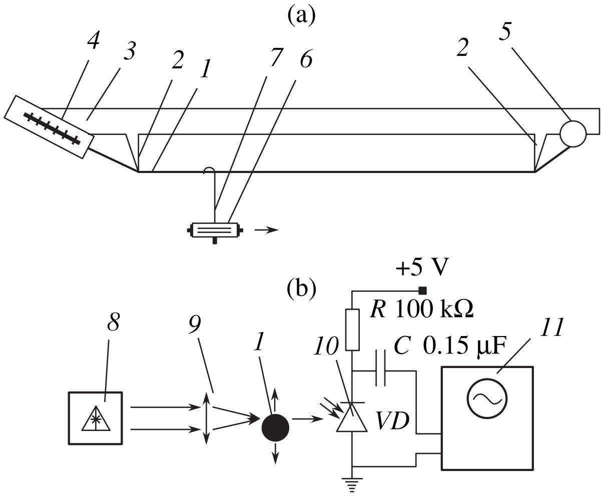

Fig. 1. Schematic diagram of the (a) mechanical and (b) optical experimental arrangement: (*1*) string; (*2*) ribs; (*3*) base; (*4*) dynamometer; (*5*) string tension control; (*6*) piezoelement; (*7*) bracket; (*8*) semiconductor laser; (*9*) focusing lens; (*10*) photodiode; (*11*) oscillograph.

1063-7850/04/3007-0563$26.00 © 2004 MAIK “Nauka/Interperiodica”

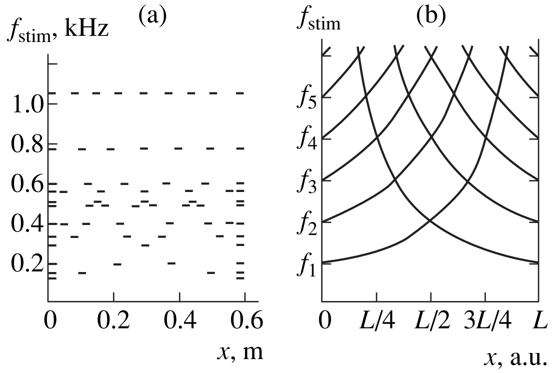

Fig. 2. (a) Experimental diagrams of the positions x of regions admitting the vibrational motion of a piezoelement along a string (L = 0.6 m, F = 50 N) for various excitation frequencies f_{stim}; (b) plots of the $f_{\text{stim}}(x)$ for the vibrational motion of the source of oscillations along the string calculated using relations (3) and (4); f_1–f_5 are the frequencies of natural oscillations of the string.

behind the string. The output signal of this photodiode was fed to the second channel of oscillograph *11* to be compared to the oscillations of piezoelement *6*. Using this scheme, the amplitude of transverse oscillations of the string could be measured with a sensitivity of 1 μm. In the course of experiments, the maximum amplitude of transverse oscillations of the string reached 0.5 mm.

Calculations were performed assuming that the transverse oscillations in the string propagate in the form of elastic waves with the velocity ν_η dependent on the string tension F, material density ρ, and cross section area S: $\nu_\eta = (F/\rho S)^{1/2}$.

Results and discussion. It was found that the piezoelement excited in the indicated low-frequency range performs slow vibrational motion with the bracket along the string at a velocity of 1–2 mm/s. This motion takes place only in certain regions of the string with a length not exceeding 20 mm. For a fixed excitation frequency, there are several regions of such vibrational motion centered at points arranged along the string symmetrically relative to its center (Fig. 2a). As the excitation frequency is varied, these regions shift along the string, but the motion near the string ends (at the ribs) is observed for all excitation frequencies. Thus, by smoothly varying the oscillation frequency of the piezoelement, it is possible to control its position on the string.

It was experimentally demonstrated that, under the conditions of vibrational motion of the source of oscillations (piezoelement), the maximum amplitude of transverse oscillations of the string is observed in the regions between the point of hanging and the ends. Various parts of the string may oscillate at two different frequencies, f_{stim} and nf_{stim}, where f_{stim} is the stimulating source (piezoelement) frequency and n = 2, 3, 4, ….

The observed results can be explained by impact interaction between the source of oscillations and the string. Both transverse and longitudinal elastic waves are simultaneously excited at a point where the bracket touches the string. The amplitude of these waves can be large when the source oscillates relative to an immobile part of the string or when the oscillations at the hanging point are absent. Since the string ends are fixed, transverse oscillations at the ends are impossible. Oscillations of the source relative to the string in these regions are always sufficient to excite elastic waves as a result of impact action upon the string surface. At certain frequencies of this action, the elastic waves propagating along the string induce resonance transverse oscillations in the form of standing waves.

The wavelength λ_{st} of a standing transverse wave equals the distance between nodes, which amounts to half of the length of a usual transverse wave. In the case of natural oscillations, an integer number of standing waves are accommodated on the string. The corresponding wavelengths can be expressed through the parameters of the string and the natural frequency f_{own}:

$$\lambda_{\text{st}} = (F/\rho S)^{1/2}/2f_{\text{own}}. \tag{1}$$

The frequencies of natural oscillations of a string with the length L form the harmonic sequence $f_{N\text{own}} = Nf_{1\text{own}}$ (where N = 1, 2, 3, …) and

$$f_{1\text{own}} = (F/\rho S)^{1/2}/2L. \tag{2}$$

Excitation of the standing transverse waves in the string is also possible when the source of oscillation occurs in the other region at a certain distance x from one of the string ends. In this case, the excitation frequency f_{stim} and the position x are determined by a family of curves (Fig. 2b) obeying the equations

$$f_{\text{stim}} = N\nu_\eta/2x, \quad 0 < x \le L; \tag{3}$$

$$f_{\text{stim}} = N\nu_\eta/2(L-x), \quad 0 \le x < L. \tag{4}$$

As can be seen from Fig. 2b, the points of intersection of these curves correspond to the excitation frequencies equal to the frequencies of natural oscillations of the string ($f_{\text{stim}} = f_{\text{own}}$). At the same time, these points coincide with the nodes of standing transverse waves formed during the natural oscillations of the string. In this case, all regions of the string oscillate with the same frequency and an integer number of the wavelengths of standing waves are accommodated on the string length.

If $f_{\text{stim}} \neq f_{\text{own}}$, that is, when the point (x, f_{stim}) in Fig. 2b does not coincide with the intersection of curves *3* and *4* (but belongs to one of these curves), experiments show that various parts of the string may oscillate with different frequencies: f_{stim} and nf_{stim} (n = 1, 2, 3, …). As a result, standing waves of different lengths, $\lambda_{\text{stim}} = \nu_\eta/2f_{\text{stim}}$ and $\lambda_{1\text{stim}} = \nu_\eta/2nf_{\text{stim}}$, are excited in various parts of the string. These wavelengths obey the relation

$$l\lambda_{\text{stim}} + m\lambda_{1\text{stim}} \approx L, \tag{5}$$

where l and m are integers.

The results of analysis and calculations performed for all values of the string tension used in our experiments showed that the observed coordinates of the centers of regions featuring the vibrational motion of the piezoelement along the string coincide to within 0.5% with the curves constructed using Eqs. (3) and (4). From this we infer that the vibrational motion of the source of oscillations takes place in the regions where the transverse oscillations are absent. These regions are observed at the string ends and at the nodes of standing transverse waves excited by this source in the string. When the source is outside these regions, oscillations of the string may cause damping of the impact. As a result, the amplitude of oscillations of the source relative to the string drops and the vibrational motion of the source along the string ceases. This behavior indicates that the mechanism of the vibrational motion of an oscillation source operative in the course of transportation along the string is different from the mechanism involved in the wave transport of particles occurring far from the wave source [1, 2].

Conclusions. Transverse oscillations of the string excited in the course of vibrational transportation produce damping of the source oscillations. As a result, the vibrational motion is observed only at the string ends and at the nodes of standing transverse waves excited by this source in the string, that is, at the points where the transverse oscillations are absent. This result suggests that the mechanism of the vibrational transportation of an oscillation source along the string, in contrast to the mechanism involved in the wave transport of particles occurring far from the wave source, is not related to transverse oscillations of the string. However, the excitation of transverse oscillations provides conditions when a piezoelement can be transported along the string by smoothly varying the frequency of the sinusoidal driving signal.

REFERENCES

1. *Vibrations in Engineering: A Handbook,* Ed. by E. E. Lavendel (Mashinostroenie, Moscow, 1981), Vol. 4.
2. V. A. Aleksandrov, Pis'ma Zh. Tekh. Fiz. **28** (10), 88 (2003) [Tech. Phys. Lett. **28**, 438 (2003)].
3. A. N. Gorb and O. A. Korotchenkov, Pis'ma Zh. Tekh. Fiz. **28** (17), 67 (2002) [Tech. Phys. Lett. **28**, 740 (2002)].
4. V. A. Aleksandrov, Datchiki i Sistemy, No. 6, 35 (2001).

Translated by P. Pozdeev

Technical Physics Letters, Vol. 30, No. 7, 2004, pp. 566–568. Translated from Pis'ma v Zhurnal Tekhnicheskoĭ Fiziki, Vol. 30, No. 13, 2004, pp. 77–82.
Original Russian Text Copyright © 2004 by Ionov, Popov, Svetlichnyĭ, Pashkevich.

Field Electron Emission from Flat Metal Cathodes Covered by Thin Polymer Films

A. N. Ionov*, E. O. Popov, V. M. Svetlichnyĭ, and A. A. Pashkevich
Ioffe Physicotechnical Institute, Russian Academy of Sciences, St. Petersburg, 194021 Russia
Institute of Macromolecular Compounds, Russian Academy of Sciences, St. Petersburg, 199004 Russia
**e-mail: ionov@tuch.ioffe.rssi.ru*

Received November 14, 2003

Abstract—We have studied the physical properties of a new class of field electron emitters representing metal cathodes covered by thin polymer films based on a soluble imide–siloxane copolymer. Polymer coating leads to an increase in the emission current and provides for a quite stable field electron emission of flat polished molybdenum and niobium cathodes. *© 2004 MAIK “Nauka/Interperiodica”.*

In recent years, much effort has been devoted to the search for promising materials for field emission cathodes capable of stably operating under the conditions of a relatively low vacuum (i.e., at a residual pressure of 10^{-6} Torr and above). Numerous variants of field emission cathodes based on carbon-containing materials have been described in research papers and patents. The list of promising materials includes, in particular, (i) carbon fibers [1, 2], (ii) massive carbon plates processed by radiation technologies ensuring the formation of a well-developed surface in initially smooth cathodes [3], and (iii) nanodimensional carbon structures such as nanotubes [4]. It was also reported that the field electron emission from silicon and molybdenum point cathodes increases upon coating with diamond-like films by methods of chemical vapor deposition or electrophoresis [5].

This Letter presents the results of investigation of the physical properties of a new class of field electron emitters—metal cathodes coated by thin (1–2-μm-thick) polymer films based on a soluble imide–siloxane block copolymer. Previously [6], we reported on an anomalously high channel conductivity of this copolymer placed between metal electrodes. Imide–siloxane copolymer synthesized as described in [7] possesses a structure composed of polyester imide blocks and siloxane imide blocks [8]. The former blocks represent alternating dianhydride and aromatic diamine residues, and the latter blocks represent alternating dianhydride and siloxane diamine residues. This copolymer was selected because it exhibits no viscous flow at room temperature (in contrast to poly(dimethylsiloxane)) due to the aromatic imide fragments and is capable of forming strong coatings on metals. By varying the ratio of flexible oligo(dimethylsiloxane) and more rigid aromatic imide fragments, it is possible to control the supramolecular structure of these polymer films. The modulus of elasticity and the strength at break of a 40-μm-thick film amount to 40 ± 1 and 6.5 ± 0.3 MPa, respectively, while the temperature of the onset of thermal decomposition of the imide–siloxane copolymer exceeds 400°C. The polymer films are characterized by good adhesion to metals.

Thin polymer coatings with a thickness of about 1 μm were applied onto polished edge surfaces of molybdenum and niobium cathodes with a diameter of 5 mm by the method of solution spreading. For this purpose, the calculated amount of a 5% copolymer solution in anhydrous N-methyl-2-pyrrolidone was placed onto the cathode surface, after which the solvent was removed by heating the electrode in a thermal box for 1–2 h at 100°C in air at atmospheric pressure. The polymer film thickness was determined with the aid of an MII-4 interference microscope (LOMO Company, Russia).

The surface topography of polymer coatings was studied by the method of atomic force microscopy (AFM) in air. The measurements were performed in a resonance regime on a Solver P47 instrument (NTMDT, Russia) using NSG11 silicon probes (NTMDT, Russia) with a curvature radius of the probe tip below 40 nm. The AFM topograms of the polymer surface measured prior to field electron emission measurements showed that the surface roughness did not exceed 30 nm, which allows the surface to be considered as sufficiently smooth.

The field electron emission from polymer-coated cathodes was studied in a vacuum of 10^{-6} Torr. The distance from the flat cathode to a grid anode was 0.5–1.5 mm. The grid anode was made of the shadow mask of a TV tube. The cathode images formed on a flat luminescent screen were monitored with the aid of a TV camera, digitized, and stored in a computer mem-

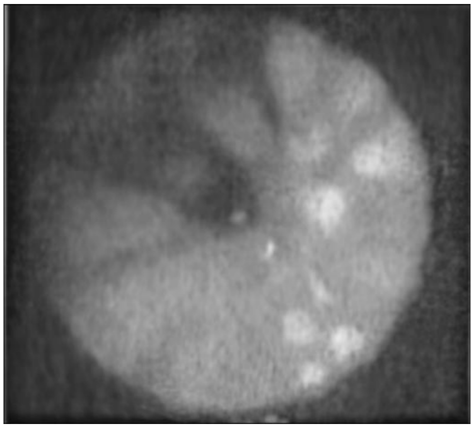

Fig. 1. Luminescent image of operating polymer-coated field emitter (cathode diameter, 5 mm).

ory. The screen occurred at a grid potential and was positioned at a small distance from the grid so as to provide for a fourfold magnification.

The current–voltage characteristics of the cathodes were measured in both forward and reverse directions by high-voltage scanning at a frequency of 50 Hz. The values of current and voltage were measured with a two-channel digital oscillograph and stored in a computer memory. The experimental setup was linked to computer via a standard slot with a laboratory-made interface plate of special design providing 16 bit/channel data acquisition at a sampling frequency of 100 ks/s.

The lower threshold electric field strength for which the field emission current was detected from a cathode coated with the imide–siloxane copolymer was 4 kV/mm. However, the primary activation of the electron emitter required applying a field 2.5–3 times higher than this lower threshold. It should be noted that the field emission from bare (uncoated) polished metal electrodes did not take place below 25 kV/mm.

Figure 1 shows the typical luminescent image formed on a screen by electrons emitted from a polymer-coated flat niobium cathode at an electric field strength of 6 kV/mm. As can be seen, the electron emission centers are distributed over the entire cathode surface.

The AFM topography of a polymer film after the field emission measurements showed that the initial surface was strongly modified: there appeared cusps with a height of up to 400 nm (Fig. 2a). The formation of cusps on the polymer surface in a strong electric field can be explained by local electrification due to self-injection of charge carriers from the metal electrode into a relatively elastic polymer matrix [9].

The reversible current–voltage characteristics (Fig. 2b) measured at relatively low bias voltages agrees with the Fowler–Nordheim theory, which is evidence of the field emission regime of operation of a polymer-coated cathode. However, further increase in the applied voltage (above ~6000 V) is accompanied by a slower growth in the current.

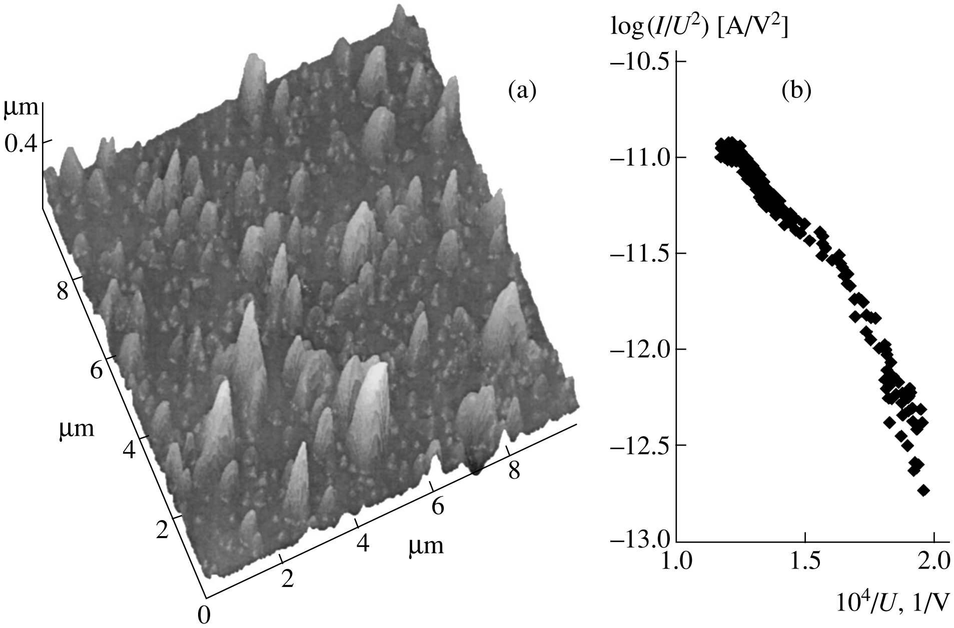

Fig. 2. Polymer coated field emitter: (a) an AFM image of a modified polymer surface showing cusps with a height of up to 400 nm; (b) a current–voltage characteristic of the imide–siloxane copolymer on a niobium substrate plotted in the Fowler–Nordheim coordinates.

X-ray analysis of a polymer film after the emitter operation for several hours at a field strength of $E >$ 10 kV/mm in the interelectrode gap and an emission current of $I > 1$ mA showed the presence of a considerable amount of carbon-containing inclusions formed as a result of the thermal decomposition of the polymer. This is evidence of a local heating of the polymer coating above 700°C by the emission currents. This was accompanied by the transfer of a considerable amount of the carbon-containing material to anode and by nonuniform luminescence of the screen, whereby some emission centers disappeared and the new centers appeared.

Thus, it was demonstrated that the use of a polymer coating as the field electron emitter material may have good prospects in some applications because of (i) energy-saving technology, (ii) simplicity of cathode fabrication (preliminary sharpening of the cathode surface is not required), and (iii) good stability under the conditions of ion bombardment in technical vacuum.

Acknowledgments. The authors are grateful to A.V. Ankudinov for carrying out AFM measurements.

This study was supported by the Federal Program "Physics of Solid State Nanostructures."

REFERENCES

1. C. Lea, J. Phys. D **6**, 1105 (1973).
2. F. S. Baker, A. R. Osborn, and J. Williams, J. Phys. D **7**, 2105 (1973).
3. D. V. Kulikov, A. L. Suvorov, R. A. Suris, *et al.*, Pis'ma Zh. Tekh. Fiz. **23** (14), 89 (1997) [Tech. Phys. Lett. **23**, 573 (1997)].
4. L. A. Chernozatonskii, Z. Ya. Kosakovskaya, Yu. V. Gulyaev, *et al.*, J. Vac. Sci. Technol. B **14**, 2080 (1996).
5. M. W. Geis, J. C. Twichell, and T. M. Lyszczarz, J. Vac. Sci. Technol. B **14**, 2060 (1996).
6. A. N. Ionov, V. A. Zakrevskii, V. M. Svetlichnyi, and R. Rentzsch, in *Proceedings of the 10th International Symposium "Nanostructure: Physics and Technology," St. Petersburg, 2002*, p. 531.
7. J. Yilgor and B. C. Johnson, Polym. Prepr. (Am. Chem. Soc. Div. Polym. Chem.) **27**, 54 (1986).
8. V. M. Svetlichnyi, E. V. Arkhipova, V. M. Denisov, *et al.*, Vysokomol. Soedin., Ser. A **32**, 2075 (1990).
9. J. Lowell and A. C. Rose-Innes, Adv. Phys. **29**, 947 (1980).

Translated by P. Pozdeev

Technical Physics Letters, Vol. 30, No. 7, 2004, pp. 569–571. Translated from Pis'ma v Zhurnal Tekhnicheskoĭ Fiziki, Vol. 30, No. 13, 2004, pp. 83–88.
Original Russian Text Copyright © 2004 by Lysak, Trofimov.

On the Possibility of Obtaining Attosecond Pulse Trains during Second Harmonic Generation by High-Intensity Femtosecond Pulses

T. M. Lysak and V. A. Trofimov*
Moscow State University, Moscow, 119899 Russia
**e-mail: vatro@cs.msu.su*

Received December 12, 2003

Abstract—The possibility of obtaining attosecond pulse trains during second harmonic generation by high-intensity femtosecond pulses is demonstrated by means of computer simulation. The attosecond pulses are formed at the basic frequency with a low efficiency (≤8%) of the energy conversion from first to second harmonic. The regimes of attosecond pulse generation at the double frequency are considered. © *2004 MAIK "Nauka/Interperiodica".*

The problem of obtaining attosecond pulses has received much attention in recent years [1–7]. One possible method consists in the formation of a train of such pulses during the generation of a difference frequency in the terahertz range or during the cascade multiplication of the frequency of high-intensity femtosecond pulses [1, 2]. The latter approach is more interesting for us due to simultaneous manifestation of the nonlinearity of various orders for such pulses, since previously (see [8–11] and other papers) we studied the second harmonic generation (SHG) under similar conditions in order to provide for a high conversion efficiency.

Let us recall that doubling of the frequency of high-intensity femtosecond pulses is accompanied, in particular, by the phenomenon of optical bistability manifested in the formation of spatial contrast structures (in the one-dimensional case, kinks). The optical bistability may also lead to the appearance of temporal contrast structures in the form of sharp fronts. Therefore, using optical bistability and modulating a pulse, it is possible to form a sequence (train) of pulses whose width can be a factor of ten (or even more) smaller than that of the initial pulse. In the case considered below, the required modulation of the initial pulse is provided by the second-harmonic wave generated (in the given regime) with a 6–8% conversion of the primary pulse energy. The remaining energy is distributed (probably, in equal fractions) between subpulses of the basic-frequency wave. It should be noted, however, that a sequence of subpulses (or a single pulse) can also be obtained at the second harmonic frequency, but their energy will not exceed 60% of the primary pulse energy.

Assuming group synchronism, the SHG process under consideration can be described by the following system of equations written in terms of dimensionless variables:

$$\frac{\partial A_1}{\partial z} + iD_1\frac{\partial^2 A_1}{\partial \eta^2} + i\gamma A_1^* A_2 e^{-i\Delta kz} + i\alpha_1 A_1(|A_1|^2 + 2|A_2|^2) = 0,$$
$$0 < z \le L_z, \tag{1}$$
$$\frac{\partial A_2}{\partial z} + iD_2\frac{\partial^2 A_2}{\partial \eta^2} + i\gamma A_1^2 e^{i\Delta kz} + i\alpha_2 A_2(2|A_1|^2 + |A_2|^2) = 0,$$
$$\alpha_2 = 2\alpha_1 = 2\alpha.$$

Here, η is the dimensionless time in the frame of reference moving with the basic-frequency wave pulse; z is the normalized longitudinal coordinate, $D_j \sim -0.5\frac{\partial^2 \bar{k}_j}{\partial \bar{\omega}_j^2}$ are the coefficients characterizing the second-order dispersion of the jth wave; $\bar{k}_j$ and $\bar{\omega}_j$ are the dimensional wavenumber and frequency of the jth wave, respectively; γ is the nonlinear coupling coefficient of the interacting waves; $\Delta k = k_2 - 2k_1$ is the dimensionless detuning of the wavenumbers; α_j are the wave self-action coefficients; A_j are the complex amplitudes of the harmonics ($j = 1, 2$) normalized to the maximum amplitude of the first harmonic in the initial cross section of the medium ($z = 0$); and L_z is the length of the nonlinear medium.

In the input cross section, the initial pulse of the basic frequency is described by the Gaussian or hyper-Gaussian distribution

$$A_1(z = 0, \eta) = A_1^0(\eta) = \exp(-(\eta/\tau)^2/2),$$
$$0 \le \eta \le L_t, \tag{2}$$

1063-7850/04/3007-0569$26.00 © 2004 MAIK "Nauka/Interperiodica"

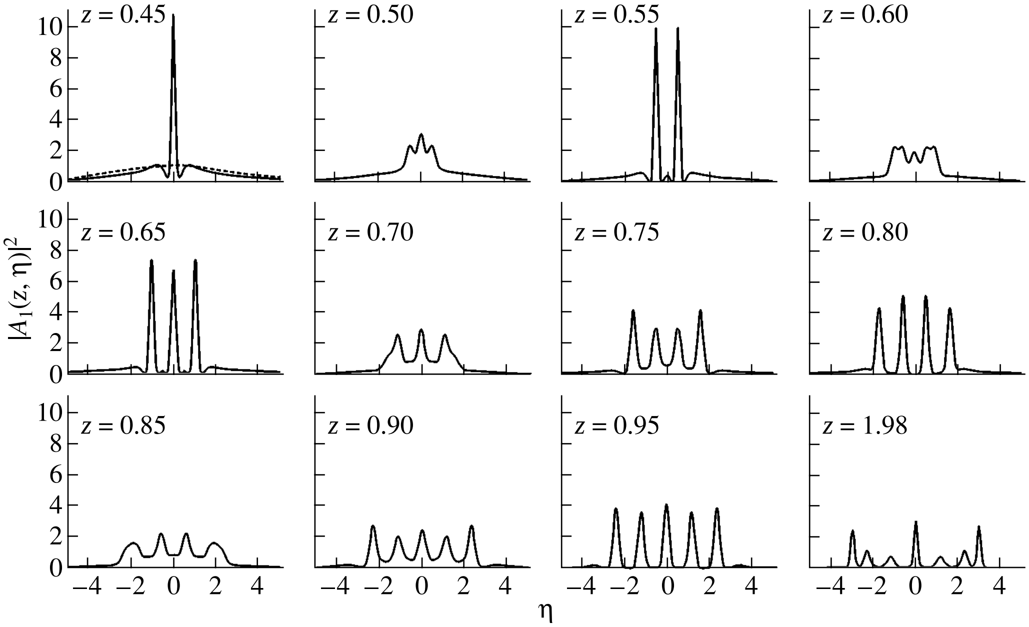

Fig. 1. Evolution of the basic-frequency pulse shape along the propagation axis (in various cross sections with the coordinate z) simulated for $\alpha = 16$, $\gamma = 4$, $\Delta k = -2$, $\tau = 4$, $D_1 = 1$, and $D_2 = -1.5$. Dashed curve in the cross section $z = 0.45$ shows a part of the initial femtosecond pulse.

where L_t is the dimensionless time interval during which the process is analyzed. The second-harmonic wave amplitude in the initial cross section is zero: $A_2(z = 0, \eta) = 0$.

Figure 1 shows an example of the regime of generation of a train of subpulses at the basic frequency, with a subpulse width equal to approximately 1/20 of the input pulse duration (for comparison, a part of the basic pulse is depicted as well). It should be noted that the pulse propagation regime under consideration is observed under certain conditions. First, cubic nonlinearity effects (wave self-action) must dominate over the quadratic nonlinearity manifestations. In this case, there are two SHG regimes corresponding to high and low conversion efficiency. Second, second-order dispersion must have opposite signs for the basic-frequency and second-harmonic waves (which frequently takes place in physical experiments) [12], whereby the pulse exhibits compression for the fundamental wave and decompression for the double frequency wave.

An analysis of Fig. 1 reveals several stages in the pulse propagation. In the first stage, the initial pulse exhibits compression over a pathlength of $z \leq 0.5$. As a result, the pulse width decreases by a factor of several tens with simultaneous tenfold growth of the pulse intensity. This subpulse occurs at the center of the initial pulse, above a background on the order of unity. It should be noted that this stage is most critical from the standpoint of experimental realization, since considerably increased intensity may lead to breakdown of the nonlinear medium. This poses limitations on the initial pulse intensity and implies selection of the nonlinear medium assuring realization of this regime.

In the course of subsequent propagation ($z > 0.5$), the basic-frequency pulse splits into subpulses with an intensity not exceeding several dimensionless units. The number of these subpulses is determined by the pathlength and increases with z. An increase in the number of pulses is accompanied by their virtually complete disappearance (Fig. 1). In the case under consideration, five identical subpulses with an intensity of 4 are formed at $z = 0.95$.

For a pathlength above $z = 1$, the formation of new subpulses continues, but we failed to obtain subpulses of equal amplitude for $z \leq 2$ (see Fig. 1, $z = 1.98$). Nevertheless, it should be noted that the time interval between subpulses keeps increasing, which may present certain interest in practical applications of the observed generation regime. Apparently, with further increase in the pathlength, the number of subpulses and the interval between them will continue to grow. However, this growth will slow down because of a decrease in the peak intensity for a part of subpulses.

Another remarkable peculiarity of the regime under consideration is the shape of separate subpulses, which is close to the classical soliton shape:

$$|A|^2 = I_0 ch^{-2}\left(\frac{\eta}{\tau_s}\right). \tag{3}$$

For example, Fig. 2b shows the shape of a subpulse formed at $z = 0.98$ approximated by function (3). As can be seen, the fit is very good. Small deviations observed at the leading and trailing pulse fronts are related to the onset of the process of merging into a single pulse, whereby the subpulses in this section are already somewhat coupled. In other sections, where the subpulses are well separated, the fit between subpulses and the approximation in the low-intensity parts is much better (see Fig. 2a for $z = 0.95$). Using this circumstance, it is possible to form solitons. To this end, it is necessary to change the properties of the medium past a certain cross section so as to eliminate the effects involving the quadratic nonlinearity.

An analogous behavior of the propagating femtosecond pulses is observed for other relations between the constants characterizing nonlinearities. In particular, the coefficient γ can be increased by a factor of two. Therefore, the results of calculations presented here are by no means the only possible realization of the regime of subpulse train formation.

It should be emphasized that there are several possibilities to reduce the maximum pulse intensity reached in a medium. For this purpose, it is possible either to select the medium (or the basic-frequency wavelength) in which both second-order dispersions are positive or to introduce a phase shift in a certain cross section [8–11]. Using any of these methods, it is possible to reduce the maximum pulse intensity by a factor of about 1.5 (to 5–6 dimensionless units) and to shift the corresponding cross section deeper into the medium.

To summarize, we point out that SHG by high-intensity femtosecond pulses leads under certain conditions to the formation of a train of regular subpulses at the basic frequency, whereby no more than 10% of the incident light pulse energy is converted in the second-harmonic wave energy. Therefore, the basic fraction of the initial energy is retained in the subpulses. The number of subpulses can be controlled by varying the length of the nonlinear medium. The second-harmonic wave is necessary for modulation of the basic-frequency pulse ensuring the contrast structure development due to a bistable generation regime.

In conclusion, it should be noted that our computer simulations also demonstrated the formation of separate subpulses (up to three) at the double frequency. However, the energies of these pulses were significantly lower than those of the basic-frequency subpulses in the case considered above. This is explained by the fact that the conversion efficiency with and without a phase shift introduced at a certain cross section does not exceed 60 and 30%, respectively.

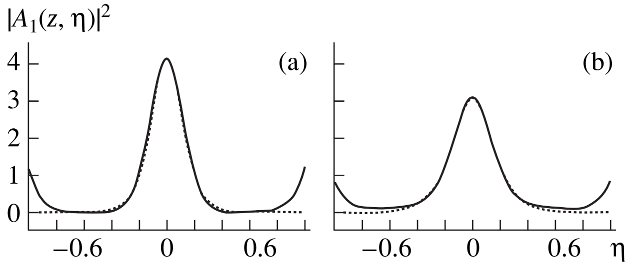

Fig. 2. A comparison the shape of an individual subpulse (solid curve) and soliton (the inverse hyperbolic cosine pulse according to formula (3)) in two cross sections (a) $z = 0.95$, $I_0 = 4.103$, $\tau_s = 0.15$; (b) $z = 0.98$, $I_0 = 3.04$, $\tau_s = 0.2$.

Acknowledgments. This study was supported by the Russian Foundation for Basic Research (project no. 02-01-727).

REFERENCES

1. N. A. Paradogiannis *et al.*, Phys. Rev. Lett. **90**, 133902 (2003).
2. N. A. Paradogiannis *et al.*, Appl. Phys. B **73**, 687 (2001).
3. C. Altucci *et al.*, Phys. Rev. A **61**, 021801 (2000).
4. P. M. Paul *et al.*, Science **292**, 1689 (2001).
5. D. Charalambidis *et al.*, Phys. Scr., T **105**, 23 (2003).
6. U. Teubner *et al.*, Phys. Rev. A **67**, 013816 (2003).
7. A. Hertz *et al.*, Phys. Rev. A **64**, 051801 (2001).
8. T. M. Lysak and V. A. Trofimov, Opt. Spektrosk. **93**, 861 (2002) [Opt. Spectrosc. **93**, 797 (2002)].
9. T. M. Lysak and V. A. Trofimov, Opt. Spektrosk. **92**, 323 (2002) [Opt. Spectrosc. **92**, 287 (2002)].
10. T. M. Lysak and V. A. Trofimov, Zh. Tekh. Fiz. **71** (11), 53 (2001) [Tech. Phys. **46**, 1401 (2001)].
11. T. M. Lysak and V. A. Trofimov, Opt. Spektrosk. **95**, 489 (2003) [Opt. Spectrosc. **95**, 455 (2003)].
12. X. Lui, K. Beckwitt, and F. Wise, Phys. Rev. E **62**, 1328 (2000).

Translated by P. Pozdeev

Technical Physics Letters, Vol. 30, No. 7, 2004, pp. 572–574. Translated from Pis'ma v Zhurnal Tekhnicheskoĭ Fiziki, Vol. 30, No. 13, 2004, pp. 89–94.
Original Russian Text Copyright © 2004 by Shuman, Savkina.

Graphitization of Porous 6H-SiC Layers during Thermal Treatment in Vacuum

V. B. Shuman* and N. S. Savkina
Ioffe Physicotechnical Institute, Russian Academy of Sciences, St. Petersburg, 194021 Russia
**e-mail: shuman@mail.ioffe.ru*

Received October 13, 2003; in final form, December 11, 2003

Abstract—We have studied the effect of thermal treatment in vacuum on the optical transmission of 6H-SiC samples with a porous layer on the Si face in the visible and near infrared spectral range. An analysis of changes in the absorption coefficient shows that the process of graphitization begins at a temperature below 700°C. *© 2004 MAIK “Nauka/Interperiodica”.*

As is known, the surface of silicon carbide (SiC) heated in vacuum exhibits a tendency to graphitization (on both Si and C faces) as a result of the thermal decomposition of SiC with the evaporation of Si atoms. This process was studied for a 6H-SiC(0001) surface by means of low-energy electron diffraction (LEED), Auger electron spectroscopy (AES), and other techniques [1–3], which gave somewhat different results. The AES data [1] showed that the onset of graphitization (T_1) takes place only after heating to 1000°C, whereby the peak of silicon decreases and the peak of carbon increases and changes shape from “carbide” to “graphite” type. According to the LEED data, annealing at 1000°C leads to the appearance of traces of a graphite structure in addition to the initial SiC structure, while only graphite structure is observed on the (0001) surface after heating to 1500°C. The results of ellipsometric measurements performed in the same investigation showed that layers with the optical constants characteristic of graphite appear at temperatures above 1200°C. At the same time, it was ascertained [1] that a graphite monolayer on the Si face may form already upon heating to 800°C. The results obtained in [2, 3] indicated that $T_1 \cong 1000$°C.

We have studied the process of graphitization in porous SiC (por-SiC). The porous material possesses a well-developed surface and can be studied by alternative methods.

The pores in 6H-SiC develop to form a herringbone pattern comprising a chain of tetrahedra aligned in directions close to the normal to the (0001) basal plane. The bases of these tetrahedra are parallel to the basal plane, while the vertices are directed outside of the porous layer [4, 5]. We have studied samples with a porosity of ≤20% (see table); therefore, the total area of bases in one layer of tetrahedra accounts for approximately the same fraction of monolayer. However, since the height of a tetrahedron is 20–50 nm, the chain length (equal to the porous layer thickness, which is on the order of 10 μm) accommodates several hundred tetrahedra. The absorption of light in such a structure must significantly increase compared to a flat surface, provided that the pore walls are covered with at least a monolayer of a substance whose absorption coefficient is substantially greater than that of SiC. Additional absorption may take place on three side faces of the tetrahedra, although we may suggest that the rates of graphitization on the side faces and basal plane are different. Indeed, it was shown [1, 2] that the rate of graphitization on the C face of SiC is markedly higher than that on the Si face. A considerable increase in the optical absorption of a porous material as a result of graphitization allows this effect to be detected and studied using relatively simple optical methods.

This study was aimed at determining the temperature of the onset of graphitization in porous 6H-SiC.

The experiments were performed with two polished *n*-type 6H-SiC plates. Sample 1 was prepared by the Lely method and had a concentration of uncompensated donors of $N_d – N_a = 4 \times 10^{17}$ cm^{-3}. Sample 2, with $N_d – N_a = 4.5 \times 10^{18}$ cm^{-3}, was obtained by a modified Lely technique (CREE Company) and characterized by a misorientation of 3.5° relative to the crystallographic *c* axis. The latter sample was divided into two parts (2a and 2b). The porous layers were formed on the Si faces of plates by electrochemical etching in HF–H_2O–C_2H_5OH (1 : 1 : 2) mixture under UV illumination. The etching was performed at a current density of 15 mA/cm^2 for 20 min (sample 1) and 15 min (sam-

Parameters of porous layers in 6H-SiC samples studied

Parameter	Sample 1	Sample 2
Porous layer thickness, μm	26.3 ± 0.5	(11.3–14.8) ± 0.5
Relative porosity, %	11 ± 1	17 ± 1
Effective pore diameter, nm	43.7	27.3

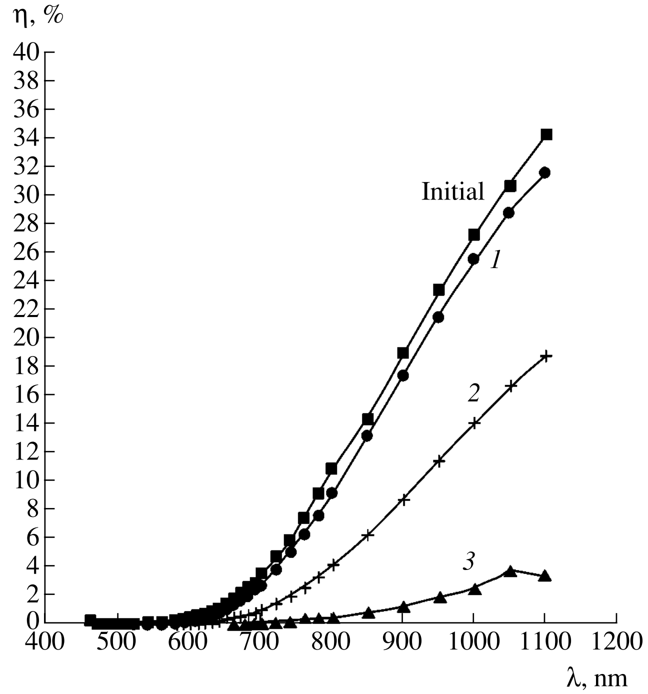

Fig. 1. Transmission spectra η(λ) of sample 1 before (initial) and after isochronous vacuum anneals for 1 h at (*1*) 700, (*2*) 1100, and (*3*) 1500°C.

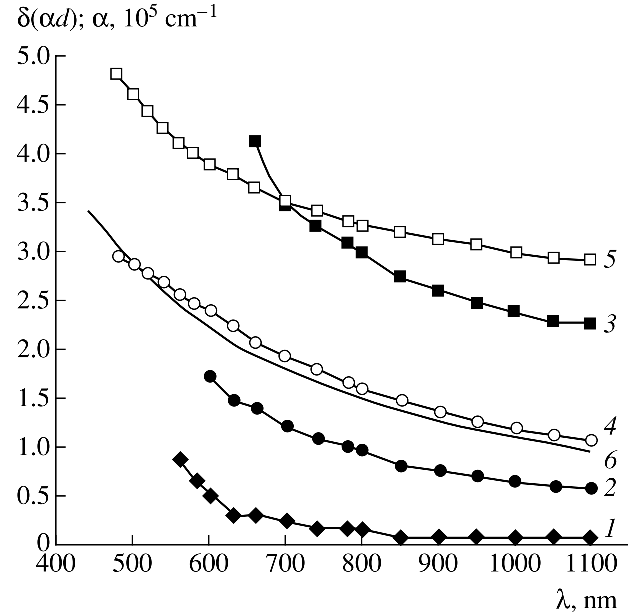

Fig. 2. Spectral dependences of increments of the absorption coefficient of porous layers in SiC samples 1 (curves *1*–*3* corresponding to T_a = 700, 1100, and 1500°C, respectively), 2a (*4*), and 2b (*5*) annealed in vacuum; curve *6* shows the corresponding dependence for a quasi-amorphous carbon phase calculated using data from [7].

ples 2a and 2b). The porous layer thickness was measured using a scanning electron microscope; the relative porosity was determined gravimetrically; the effective pore diameter was determined using an X-ray diffraction technique [5] based on the width of a diffuse halo in the X-ray rocking curve. These parameters of the porous structure of samples 1 and 2 are listed in the table. Considerable differences in the characteristics of samples 1 and 2 reflect the fact that the porosity in SiC significantly depends on the level of doping and on the density and types of structural defects [6], rather than on the duration of etching (the effective pore diameter and the relative porosity very slightly depend on the etching time).

The samples with porous layers were annealed in a vacuum of 10^{-6} Torr. Sample 1 was subjected to isochronous anneals for 1 h at T_a = 700, 1100, and 1500°C; sample 2a was annealed for 1 h only at 1100°C, and sample 2b, at 1500°C. The porous layers in annealed samples exhibited visible blackening. The spectral characteristics of the samples with porous layers were measured in the visible and near infrared (NIR) range using an SF-26 spectrophotometer. The measurements were performed before annealing and after each thermal treatment.

Figure 1 shows the results of measurements for sample 1. Small transmission in the visible range is explained by a strong scattering of visible light in the porous layer. As can be seen, a decrease in transmission is observed already after the first annealing at 700°C; the transmission significantly decreases with an increase in the annealing temperature.

Figure 2 shows the differential spectra representing the increment of the absorption index $\delta(\alpha d) = (\alpha d)_1 - (\alpha d)_2$ for all samples, where α is the absorption coefficient, *d* is the porous layer thickness, and subscripts 1 and 2 refer to the annealed and unannealed (initial) porous samples, respectively. For comparison, Fig. 2 shows the absorption spectrum α_g of a disordered quasi-amorphous carbon phase of graphitized type (curve *6*) calculated using the data from [7]. In all our samples, as well as in quasi-amorphous carbon, the absorption coefficient decreases with increasing wavelength λ. The distance between curves *1* and *2* also decreases with increasing λ. As the annealing temperature is increased further (from 1100 to 1500°C, curve *3*), this behavior is retained. However, the distance between curves *2* and *3* is 2.5–3 times that between curves *1* and *2*, which implies that the rate of graphitization increases with the annealing temperature (rather than remaining constant). These results may be indicative of a constant structure of the graphitized layer.

In samples 2a and 2b (which had identical characteristics of porous layers before annealing), the effect of the annealing temperature is different (Fig. 2, curves *4* and *5*, respectively). Probably, the annealing at 1500°C was accompanied by a certain transformation of the graphitized layer structure in sample 2b. A comparison of curves *2* and *4* (corresponding to the annealing at 1100°C) shows that δ(α*d*) for sample 2a is greater than that for sample 1, despite an almost half as small thickness of the porous layer in the former case (i.e., the relative increment in the absorption coefficient is even greater). This can be explained by higher relative porosity and smaller effective pore size and, hence, greater total pore surface in sample 2a than in sample 1.

As can be seen in Fig. 2, curves *4* and *6* virtually coincide in the entire spectral range studied. Therefore, we may suggest that the quasi-amorphous carbon phase in sample 2a is structurally close to that in a graphitized-type carbon phase studied in [7]. From this we can estimate the effective total thickness of the graphitized carbon layer in sample 2a as ~10^2 nm. This thickness corresponds to the absorption of chains composed of several hundred tetrahedra (assuming a monolayer coverage of the pore surface).

As can be seen from the data in Figs. 1 and 2, the process of graphitization on the Si face of 6H-SiC begins at a temperature certainly below 700°C, that is, at a much lower temperature than that reported for a polished surface of 6H-SiC [1–3]. This behavior can be explained at least by two factors. First, por-SiC possesses (despite relatively low porosity) a highly developed surface that can be roughly estimated as 300 cm^2 per 1 cm^2 of substrate area. Assuming that the quasi-amorphous carbon phase nucleates as islands growing to form a continuous films (rather than uniformly covering the pore surface from the very beginning), the possibility of detecting this phase is higher for optical methods that for the “local” surface techniques. Second, the rate of graphitization obviously depends on the crystallographic orientation of the surface. On the lateral faces of tetrahedra forming the pore surface, this rate can differ from that in the basal plane. As was noted above, it was shown [1, 2] that the rate of graphitization is much higher for the C face than for the Si face of SiC.

In conclusion, we have demonstrated that the process of graphitization in vacuum-annealed porous 6H-SiC begins at a temperature below 700°C. The rate of this process increases with the annealing temperature. The increment of the absorption coefficient of por-SiC upon annealing decreases with the wavelength, this spectral dependence being generally similar to the absorption spectrum of a quasi-amorphous carbon phase of graphitized type.

Acknowledgments. This study was supported by the Russian Foundation for Basic Research, project no. 01-02-17907.

REFERENCES

1. A. J. van Bommel, J. E. Crombeen, and A. van Tooren, Surf. Sci. **48**, 463 (1975).
2. L. Muehlhoff, W. J. Choyke, M. J. Bozak, *et al.*, J. Appl. Phys. **60**, 2842 (1986).
3. J. Forbeaux, J.-M. Themlin, and J.-M. Debever, Phys. Rev. B **58**, 16396 (1998).
4. J. S. Shor, J. Grimberg, B. Weiss, *et al.*, Appl. Phys. Lett. **62**, 2836 (1993).
5. N. M. Savkina, V. V. Ratnikov, and V. B. Shuman, Fiz. Tekh. Poluprovodn. (St. Petersburg) **35**, 159 (2001) [Semiconductors **35**, 153 (2001)].
6. V. B. Shuman, V. V. Ratnikov, and N. S. Savkina, Pis’ma Zh. Tekh. Fiz. **28** (10), 30 (2002) [Tech. Phys. Lett. **28**, 414 (2002)].
7. G. Jungk and C. H. Lange, Phys. Status Solidi B **50**, K71 (1972).

Translated by P. Pozdeev

Technical Physics Letters, Vol. 30, No. 7, 2004, pp. 575–577. Translated from Pis'ma v Zhurnal Tekhnicheskoĭ Fiziki, Vol. 30, No. 14, 2004, pp. 1–7.
Original Russian Text Copyright © 2004 by Ivanov, Kalinina, Konstantinov, Onushkin, Strokan, Kholuyanov, Hallén.

High-Resolution Short Range Ion Detectors Based on 4H-SiC Films

A. M. Ivanov, E. V. Kalinina, A. O. Konstantinov, G. A. Onushkin,
N. B. Strokan, G. F. Kholuyanov, and A. Hallén
Ioffe Physicotechnical Institute, Russian Academy of Sciences, St. Petersburg, 194021 Russia
ACREO AB, Electrum 236, SE 16440 Kista, Sweden
Department of Electronics, Royal Institute of Technology, Electrum 229, SE 16440 Kista, Sweden

Received January 14, 2004

Abstract—The energy resolution of SiC detectors has been studied in application to the spectrometry of α particles with 5.1–5.5 MeV energies. The Schottky barrier structure of the detector was based on a CVD-grown epitaxial *n*-4H-SiC film with a thickness of 26 μm and an uncompensated donor concentration of (1–2) × 10^{15} cm^{-3}. An energy resolution of 0.5% achieved for the first time with SiC detectors allows fine structure of the α particle spectrum to be revealed. The average energy of the electron–hole pair formation in 4H-SiC is estimated at 7.71 eV. © *2004 MAIK "Nauka/Interperiodica".*

Introduction. In recent years, silicon carbide (SiC) has proved to be a promising material for semiconductor detectors used for the registration and spectrometry of nuclear radiation. This is related to considerable progress in the technology of SiC films with characteristics acceptable for designing detectors, at least in the simplest variant of a two-electrode ionization chamber. Advantages of SiC over other materials (germanium, silicon, cadmium telluride) widely used in semiconductor detectors are a higher threshold energy of defect formation and a greater bandgap width. The former factor provides for a high stability of detector characteristics with respect to irradiation [1, 2], while the latter allows the current (and the related noise) generated in the detector volume to be reduced by several orders of magnitude. For this reason, SiC detectors are capable of operating at temperatures of up to 500°C [3], which, together with high stability under irradiation, makes these detectors unique devices for some special applications.

This Letter reports on the use of detectors based on 4H-SiC films for the spectrometry of short range ions, including α particles formed during the natural decay of elements. It will be demonstrated that the high quality of the obtained epitaxial SiC films allows an energy resolution of 0.5% to be reached.

Experimental methods. We have studied the characteristics of detectors based on 26-μm-thick epitaxial films of *n*-4H-SiC with an uncompensated donor concentration of N_d–N_a = (1–2) × 10^{15} cm^{-3}. The semiconductor films were grown by chemical vapor deposition (CVD) on commercial 4H-SiC substrates. Schottky barriers with an area of 1×10^{-2} cm^2 and a thickness of 0.1 μm and the Cr/Al base ohmic contacts were obtained by thermal deposition of chromium (see the inset in Fig. 1).

Characteristics of the SiC detectors were studied using a setup comprising an ORTEC Model 142 preamplifier, an ORTEC Model 571 amplifier with a passband controlled by RC filters, and a high-precision ORTEC Model 419 oscillator. The amplitude analyzer designed and developed at the St. Petersburg Institute of Nuclear Physics (Russian Academy of Sciences) had 4000 channels and was based on an RI 161.01 module linked to a computer. The analyzer scale was calibrated using a high-precision Si detector (developed at the Ioffe Physicotechnical Institute [4]) and a spectrometric source (S1) generating two groups of lines with ener-

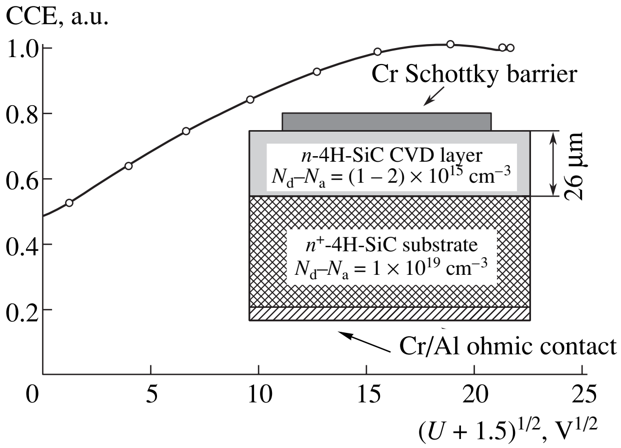

Fig. 1. A plot of the SiC detector response (normalized to the maximum signal amplitude) versus bias voltage. The inset shows the detector structure.

1063-7850/04/3007-0575$26.00 © 2004 MAIK "Nauka/Interperiodica"

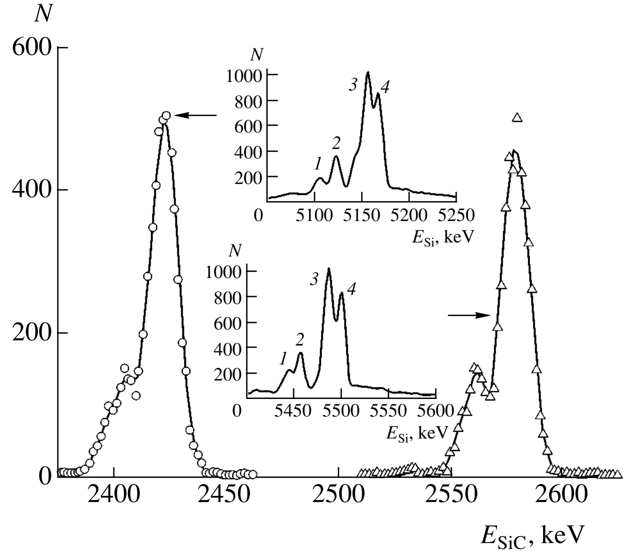

Fig. 2. The spectra of α decay in ^{239}Pu + ^{240}Pu (left) and ^{241}Am + ^{138}Pu (right) isotope mixtures measured using a SiC detector. The insets shows the same spectra measured using a Si detector, displaying peaks *1–4* with the energies 5105, 5124, 5157, and 5168 keV (top) and 5443, 5456, 5485, and 5499 keV (bottom), respectively.

gies in the vicinity of 5.49 MeV (^{241}Am + ^{238}Pu isotopes) and 5.16 MeV (^{239}Pu + ^{240}Pu isotopes).

The same S1 source was used for determining the limiting energy resolution. Another source (S2) of higher intensity had an energy of 5.39 MeV and a relative line width of 1% [full width at half maximum (FWHM) divided by the mean energy]. This source was used for rapid determination of the charge collection efficiency (CCE) and evaluation of the energy resolution. Besides the CCE and FWHM of the detector, we also determined the average energy ε_{SiC} of the electron–hole pair formation in 4H-SiC. All measurements of the CCE, FWHM, and ε_{SiC} values were performed under conditions of rough vacuum.

Results and discussion. Optimum conditions for the spectrometry of nuclear particles are determined by the relation $W \geq R$, where W is the length of a region occupied by the electric field and R is the particle range. For α particles with an energy of 5.5 MeV and R = 18 μm, the required values of $W \approx 20$ μm (corresponding to the lower boundary of the N_d–N_a interval indicated above) are achieved with a bias voltage of U = 365 V. In the obtained Schottky barriers, the values of reverse currents for applied voltages at least up to U = 500 V did not exceed 1 nA. This provided for a low noise level in the entire range of bias voltages used in the investigation of SiC detectors.

1. Figure 1 shows the typical plot of the detector response (normalized to the maximum signal amplitude) as a function of the bias voltage U (the contact potential difference was taken equal to U_c = 1.5 V). As can be seen, the detector output characteristic exhibits saturation in the region of U = 225–450 V, which is evidence in favor of the complete transfer of the nonequilibrium charge created by α particles. The bias voltage $U \approx 400$ V corresponds to an average field strength of $F \approx 2 \times 10^5$ V/cm, which is two orders of magnitude higher than the values typical of Si detectors. This is an important advantage, since the time of the diffusion drift track blurring (the stage immediately preceding the drift of charge carriers) is proportional to $1/F$.

It should be noted that, for U + 1.5 V = 0 V (where the charge transfer is determined predominantly by the diffusion of holes), the detector response reaches CCE ~ 0.5. This fact indicates that the diffusion length of holes (L_D) is comparable with the range of α particles. The L_D value can be estimated from the initial linear part of the plot in Fig. 1 using the relation

$$E(0) = (dE_\alpha/dx)L_D,$$

where $E(0)$ is the energy measured by the detector at U + 1.5 V = 0 V and $dE_\alpha/dx \approx 200$ keV/μm is the initial specific energy loss of α particles. For the data of Fig. 1, this formula yields L_D = 13.2 μm, which amounts to 75% of the range R. The slope of the linear portion agrees with the value of N_d–$N_a = 1.1 \times 10^{15}$ cm^{-3} determined from the results of capacitance measurements for the initial sample.

2. The presence of a region where CCE ≈ 1 in the plot of CCE(U) is a prerequisite for obtaining a high energy resolution. This characteristic was determined at a bias voltage of U = 450 V for two groups of α particles from S1 source. Each group contains lines separated by 10–14 keV, which could be resolved by the Si detector used for the analyzer calibration. These spectra, shown in the inset in Fig. 2, were used as the reference for comparison with the spectra obtained using our SiC detectors.[1]

As can be seen from Fig. 2, the SiC detector does not resolve the detailed structure of the energy spectrum: close doublets merge into a single line. However, the lines separated by ≈40 keV are clearly distinguished, which implies that this SiC detector reveals fine structure of the spectrum. The energy resolution is characterized by the value FWHM = 0.49–0.52%, which can be slightly corrected toward lower values by taking into account the noise contribution. For SiC detectors known previously, the minimum FWHM values amounted to 8–9% [5, 6].

Semiconductor detectors employ the so-called “ionization” principle of spectrometry, whereby the energy of detected ions is converted into the charge of nonequilibrium carriers. This conversion is accompanied by fluctuations in the number of electron–hole pairs,

---

[1] The presence of a background decaying toward high energies in the reference spectra is related to the high pulse count rate due to the significant (≈0.5 cm^2) area of the Si detector.

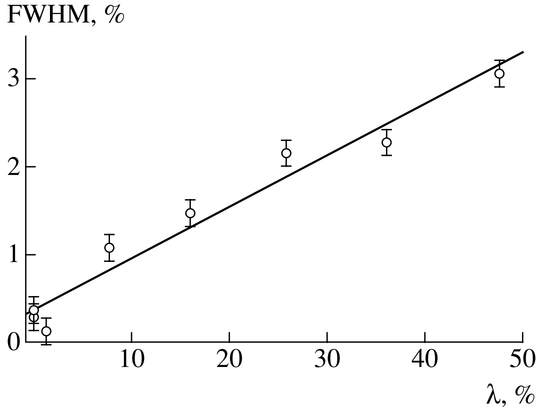

Fig. 3. A plot of the energy resolution of SiC detectors versus relative charge losses λ (determined for the region of $U \leq 225$ V in from Fig. 1).

which are related to the nuclear scattering of ions on atoms of the detector matrix and to the nature of impact ionization (produced both by δ electrons and by ions). In the case of silicon detectors, basic considerations restrict the possible FWHM value to ≈0.12%. Therefore, FWHM values on a level of 0.5% should be assigned to fluctuations of the ion charge (appearing during ion retardation) in the course of subsequent transfer in the bulk of the detector.

3. Obviously, the FWHM values must increase depending on the relative charge losses $\lambda = (q_0 - q)/q_0$, where q_0 is the charge produced by the ion and q is the detected charge. The values of λ determined using the data of Fig. 1 corresponded to the region of small displacements, where the charge transfer involves diffusion. According to [7], the dependence of FWHM on λ under these conditions has to be linear, in agreement with our results (Fig. 3). It should be noted that the slope of this line ($K = 0.06$) is small compared to that ($K = 0.36$) in the case of the Si detector studied in [7]. The coefficient K characterizes the inhomogeneity of charge losses over the detector area: a small K value is evidence of a perfect structure of the 4H-SiC epitaxial layer.

4. The average number of electron–hole pairs is determined by the energy ε required for the pair formation. According to [8], the corresponding value for α particles is $\varepsilon_{\mathrm{SiC}} = 8.4$ eV. However, recent X-ray emission data [9] showed that $\varepsilon_{\mathrm{SiC}} = 7.4$ eV.

In order to determine the value of ε corresponding to the films under consideration, we determined positions of the main peaks in the spectra of SiC detectors: $E_{\mathrm{SiC}} =$ 2579 and 2421 keV. Since these peaks correspond to the doublets observed in the spectra of Si detectors, we used their average energies $E_{\mathrm{Si}} = 5490$ and 5159 keV. Using the relation $\varepsilon_{\mathrm{SiC}} = \varepsilon_{\mathrm{Si}}(E_{\mathrm{Si}}/E_{\mathrm{SiC}})$ and assuming that $\varepsilon_{\mathrm{Si}} = 3.62$ eV, we obtain for both pairs $\varepsilon_{\mathrm{SiC}} = 7.71$ eV. It should be noted that this procedure does not take into account the energy losses of α particles in the “input window” of the detector. This role is played by a chromium film forming the Schottky barrier, in which the energy losses amount to ≈34 keV or ≈0.6%.

Conclusions. Using semiconductor detectors based on 4H-SiC films with Schottky barriers, we have reached an energy resolution of ≈0.5%, which makes it possible to reveal a fine structure in the spectra of α particles. This progress in the resolution is provided by favorable conditions of the nonequilibrium charge transfer, both with respect to increased diffusion lengths of charge carriers and the homogeneity of these values over the film volume (the homogeneity of L_D is at least comparable with that for Si detectors).

Conditions ensuring complete transfer of the charge, produced by α particles, during its drift in the electric field of the detector are established. The complete transfer was observed at an electric field strength not exceeding 2×10^5 V/cm. The absence of additional noise in this regime is evidence of the perfect structure of a CVD-grown epitaxial 4H-SiC film and the related Schottky barrier.

The average energy of electron–hole pair formation—an important spectrometric constant—was estimated as 7.71 eV, which is significantly smaller than the value (8.4 eV) reported previously.

Acknowledgments. This study was supported by the Russian Foundation for Basic Research (project no. 01-02-17911) and the Presidential Program of Support for Leading Scientific Schools in Russia (NSh-2223-2003.02).

REFERENCES

1. A. M. Ivanov, N. B. Strokan, D. V. Davidov, *et al.*, Appl. Surf. Sci. **184**, 431 (2001).
2. A. A. Lebedev, V. V. Kozlovski, N. B. Strokan, *et al.*, Mater. Sci. Forum **433–436**, 957 (2003).
3. E. V. Kalinina, G. F. Kholuyanov, D. V. Davydov, *et al.*, Fiz. Tekh. Poluprovodn. (Leningrad) **37**, 1260 (2003) [Semiconductors **37**, 1229 (2003)].
4. V. K. Eremin, E. M. Verbitskaya, N. B. Strokan, *et al.*, Zh. Tekh. Fiz. **56**, 1987 (1986) [Sov. Phys. Tech. Phys. **31**, 1186 (1986)].
5. V. A. Tikhomirova, O. P. Fedoseeva, and G. F. Kholuyanov, At. Énerg. **34**, 122 (1973).
6. A. A. Lebedev, A. M. Ivanov, and N. B. Strokan, Fiz. Tekh. Poluprovodn. (St. Petersburg) **38**, 129 (2004) [Semiconductors **38**, 125 (2004)].
7. N. B. Strokan, Pis’ma Zh. Tekh. Fiz. **24** (5), 44 (1998) [Tech. Phys. Lett. **24**, 186 (1998)].
8. M. Rogalla, K. Runge, and A. Soldner-Rembold, Nucl. Phys. B **78**, 516 (1999).
9. G. Bertuccio and R. Casigaghi, IEEE Trans. Nucl. Sci. **50**, 175 (2003).

Translated by P. Pozdeev

Technical Physics Letters, Vol. 30, No. 7, 2004, pp. 578–579. Translated from Pis'ma v Zhurnal Tekhnicheskoĭ Fiziki, Vol. 30, No. 14, 2004, pp. 8–12.
Original Russian Text Copyright © 2004 by Dmitriev, Psakhie.

Molecular-Dynamics Study of the Initial Stage of Nanoscale Deformation Localization in the Surface Layers of a Loaded Solid

A. I. Dmitriev* and S. G. Psakhie

Institute of Strength Physics and Materials Science, Siberian Division, Russian Academy of Sciences,
Tomsk, 634055 Russia
** e-mail: dmitr@usgroups.com*

Received December 2, 2003

Abstract—The nucleation and development of plastic deformation in the surface layers of a solid under dynamical loading conditions have been studied on a nanoscale level by computer simulation using molecular dynamics method. It is established that the onset of deformation localization is directly related to the loss of structural stability in the surface layers of a loaded solid, the appearance of surface local straining zones, and their spreading in the bulk of the material. This is preceded by uncorrelated atomic displacements in the near-surface region of the solid. The obtained results agree with the well-known experimental data and confirm the special role of the surface layers of solids in the onset and development of plastic deformation. *© 2004 MAIK "Nauka/Interperiodica".*

Unique properties of the surface as a special state of the solid is extensively investigated and discussed in many applications of modern materials science [1, 2]. However, the substantial role of the surface in the development of plastic deformation was originally recognized and rationalized within the framework of physical mesomechanics. It was shown [3–5] that the surface layers of solids represent an independent level of plastic deformation, which plays an important role in the behavior of the whole deformed body. It should be emphasized that this special role is related not only to the initial defect nature of the surface or the influence of surrounding medium but also to a reduced stability of the surface layers with respect to shear [5].

The onset of deformation processes has been extensively studied by advanced experimental methods such as scanning tunneling microscopy, atomic force microscopy, and scanning electron microscopy [6, 7]. Nevertheless, the initial stage of the process of deformation localization still remains unstudied because such investigations require an unprecedented combination of extremely high temporal (10^{-9} s) and spatial (10^{-10} m) resolution. This circumstance accounts for the considerable interest in atomic-scale modeling of the elementary processes involved in the nucleation and development of plastic deformation in the surface layers of solids.

In this context, the molecular dynamics modeling of the elementary events of plastic deformation near the free surface of a solid is of interest both for the development of basic notions about the nucleation and development of these processes on the nanostructural level and for the possible practical applications.

The model crystal is schematically depicted in Fig. 1, where region I is a freely strained part of the crystal, while regions II simulate the external load. In our model, the latter regions represent the so-called string boundary conditions [8]. According to these, the projections of atomic velocities onto the [001] direction in regions II are fixed at –50 and 50 m/s (for the top and bottom surface, respectively), which corresponds to dynamic compression. These conditions have certain advantages over, for example, rigid boundary conditions, since the behavior of atoms in directions other than [001] is not specified and is determined by the atomic environment. In order to take into account the extension of the model fragment in the [010] direction, we used periodic boundary conditions in the [010] direction and simulated free boundaries in the [100] direction. The interatomic interactions were described within the framework of the method of embedded atom [9]. In order to avoid the induced effects related to the symmetry of the ideal crystal lattice, the model copper crystal was heated to 20 K. The dynamic loading was applied

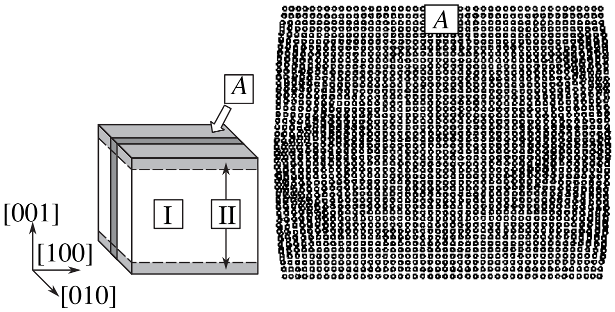

Fig. 1. The structure of fragment *A* of the model crystal deformed to ε = 12.5%. The thickness of fragment *A* corresponds to three interplanar distances.

1063-7850/04/3007-0578$26.00 © 2004 MAIK "Nauka/Interperiodica"

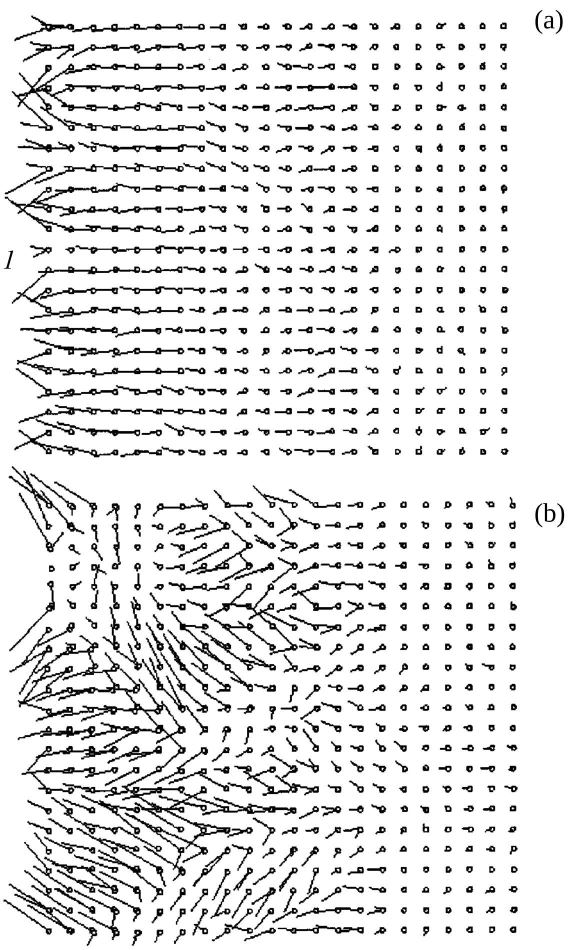

Fig. 2. Atomic displacements during the same time interval for the model crystal deformed to (a) 11 and (b) 12.5% (*1* is the free surface of the crystal).

after the initial structure relaxation at this temperature, which provided for equilibrium atomic configurations in the surface layers of the model crystal.

The results of our simulations showed that, after reaching a certain initial degree of straining of the model crystal, the formation and development of deformation localization bands occur. Detailed analysis showed that these bands nucleate on the free surface. The centers of nucleation of the deformation localization bands occur in the region of stress concentrators, namely, in the middle parts of the free surfaces (which is related to the regime of loading and the crystal geometry) and in the boundary regions between the deformed region I and regions II. This is clearly illustrated in Fig. 1, showing the structure of a fragment of the model crystal at the moment of time corresponding to the onset of formation of the deformation localization bands. As can be seen, the process of deformation localization begins on the surface and then proceeds in depth of the material.

Figure 2 shows the patterns of atomic displacements during equal time intervals in the plane situated in the central part of the deformed region I and parallel to the (001) crystal plane in the model crystal under different loads. The thickness of this fragment in the [001] direction corresponds to two atomic planes. For the sake of better illustration, the length of bars representing atomic displacements is increased by a factor of 10. Note that, in the initial stage of loading, the atomic displacements exhibit a correlated character and are directed outward from the bulk to the free surface. Allowance for a finite temperature introduces a certain scatter in the directions of displacements but does not change the general pattern of correlated displacements.

In the stage immediately before the appearance of the deformation localization bands, the surface layer exhibits a significant disorientation of atomic displacements (Fig. 2a). This is evidence of instability of the atomic configurations formed in the near-surface region. The absolute values of atomic displacements on the surface are significantly (by a factor of up to 10) greater than those in the bulk. Apparently, a change in the atomic structure only in the near-surface region cannot provide for further energy dissipation. This unavoidably involves deeper layers into this process, which is clearly seen in Fig. 2b. Thus, being initially formed on the surface, large atomic displacements propagate into the bulk in the form of localized deformation bands.

Acknowledgments. This study was supported in part by the Presidential Program of Support for Leading Scientific Schools in Russia (project no. NSh-2324.2003.1), the Ministry of Defense of the Russian Federation (project no. PD02-1.5-425), and the US Civilian Research and Development Foundation for the Independent States of the Former Soviet Union (CRDF grant no. TO-016-02).

REFERENCES

1. J. D. Eshelby, *Boundary Problems* (North-Holland, Amsterdam, 1979).
2. V. P. Alekhin, *The Physics of Strength and Plasticity of the Surface Layers of Materials* (Nauka, Moscow, 1983) [in Russian].
3. V. E. Panin, Theor. Appl. Fract. Mech. **37**, 261 (2001).
4. V. E. Panin, Fiz. Mezomekh. **4** (3), 5 (2000).
5. V. E. Panin, V. M. Fomin, and V. M. Titov, Fiz. Mezomekh. **6** (2), 5 (2003).
6. A. V. Panin, V. A. Klimenov, N. L. Abramovskaya, *et al.*, Fiz. Mezomekh. **3** (1), 83 (2000).
7. V. I. Vettegren’, S. Sh. Rakhimov, and V. N. Svetlov, Fiz. Tverd. Tela (St. Petersburg) **40**, 2180 (1998) [Phys. Solid State **40**, 1977 (1998)].
8. A. I. Mel’ker, A. I. Mikhaĭlin, and E. Ya. Baĭguzin, Fiz. Met. Metalloved. **64**, 1066 (1987).
9. G. G. Rusina, A. V. Berch, I. Yu. Sklyadneva, *et al.*, Fiz. Tverd. Tela (St. Petersburg) **38**, 1120 (1996) [Phys. Solid State **38**, 619 (1996)].

Translated by P. Pozdeev

Technical Physics Letters, Vol. 30, No. 7, 2004, pp. 580–582. Translated from Pis’ma v Zhurnal Tekhnicheskoĭ Fiziki, Vol. 30, No. 14, 2004, pp. 13–19.
Original Russian Text Copyright © 2004 by Petrov, Kaĭdash, Krasovitskiĭ, Sokolov, Pogorel’skiĭ, Chalyĭ, Shkurko, Stepanov, Pavlenko, Baranov.

MBE of InGaN/GaN Heterostructures Using Ammonia as a Source of Nitrogen

S. I. Petrov, A. P. Kaĭdash, D. M. Krasovitskiĭ, I. A. Sokolov, Yu. V. Pogorel’skiĭ,
V. P. Chalyĭ, A. P. Shkurko, M. V. Stepanov, M. V. Pavlenko, and D. A. Baranov
“ATC–Semiconductor Technologies and Equipment” Joint-Stock Company, St. Petersburg, Russia
e-mail: support@semiteq.ru

Received September 16, 2003; in final form, December 11, 2003

Abstract—InGaN/GaN heterostructures have been grown by molecular beam epitaxy (MBE) using ammonia as a source of nitrogen. The influence of the growth temperature and rate on the incorporation of indium into the epitaxial layers and the position of the corresponding photoluminescence peak has been studied. Based on these data, optimum growth conditions have been selected for the ammonia MBE of InGaN layers in the active region of light-emitting diodes operating in the blue/violet spectral range. *© 2004 MAIK “Nauka/Interperiodica”.*

Introduction. During the past decade, semiconductor compounds based on group III metal nitrides have entered the group of most promising materials for modern optoelectronics. Various types of light-emitting diodes (LEDs) based on these materials are now fabricated on a large scale and the first commercial solid state nitride lasers have been created. As a rule, ternary compounds of the InGaN system are used as materials for the active region of lasers emitting in the visible spectral range.

Despite all achievements, obtaining high-quality InGaN for optoelectronic devices still encounters certain difficulties. These include, in particular, large misfit between the lattice parameters of unstrained crystals. As a result, thin InGaN epilayers on relatively thick GaN and AlGaN substrates always occur in a stressed state. When the epitaxial layer thickness exceeds a certain critical value corresponding to the pseudomorphous growth, this stress favors phase separation of the indium-containing layers with the appearance of regions depleted of and enriched in indium up to the formation of pure InN [1]. Another problem is related to the fact that the pressure of indium vapor is lower than that of gallium vapor, while the thermal stability of InN is much lower than that of GaN. For this reason, the usual growth temperatures for InGaN are much lower than those for GaN [2, 3]. Therefore, epilayers with a large content of In atoms can be obtained either by decreasing the growth temperature (which results in reduced mobility of atoms on the growth surface and, hence, in decreased structural perfection of epilayers) or by increasing the flux of In atoms (which leads to the formation of indium droplets on the growth surface and pure indium inclusions in the InGaN matrix). In addition, experimental data show that the content of indium in the final solid solution strongly depends on the ratio of incident fluxes of In and Ga atoms and on the ratio of the flux of group V elements to the total flux of group III elements [4, 5].

At present, the most widely used method of fabrication of the GaN-based device heterostructures is metalorganic vapor phase epitaxy (MOVPE) [6]. However, progress achieved in recent years in the development of molecular beam epitaxy (MBE) makes this method competitive to MOVPE with respect to the quality of epitaxial layers, the possibility of growing doped layers, and applicability to device structure fabrication. High-quality GaN layers can be obtained by MBE using either gaseous ammonia or nitrogen plasma as a source of nitrogen [7, 8]. Ammonia MBE is more attractive because it allows the growth to be performed at a higher temperature compared to that for the plasma MBE, thus ensuring a higher quality of nitride epilayers. LEDs with an active InGaN region emitting in the blue spectral range were obtained only using MBE with ammonia as a source of nitrogen [9].

This Letter presents the results of investigation of the influence of the growth temperature and rate on the incorporation of indium into the epitaxial InGaN layers grown by ammonia MBE and on their luminescent properties. Based on these data, optimum growth conditions have been selected for the growth of InGaN-based active regions of light-emitting diodes with room-temperature luminescence in the blue spectral range.

Experimental. Epitaxial InGaN and GaN layers were grown using an ATC-EPN1 system specially designed for the MBE of group III nitrides using ammonia as a source of nitrogen. The epitaxial films were grown on sapphire substrates coated with molybdenum from the rear side (for radiative heating) and mounted in indium-free substrate holders. The growth temperature was calibrated with respect to the rate of the thermal evaporation of gallium and the temperature of the onset of gallium nitride decomposition at a given flux of ammonia. The epitaxial growth rate and layer thickness was determined using a He–Ne laser interferometer.

Prior to layer growth, the sapphire substrate was nitrided in a flow of ammonia (20 sccm) at 950°C. Then, the temperature was reduced to 500°C for growing a 25-nm-thick buffer GaN layer and increased again at a rate of 30 K/min up to the onset of GaN decomposition (900°C) in a flow of ammonia (80 sccm), after which the ammonia flux was decreased to 20 sccm, the flow of gallium vapor was switched on, and a 0.5-μm-thick GaN layer was grown at a rate of 1 μm/h. Finally, the substrate temperature was decreased to 580–680°C and an InGaN layer was deposited onto GaN at a rate of 0.1 or 0.05 μm/h. The content of indium in epilayers was determined by X-ray diffraction. The photoluminescence (PL) spectra were excited by a 5-mW He–Cd laser and measured at 77 and 300 K.

Results and discussion. Figure 1a shows the PL spectra measured at 77 K for 50-nm-thick InGaN epilayers grown on GaN at 580, 630, and 680°C at a rate of 0.1 μm/h and at 680°C and 0.05 μm/h. Data on the indium content in InGaN epilayers (determined by X-ray diffraction) and on the edge luminescence peak energy are presented in the table. As the InGaN layer growth temperature increases, the peak of luminescence at 77 K shifts toward shorter wavelengths (from 2.75 to 3.17 eV) and increases in intensity by approximately one and a half orders of magnitude. For the layer grown at 580°C, the edge PL peak is positioned at 2.75 eV and its intensity is comparable with that of the yellow (“defect”) and blue (“donor–acceptor”) emission bands and the edge emission peak of gallium nitride. The content of indium in this layer according to the X-ray diffraction data amounts to 15%. As the growth temperature increases to 630°C, the peak of InGaN luminescence shifts to 2.88 eV and exhibits a tenfold increase in intensity, while the content of indium in the layer decreases to 11%. The shortwave shift is caused by a decrease in the indium content with increasing growth temperature. The increase in intensity is probably related to improved structure of the InGaN layer, while the greater width (FWHM) of the PL peak can be explained by inhomogeneity of the indium distribution in the layer. When the growth temperature is elevated to 680°C, the PL peak exhibits an additional twofold increase in intensity and shifts to 3.17 eV, while the indium content drops to 3%. A decrease in the growth rate by half, achieved by reducing the flux of gallium at a constant flux of indium, leads to only a slight increase in the indium content (4%) and a more pronounced change in the PL peak position (from 3.17 to 3.06 eV).

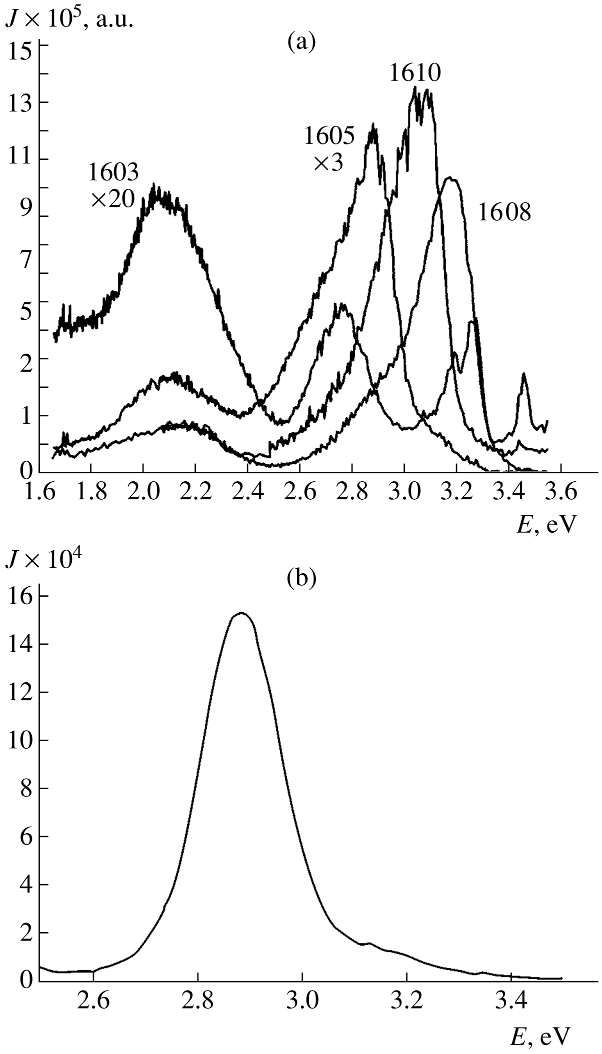

Fig. 1. PL spectra of InGaN epilayers on GaN: (a) luminescence at 77 K from InGaN grown at 580°C (sample 1603), 630°C (1605), and 680°C (1608) at a rate of 0.1 μm/h and at 680°C and 0.05 μm/h (1610); (b) room-temperature luminescence from a three-layer heterostructure with InGaN layers grown at 650°C.

Figure 2 shows plots of the bandgap width versus indium content in InGaN solid solutions according to the data of different researchers. One of these dependences was calculated assuming that the bandgap of $In_xGa_{1-x}N$ varies from 1.9 to 3.49 eV with a sag parameter of $b = 1$ [6], while the other curve was calculated as $E_g = 3.493 - 2.843x - 2.5x(1 - x)$, assuming that InN is

PL peak energy (77 K) and indium content in InGaN layers growth by ammonia MBE under various conditions

Sample	InGaN growth temperature, °C	InGaN growth rate, μm/h	InGaN emission peak, eV	In content, % (X-ray data)
1603	580	0.1	2.75	15
1605	630	0.1	2.88	11
1608	680	0.1	3.17	3
1610	680	0.05	3.06	4

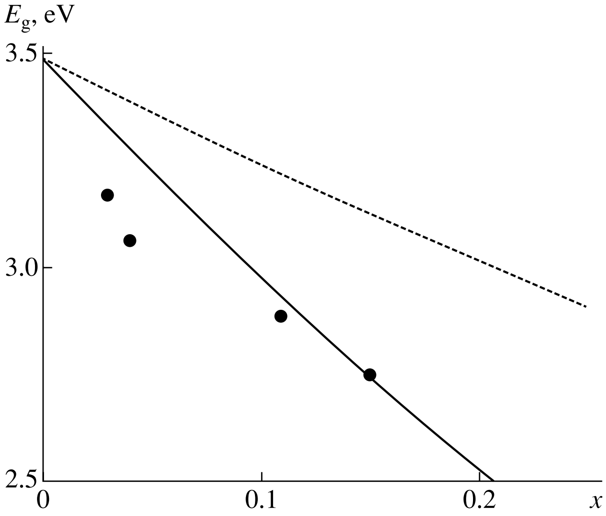

Fig. 2. Plots of the bandgap width E_g (77 K) versus indium content x in $In_xGa_{1-x}N$ solid solutions: (dashed line) calculation [6]; (solid line) calculation [10]; (points) experiment (this study).

a narrow-bandgap semiconductor [10]. Experimental points in Fig. 2 represent our data for the PL peak position in InGaN epilayers with various indium concentrations. As can be seen, an increase in the content of indium in the InGaN layer is accompanied by increasing Stokes shift relative to the calculated values from [6], in agreement with the data published in [11]. At the same time, the experimental points for $x = 15$ and 11% exhibit a better fit to the curve calculated according to [10]. As the indium content decreases, the experimental points deviate from this calculated curve toward greater emission wavelengths. However, it should be noted that a decrease in the indium content is accompanied by an increase in the uncertainty of X-ray diffraction measurements.

Based on the data presented above, the MBE growth at a temperature of 650°C is considered as optimum for obtaining structures with a room-temperature edge luminescence peak in the blue spectral range without significant loss of the emission intensity caused by a decrease in the quality of structures grown at a reduced temperature. The room-temperature PL spectrum of a sample comprising three pairs of InGaN/GaN (30 nm/30 nm) epilayers grown at 650°C on an 0.5-μm-thick high-temperature GaN sublayer exhibits a dominating emission peak at 2.88 eV (Fig. 1b). Therefore, these growth conditions can be considered as optimum for the ammonia MBE of InGaN layers in the active region of LEDs operating in the blue/violet spectral range.

Conclusions. In InGaN/GaN heterostructures grown by MBE using ammonia as a source of nitrogen, the content of indium in InGaN layers obtained in the interval of substrate temperatures 580–680°C varies from 15 to 3% and the edge luminescence peak (77 K) shifts from 2.75 to 3.17 eV. A change in the growth rate at the expense of the Ga/In flux ratio at a fixed substrate temperature does not lead to proportional variations in the layer composition. Based on the results of experiments, optimum conditions are established for the MBE growth of InGaN-based active region for LEDs with a dominating peak of emission in the blue spectral range.

REFERENCES

1. M. Beharama *et al.*, Mater. Res. Soc. Symp. Proc. **572**, 357 (1999).
2. D. E. Lackinson *et al.*, J. Appl. Phys. **78**, 1838 (1995).
3. S. Strite *et al.*, J. Cryst. Growth **127**, 204 (1993).
4. N. Grandjean and J. Massies, Appl. Phys. Lett. **72**, 1078 (1998).
5. T. Bottcher *et al.*, Appl. Phys. Lett. **73**, 3232 (1998).
6. S. Nakamura and G. Fasol, *The Blue Laser Diode* (Springer, Berlin, 1997).
7. G. Popovici, H. Morkoc, and S. Mohammad, in *Group III Nitride Semiconductor Compounds*, Ed. by B. Gil (Clarendon Press, Oxford, 1998).
8. N. Grandjean *et al.*, J. Appl. Phys. **83**, 1379 (1998).
9. S. Dalmasso *et al.*, Mater. Sci. Eng. B **82**, 256 (2001).
10. V. Yu. Davydov *et al.*, Phys. Status Solidi B **234**, 787 (2002).
11. R. Martin *et al.*, Appl. Phys. Lett. **74**, 263 (1999).

Translated by P. Pozdeev

Technical Physics Letters, Vol. 30, No. 7, 2004, pp. 583–584. Translated from Pis'ma v Zhurnal Tekhnicheskoĭ Fiziki, Vol. 30, No. 14, 2004, pp. 20–24.
Original Russian Text Copyright © 2004 by Andrianov, Ivanov, Polsky.

Threshold Sensitivity of Anti-Stokes Frequency Converter

S. N. Andrianov*, V. P. Ivanov, and Yu. E. Polsky
State Institute of Applied Optics, Federal Unitary Enterprise, Kazan, Tatarstan, Russia
** e-mail: andrianov@bancorp.ru*

Received December 4, 2004

Abstract—Expressions describing the threshold sensitivity of a quantum converter of IR radiation into visible light are obtained for two schemes of energy levels in the active atoms. Based on these expressions, practical criteria for the creation of such devices are formulated. *© 2004 MAIK “Nauka/Interperiodica”.*

In 1959, Bloembergen [1] suggested to use the anti-Stokes luminescence of rare-earth metal ions for the conversion of IR radiation into visible light. Later [2–6], this anti-Stokes conversion was studied in the general case for two schemes of atomic energy levels depicted in Figs. 1 and 2. The aim of this study was to determine and compare the threshold sensitivity of the anti-Stokes conversion in these schemes. The analysis is performed using the method of rate equations under the assumption that the energies of pump and anti-Stokes radiation photons are significantly greater than the average phonon energy in the converter.

Consider a system of three-level atoms interacting with electromagnetic field and thermal oscillations of a matrix crystal lattice according to the energy scheme of Fig. 1. In this scheme, pump photons n_p convert atoms from the ground state 1 to an excited state 2 and signal photons n_s convert atoms from this state to another excited state 3, after which atoms exhibit 3 $\longrightarrow$ 1 transitions with spontaneous emission of photons n_{f1}. In addition, this scheme features phonon-induced 2 $\longrightarrow$ 3 transitions $\Phi(T)$ and 2 $\longrightarrow$ 1 transitions with spontaneous emission of photons n_{f2}.

The system of rate equations for the populations N_1, N_2, and N_3 of the corresponding levels in the above scheme can be written as

$$\begin{gathered}\frac{dN_3}{dt} = -A_{31}N_3 - \sigma_{31}n_{f1}(N_3 - N_1)\\ -A_{32}N_3 - \sigma_{32}n_s(N_3 - N_2) - R_{32}N_3 - R_{32}\Phi(T)(N_3 - N_2),\\ \frac{dN_2}{dt} = -A_{21}N_2 - \sigma_{21}n_{f2}(N_2 - N_1)\\ -\sigma_{21}n_p(N_2 - N_1) + A_{32}N_3\\ +\sigma_{32}n_s(N_3 - N_2) + R_{32}N_3 + R_{32}\Phi(T)(N_3 - N_2),\\ N_1 + N_2 + N_3 = N,\end{gathered} \tag{1}$$

where A_{mn} are the rates of spontaneous photon emission for the transitions between levels m and n ($m \longrightarrow n$), σ_{mn} are the cross sections for the induced photon emission in the $m \longrightarrow n$ transitions, R_{32} is the rate of spontaneous emission for the 3 $\longrightarrow$ 2 transition, and N is the total number of atoms in the system studied. Assuming the number of photons due to fluorescence to be small and ignoring the corresponding terms in Eqs. (1), we obtain the following expression for the signal-to-noise ratio:

$$\frac{S}{N} = \frac{\sigma_{32}n_s}{R_{32}\Phi(T)}. \tag{2}$$

Now, let us proceed to a system of three-level atoms interacting with electromagnetic field and thermal

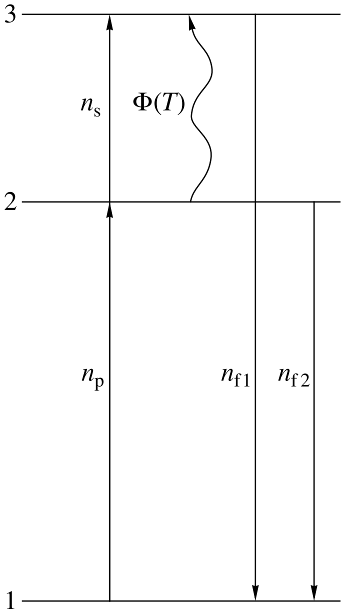

Fig. 1. Schematic diagram of the energy levels and transitions in a converter with IR photon absorption during transition from an excited state.

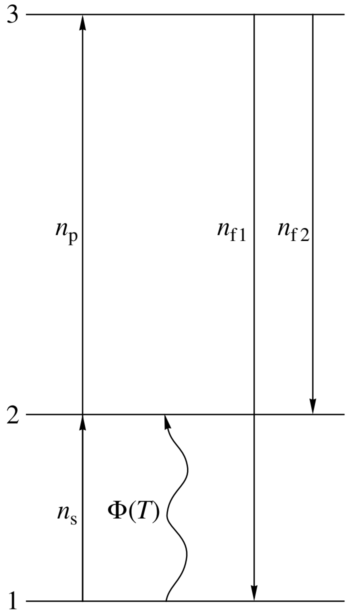

Fig. 2. Schematic diagram of the energy levels and transitions in a converter with IR photon absorption during transition from the ground state.

oscillations of the matrix crystal lattice according to the energy scheme of Fig. 2. In this case, signal photons n_s convert atoms from the ground state 1 to an intermediate excited state 2 and pump photons n_p convert atoms from this state to another excited state 3, after which atoms exhibit 3 ⟶ 1 transitions with spontaneous emission of photons n_{f1}. In addition, this scheme features phonon-induced 1 ⟶ 2 transitions Φ(*T*) and 3 ⟶ 2 transitions with spontaneous mission of photons n_{f2}.

The system of rate equations for the populations N_1, N_2, and N_3 of the corresponding levels in this scheme can be written as

$$\begin{gathered}\frac{dN_3}{dt} = -A_{31}N_3 - \sigma_{31}n_{f1}(N_3 - N_1) \\ - A_{32}N_3 - \sigma_{32}n_{f2}(N_3 - N_2) - \sigma_{32}n_{f2}(N_3 - N_2), \\ \frac{dN_2}{dt} = -A_{21}N_2 - \sigma_{21}n_s(N_2 - N_1) \\ + A_{32}N_3 + \sigma_{32}n_{f2}(N_3 - N_2) \\ + \sigma_{32}n_p(N_3 - N_2) + R_{32}N_2 + R_{32}\Phi(T)(N_1 - N_2), \\ N_1 + N_2 + N_3 = N,\end{gathered} \tag{3}$$

where R_{21} is the rate of spontaneous emission for the 2 ⟶ 1 transition. Assuming the number of photons due to fluorescence to be small and ignoring the corresponding terms in Eqs. (3), we obtain the following expression for the signal-to-noise ratio in this scheme:

$$\frac{S}{N} = \frac{\sigma_{21}n_s}{R_{21}\Phi(T)}. \tag{4}$$

The threshold sensitivity of a converter is determined from the condition $S/N = 1$. Using formulas (2) and (4), we obtain for the minimum detectable number of IR signal photons

$$n_{th} = \Phi(T)\frac{R_{mn}}{\sigma_{mn}}, \tag{5}$$

where $m = 3$, $n = 2$ for scheme 1 and $m = 2$, $n = 1$ for scheme 2.

An analysis of formula (5) shows that the threshold sensitivity increases with increasing cross section for the IR photon induced transition (3 ⟶ 2 and 2 ⟶ 1 for the schemes in Figs. 1 and 2, respectively) and with decreasing rate of the phonon-induced transitions. This implies that, in order to increase the threshold sensitivity, it is necessary to satisfy the following criteria: (i) to select ions with a level structure such that levels 2 and 3 in the scheme of Fig. 1 and levels 1 and 2 in the scheme of Fig. 2 would belong to different terms, and (ii) to select a matrix such that the electron–phonon coupling between impurity ions and the matrix would be weak.

According to criterion (i), the scheme of Fig. 1 is preferred for the creation of an anti-Stokes converter because levels close to the ground state level in most of the rare-earth metal ions belong to same term as the latter level. Criterion (ii) indicates that converters should be based on crystals with small intensity of the phonon branch of the absorption band of impurity ions. Estimates show that, for example, Eu^{3+} ions in the matrices with small electron–phonon coupling such as LaF_3 and $LaBr_3$ [7] at a working temperature of 77 K (typical of the IR converters) ensure a threshold sensitivity of no less than 10^{18} photons/m^2.

REFERENCES

1. N. Bloembergen, Phys. Rev. Lett. **2** (3), 84 (1959).
2. J. F. Porter, Phys. Rev. Lett. **7**, 414 (1961).
3. M. R. Brown and W. A. Shand, Phys. Rev. Lett. **11**, 366 (1963).
4. M. R. Brown and W. A. Shand, Phys. Rev. Lett. **12**, 367 (1964).
5. J. C. Wright, F. K. Fong, and M. M. Miller, J. Appl. Phys. **42**, 3806 (1971).
6. L. Esterowitz, Schilzer, J. Noonan, and J. Bahler, Appl. Opt. **7**, 2053 (1968).
7. Yu. P. Chukova, *Anti-Stokes Luminescence and Its New Possible Applications* (Sov. Radio, Moscow, 1980).

Translated by P. Pozdeev

Technical Physics Letters, Vol. 30, No. 7, 2004, pp. 585–586. Translated from Pis'ma v Zhurnal Tekhnicheskoĭ Fiziki, Vol. 30, No. 14, 2004, pp. 25–28.
Original Russian Text Copyright © 2004 by Usanov, Gorbatov.

Magnetic-Field-Controlled Optical Transmission in a System of Metal Diaphragms with Apertures and a Thin Dielectric Interlayer

D. A. Usanov* and S. S. Gorbatov

Saratov State University, Saratov, Russia

** e-mail: usanovda@info.sgu.ru*

Received December 15, 2003

Abstract—A system comprising two metal diaphragms with holes and a thin dielectric interlayer exhibits magnetic-field-controlled optical transmission. This phenomenon can be used, in particular, for the creation of light modulators. © *2004 MAIK "Nauka/Interperiodica".*

Previously [1], it was shown that a system of the "metal–thin dielectric layer–diaphragm with aperture" type exhibits resonance absorption of IR radiation. This effect was explained in terms of the interaction between the metal surface and the near field of an electromagnetic field distorted by the hole. It was suggested that the observed phenomenon can be used for controlling radiation.

In particular, we propose to control radiation in such a system by means of an applied magnetic field. This possibility is related to the generation of Hall currents in the metal diaphragms, with the current lines perpendicular to those of a current passing in the diaphragm in the absence of magnetic field. The Hall currents appear as a result of the Lorentz force acting upon charge carriers in the metal exposed to a magnetic field. This force produces bending of the current lines and distorts the near field of the transmitted radiation. The bending of current lines has to be manifested, in particular, by rotation of the polarization plane of the radiation passing through the diaphragm. The degree of rotation must be proportional to the magnetic field strength. In order to increase the effect, the apertures in the metal diaphragms can be made in the form of mutually perpendicular slits. In this case, rotation of the polarization plane under the action of a magnetic field will increase the effective overlap area of the slits acting as the entrance and exit holes in a system of the transmission resonator type. Since the dimensions of this resonator are small, even small distortion of the electric field of a light wave, caused by application of an external magnetic field, will significantly change the effective overlap area of the slits and, hence, the wave transmission coefficient.

This Letter reports on the results of experimental verification of the mechanism of magnetic-field-controlled light transmission in a system of the type described above.

The experiments were performed with a system consisting of two layers of ~100-μm-thick aluminum foil, each with a 20 × 5000-μm rectangular slit. The metal layers were separated by natural insulating 100-Å-thick passive films of aluminum oxide [1]. For two foil sheets tightly pressed to each other by means of thermal compression, the total thickness of the dielectric layer amounted to 200 Å. The slits were oriented perpendicularly to each other, so that the incident radiation in the absence of an external magnetic field passed through a 20 × 20-μm overlap region.

The experimental setup (Fig. 1) comprised a radiation source *1* (AL307BM light-emitting diode operating at 0.66 μm) pressed into a hole in the magnetic guide *2*.The system of metal diaphragms *3* separated by

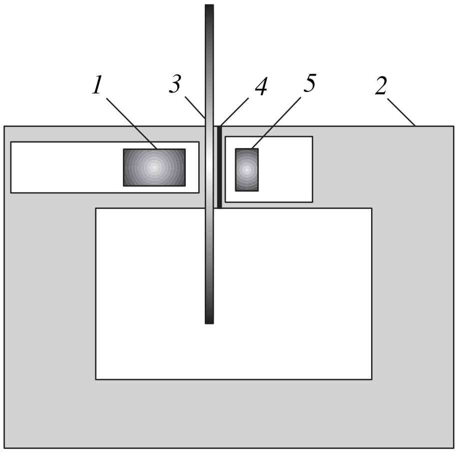

Fig. 1. Schematic diagram of the experimental setup (see the text for explanations).

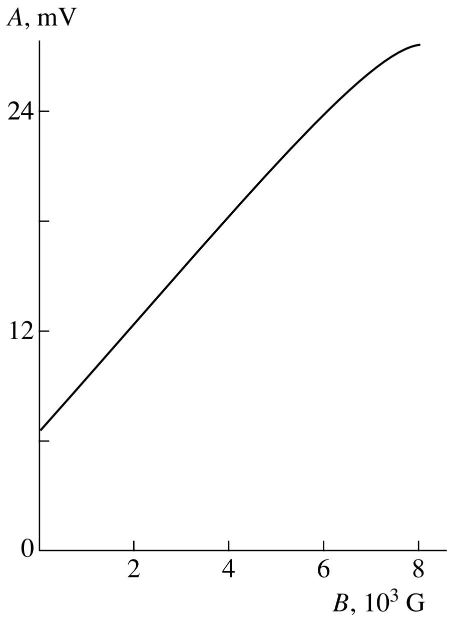

Fig. 2. A plot of the photodetector response voltage *A* versus magnetic induction *B*.

a dielectric film was placed in the gap of electromagnet. The magnetic field strength was controlled by varying the gap width and measured by Hall sensor *4*. The intensity of transmitted light was measured using a photodetector *5* based on an *n*–*i*–*p*–*i*–*n* silicon structure positioned close to the diaphragms with apertures.

As can be seen from the results of measurements presented in Fig. 2, a change in the magnetic induction *B* from zero to 8000 G is accompanied by an increase in the photodetector response from 6.6 to 27.6 mV. This behavior indicates that the optical transmission of the system varies with the applied magnetic field. It should be noted that no such variation in the transmitted light intensity was observed for a single-layer system with one diaphragm. Nor did the applied magnetic field directly influence the LED output and/or photodetector response.

Thus, we have demonstrated that a system comprising two metal diaphragms with apertures and a thin dielectric interlayer exhibits magnetic-field-controlled optical transmission of incident radiation. This phenomenon can be used for the creation of effective light modulators.

REFERENCES

1. D. A. Usanov and S. S. Gorbatov, Pis’ma Zh. Tekh. Fiz. **27** (21), 81 (2001) [Tech. Phys. Lett. **27**, 926 (2001)].

Translated by P. Pozdeev

Technical Physics Letters, Vol. 30, No. 7, 2004, pp. 587–590. Translated from Pis’ma v Zhurnal Tekhnicheskoĭ Fiziki, Vol. 30, No. 14, 2004, pp. 29–36.
Original Russian Text Copyright © 2004 by Koronovskiĭ, Hramov.

Chaotic Phase Synchronization Studied by Means of Continuous Wavelet Transform

A. A. Koronovskiĭ and A. E. Hramov*

Saratov State University, Saratov, Russia

** e-mail: aeh@cas.ssu.runnet.ru*

Received December 25, 2003

Abstract—A new approach to introduction of the phase of a chaotic signal is developed based on the continuous wavelet transform. The proposed method is applied to the study of phase synchronization of two chaotic dynamical systems with ill-defined phases. *© 2004 MAIK “Nauka/Interperiodica”.*

The phase synchronization of systems occurring in the regime of dynamical chaos [1–3] is one of the most important phenomena studied by modern theory of nonlinear oscillations. The effect of chaotic phase synchronization was experimentally observed in radio frequency generators [4], lasers [5], electrochemical oscillators [6], heart rhythm [7], gas discharge [8], etc. (see also [3, 9, 10]). Investigations into this phenomenon are also very important from the standpoint of data transmission by means of deterministic chaos [11].

The phenomenon of phase synchronization is usually described and analyzed in terms of the phase $\phi(t)$ of a chaotic signal [1, 3, 9, 10]. The phase synchronization implies that phases of the chaotic signals become entrained, while their amplitudes remain uncorrelated and appear as chaotic. The phase entrainment leads to coincidence of the signal frequencies, which are determined as average rates of the phase variation $\langle\dot{\phi}(t)\rangle$.

There is no universal method for introducing the phase of a chaotic signal which would provide correct results for arbitrary dynamical systems. Several methods have been developed for “well-behaving” systems with a relatively simple topology of chaotic attractors. First, the phase $\phi(t)$ of a chaotic signal is frequently introduced as an angle in the polar coordinate system on the (x, y) plane [12]. Second, the phase of a chaotic system is defined by considering an analytical expression $\zeta(t) = x(t) + jH[x(t)] = A(t)e^{j\phi(t)}$ [1, 9], where $H[x(t)]$ is the Hilbert transform of the chaotic signal $x(t)$ [13]. Third, the phase of a chaotic signal is defined on a surface of the Poincaré cross section and it is assumed that the signal phase exhibits linear variation in the interval between two sequential intersections of the phase trajectory with the Poincaré cross section [1, 3, 9]. All these approaches give analogous correct results for well-behaving systems [1, 3, 9, 10]. On the other hand, these methods frequently lead to incorrect results for the systems with ill-defined phases (see, e.g., [3, 15]). In such cases, the phase synchronization can be revealed by means of indirect measurements [3, 9, 14].

Below, we propose a new method for establishing the phase synchronization of dynamical systems with ill-defined phases. The behavior of such a system can be described by introducing a continuous set of phases determined by means of the continuous wavelet transform [16, 17] of a chaotic signal $x(t)$:

$$W(s, t_0) = \int_{-\infty}^{+\infty} x(t)\psi^*_{s,t_0}(t)dt, \qquad (1)$$

where $\psi_{s,t_0}(t)$ is the wavelet function (the asterisk denotes complex conjugation) obtained from the base wavelet $\psi_0(t)$

$$\psi_{s,t_0}(t) = \frac{1}{\sqrt{s}}\psi_0\left(\frac{t-t_0}{s}\right), \qquad (2)$$

s is the analyzed time scale determining the width of the $\psi_{s,t_0}(t)$ wavelet, and t_0 is the shift of the wavelet function along the time axis. Note that, in the wavelet analysis, the concept of “time scale” is usually employed instead of the term “frequency” traditionally used in the Fourier transform analysis.

For the base wavelet, we use the Morlet wavelet $\psi_0(\eta) = (1/\sqrt[4]{\pi})\exp(j\omega_0\eta)\exp(-\eta^2/2)$ [16]. Selection of the wavelet parameter $\omega_0 = 2\pi$ provides for the relation $s \simeq 1/f$ between the time scale s of the wavelet transform and the frequency f of the Fourier transform.

The wavelet surface

$$W(s, t_0) = |W(s, t_0)|\exp[j\phi_s(t_0)] \qquad (3)$$

describes the behavior of the system for each time scale s at any moment of time t_0. The magnitude of $|W(s, t_0|$ characterizes the presence and intensity of the corre-

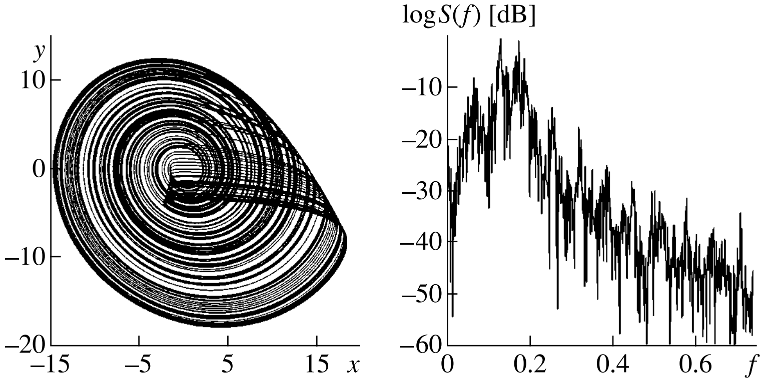

Fig. 1. The projection of a phase portrait on the (x, y) plane and the power spectrum of the first Rössler system (coupling parameter $\varepsilon = 0$).

sponding time scale s at the moment of time t_0. It is also convenient to introduce the integral distribution of the wavelet energy with respect to the time scales

$$E(s) = \int |W(s, t_0)|^2 dt_0.$$

The phase is naturally defined as $\phi_s(t) = \arg W(s, t)$ for each time scale s. In other words, it is possible to characterize the behavior of each time scale s in terms of the associated phase $\phi_s(t)$.

Let us consider the behavior of two mutually coupled nonidentical chaotic oscillators. If these oscillators do not occur in the state of phase synchronization, their behavior is not synchronized for all time scales s. As soon as some of the time scales of these dynamical systems become synchronized (e.g., as a result of increase in the coupling parameter), the phase synchronization regime is established. Evidently, this synchronization primarily takes place for the time scales corresponding to the maximum energy fraction of the wavelet spectrum $E(s)$, while the other scales remain desynchronized. The phase synchronization leads to the phase entrainment on the synchronized time scales s such that

$$|\phi_{s1}(t) - \phi_{s2}(t)| < \text{const}, \tag{4}$$

where $\phi_{s1,2}(t)$ are continuous phases of the first and second oscillators corresponding to the synchronized time scales s.

The proposed approach based on the continuous wavelet transform can be successfully applied to any dynamical systems, including those with ill-defined phases. For example, let us consider the behavior of two mutually coupled nonidentical Rössler systems occurring in the vortex chaos regime (Fig. 1):

$$\begin{aligned} \dot{x}_{1,2} &= -\omega_{1,2} y_{1,2} - z_{1,2} + \varepsilon(x_{2,1} - x_{1,2}), \\ \dot{y}_{1,2} &= \omega_{1,2} x_{1,2} + a y_{1,2} + \varepsilon(y_{2,1} - y_{1,2}), \\ \dot{z}_{1,2} &= p + z_{1,2}(x_{1,2} - c), \end{aligned} \tag{5}$$

where ε is the coupling parameter, $\omega_1 = 0.98$, $\omega_2 = 1.03$, $a = 0.22$, $p = 0.1$, and $c = 8.5$.

Figure 2 shows the results of calculations for two mutually coupled Rössler systems in the case of a small coupling parameter ($\varepsilon = 0.025$). The wavelet transform power spectra $E(s)$ of the two systems differ in shape (see Fig. 2a), but the maximum values of the energy ε correspond to approximately the same time scale s. According to Fig. 2a, the phase difference $\phi_{s1}(t) - \phi_{s2}(t)$ exhibits infinite growth for all time scales. This implies that no synchronized time scales exist in the systems under consideration and, hence, the systems exhibit no phase synchronization.

As the coupling parameter increases, the systems exhibit phase synchronization (see, e.g., [12]). The results of indirect measurements [14] showed that the coupled Rössler systems occur in the regime of phase synchronization when $\varepsilon = 0.05$. Behavior of the phase difference $\phi_{s1}(t) - \phi_{s2}(t)$ in this case is illustrated by Fig. 2b. As can be seen, there is phase synchronization for the time scale $s = 5.25$ (characterized by a maximum energy of the wavelet spectrum $E(s)$ (Fig. 2b). Thus, the time scales $s = 5.25$ of the two Rössler systems are synchronized. Simultaneously, all the time scales in the nearest vicinity of $s = 5.25$ are synchronized as well. Strongly different time scales (e.g., $s = 4.5$ or 6.0) remain unsynchronized (see Fig. 2b in comparison to Fig. 2a).

Further increase in the coupling parameter (e.g., to $\varepsilon = 0.07$) leads to phase synchronization for the time scales where no such synchronization took place before. As can be seen from Fig. 2c, the time scales $s = 4.5$ in the two coupled systems are synchronized (in contrast to the case when $\varepsilon = 0.05$, illustrated in Fig. 2b). The interval of time scales featuring phase entrainment increases, but some time scales (e.g., $s = 3.0$ and 6.0 in Fig. 2c) remain desynchronized as before.

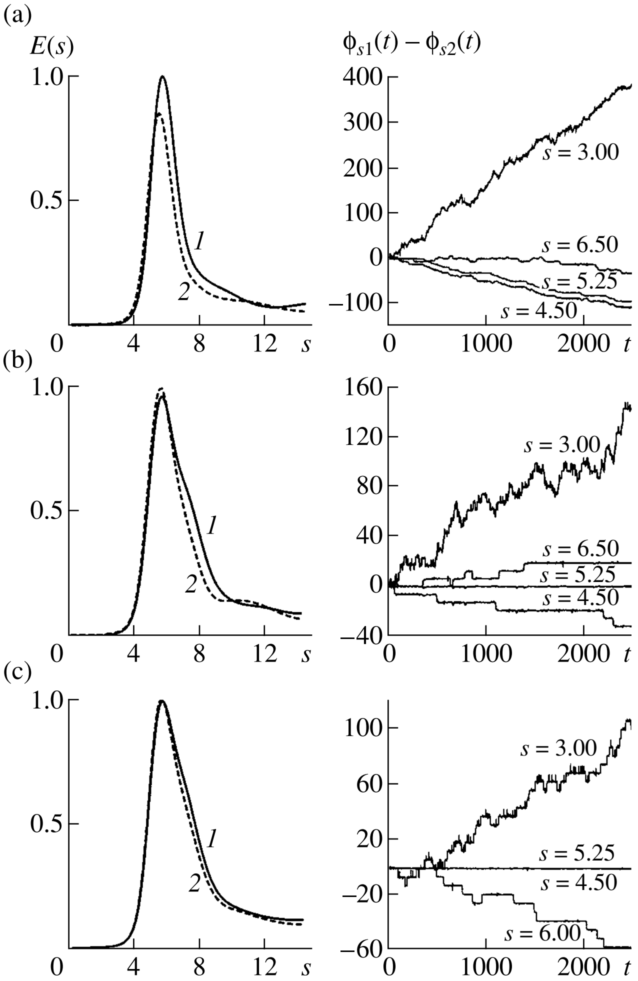

Fig. 2. Normalized energy spectra $E(s)$ of the wavelet transforms for the first (solid curves *1*) and second (dashed curves *2*) Rössler systems and behavior of the phase difference $\phi_{s1}(t) - \phi_{s2}(t)$ of these systems for various coupling parameter: (a) $\varepsilon = 0.025$ (no phase synchronization); (b) $\varepsilon = 0.05$ (time scales $s = 5.25$ are synchronized and the two systems exhibit phase synchronization); (c) $\varepsilon = 0.07$ (the number of synchronized time scales and the interval of phase synchronization increase).

The above results reveal several important aspects. First, traditional approaches to determining phase synchronization based on the introduction of a chaotic signal phase provide a correct description for time series characterized by the Fourier spectrum with a sharply pronounced main frequency f_0. In such cases, the phase ϕ_{s0} introduced for the time scale $s_0 \simeq 1/f_0$ approximately coincides with the chaotic signal phase $\phi(t)$ introduced in the classical way. Indeed, since the other frequencies (or the other time scales) are not pronounced in the Fourier spectrum, the phase $\phi(t)$ of the characteristic signal is close to $\phi_{s0}(t)$ for the main frequency f_0 (and, accordingly, for the main time scale s_0). Obviously, the average frequencies $f = \langle \dot{\phi}(t) \rangle$ and $\bar{f}_{s0} = \langle \dot{\phi}_{s0}(t) \rangle$ must also coincide with each other and with the main frequency f_0 of the Fourier spectrum: $\bar{f} = \bar{f}_{s0} = f_0$ (see also [15]).

If the given chaotic time series is characterized by a Fourier spectrum featuring no clearly pronounced main spectral component (as, e.g., in the spectrum of the Rössler system in Fig. 1), the traditional approaches to introduction of the chaotic signal phase (mentioned in the Introduction) are no longer valid and may lead to incorrect results. In contrast, the proposed approach based on a continuous wavelet transform and introduction of a continuous phase set can be applied to description of a chaotic signal of any type.

The second important circumstance is that the proposed method requires no a priori information about the system studied and, hence, can be used for an analysis of experimental data. Moreover, use of the wavelet analysis sometimes decreases the influence of noise [16, 18]. It is quite possible that the method described above can also be useful and effective in the analysis of time series generated by physical, biological, physiological, and other systems.

Thus, we have proposed a new approach to description of the phenomenon of phase synchronization, which is based on the continuous wavelet transform and analysis of the system dynamics for various time scales. This approach can be used for the description of any chaotic systems (including those with ill-defined phases) and experimental time series.

Acknowledgments. This study was supported by the Russian Foundation for Basic Research and the US Civilian Research and Development Foundation for Independent States of the Former Soviet Union (CRDF Award No. REC-006).

REFERENCES

1. M. G. Rosenblum, A. S. Pikovsky, and J. Kurths, Phys. Rev. Lett. **76**, 1804 (1996).
2. G. V. Osipov, A. S. Pikovsky, M. G. Rosenblum, and J. Kurth, Phys. Rev. E **55**, 2353 (1997).
3. A. Pikovsky, M. Rosenblum, and J. Kurths, *Synchronization: A Universal Concept in Nonlinear Sciences* (Cambridge Univ. Press, Cambridge, 2001).
4. U. Parlitz, L. Junge, and W. Lauterborn, Phys. Rev. E **54**, 2115 (1996).
5. E. Allaria *et al.*, Phys. Rev. Lett. **86**, 791 (2001).
6. I. Z. Kiss and J. L. Hudson, Phys. Rev. E **64**, 046215 (2001).
7. V. S. Anishchenko *et al.*, Int. J. Bifurcation Chaos Appl. Sci. Eng. **10**, 2339 (2000).
8. C. M. Ticos *et al.*, Phys. Rev. Lett. **85**, 2929 (2000).
9. A. Pikovsky, M. Rosenblum, and J. Kurths, Int. J. Bifurcation Chaos Appl. Sci. Eng. **10**, 2291 (2000).

10. V. S. Anishchenko and T. E. Vadivasova, Radiotekh. Élektron. (Moscow) **47**, 117 (2002).
11. A. S. Dmitriev and A. I. Panas, *Dynamical Chaos: New Information Media for Communication Systems* (Fizmatlit, Moscow, 2002) [in Russian].
12. M. G. Rosenblum, A. S. Pikovsky, and J. Kurths, Phys. Rev. Lett. **78**, 4193 (1997).
13. V. S. Anishchenko, V. Astakhov, A. Neiman, T. Vadivasova, and L. Schimansky-Geier, *Nonlinear Dynamics of Chaotic and Stochastic Systems. Tutorial and Modern Developments* (Springer-Verlag, Heidelberg, 2001).
14. M. G. Rosenblum, A. S. Pikovsky, and J. Kurths, Phys. Rev. Lett. **89**, 264102 (2002).
15. V. S. Anishchenko and T. E. Vadivasova, Radiotekh. Élektron. (Moscow) **49** (2004) (in press).
16. A. A. Koronovskiĭ and A. E. Hramov, *Continuous Wavelet Analysis and Its Applications* (Fizmatlit, Moscow, 2003).
17. J. P. Lachaux *et al.*, Int. J. Bifurcation Chaos Appl. Sci. Eng. **10**, 2429 (2000).
18. V. A. Gusev, A. A. Koronovskiĭ, and A. E. Hramov, Pis'ma Zh. Tekh. Fiz. **29** (18), 61 (2003) [Tech. Phys. Lett. **29**, 775 (2003)].

Translated by P. Pozdeev

Technical Physics Letters, Vol. 30, No. 7, 2004, pp. 591–594. Translated from Pis'ma v Zhurnal Tekhnicheskoĭ Fiziki, Vol. 30, No. 14, 2004, pp. 37–45.

Original Russian Text Copyright © 2004 by Shalyguina, Škorvánek, Švec, Molokanov, Mel'nikov.

Inverted Surface Hysteresis Loops in Heterogeneous (Nanocrystalline/Amorphous) $Fe_{81}Nb_7B_{12}$ Alloys

E. E. Shalyguina[a],*, I. Škorvánek[b], P. Švec[c], V. V. Molokanov[d], and V. A. Mel'nikov[c]

[a] *Moscow State University, Moscow, 119899 Russia*
[b] *Institute of Experimental Physics, Slovakian Academy of Sciences, SK-043 53 Košice, Slovakia*
[c] *Institute of Physics, Slovakian Academy of Sciences, SK-842 28 Bratislava, Slovakia*
[d] *Baikov Institute of Metallurgy and Materials Science, Russian Academy of Sciences, Moscow, 117334 Russia*
** e-mail: shal@magn.ru*

Received January 20, 2004

Abstract—Inverted hysteresis loops were observed for the first time in the near-surface layers of heterogeneous (nanocrystalline/amorphous) $Fe_{81}Nb_7B_{12}$ alloys. In particular, a negative residual magnetization is retained when a positive magnetic field applied in the sample plane is decreased to zero. The inverted hysteresis is qualitatively explained within the framework of a two-phase model, according to which the heterogeneous alloys contain two dissimilar phases exhibiting uniaxial magnetic anisotropy and featuring antiferromagnetic exchange interaction. © *2004 MAIK "Nauka/Interperiodica".*

Introduction. Recently, nanocrystalline materials of a new type were obtained by method of amorphous precursor crystallization [1, 2]. The new materials have attracted much attention because of their unique magnetic, mechanical, and kinetic properties. Iron-based Fe–M–B (M = Zr, Ta, Mo, and Nb) alloys (NANOPERM^{TM}) have proved to be most promising due to relatively simple composition and unique soft magnetic properties [2, 3]. The magnetic properties of Fe–M–B alloys (in particular, of the FeNbB system) have been studied by various experimental techniques (see, e.g., [2–10]). It was established that FeNbB alloys annealed in the range from 300 to 1050 K behave as materials containing two—amorphous and nanocrystalline—ferromagnetic phases and that the volume fraction of the nanocrystalline phase depends on the method and temperature of treatment of the initial alloy.

An important role in the formation of magnetic properties of materials is played by the surface. As is known, inhomogeneities in the microstructure and chemical composition of amorphous materials account for a significant (up to tenfold) increase in the surface coercive force H_C and saturation field H_S as compared to the corresponding volume values [11, 12]. Moreover, these inhomogeneities significantly influence the course of crystallization in amorphous materials during their heat treatments used for obtaining heterogeneous alloys containing two or more ferromagnetic phases.

This paper reports the results of a comparative study of the surface and volume magnetic properties of heterogeneous $Fe_{81}Nb_7B_{12}$ alloys containing two (amorphous and nanocrystalline) ferromagnetic phases.

Experimental. Amorphous $Fe_{81}Nb_7B_{12}$ ribbons with a width of 6 mm and a thickness of 30 μm were obtained by rapid solidification via melt spinning. The as-quenched ribbons were annealed in an argon atmosphere for 1 h at 550°C (sample 1) and 600°C (sample 2). The microstructure of samples was studied by X-ray diffraction. An analysis of the diffraction patterns showed that the samples of both types contain amorphous and nanocrystalline phases. The size of nanocrystalline bcc Fe grains formed as a result of annealing was 10–12 nm. It was found that the volume fractions of amorphous and nanocrystalline phases are 66.5 and 24.1% in sample 1 and 53.9 and 38.6% in sample 2. Thus, the volume fraction of the nanocrystalline phase in sample 2 was about one and a half times that in sample 1.

The surface magnetic properties of heterogeneous alloys were studied using a magnetooptical micromagnetometer described in detail elsewhere [13]. As is known, the magnetooptical Kerr effect is sensitive with respect to magnetization of the near-surface layer of a definite thickness corresponding to the so-called "light penetration depth" t_1. This layer thickness is determined by the formula $t_1 = \lambda/4\pi k$, where λ is the wavelength of the incident light and k is the absorption coefficient of the medium. According to the available experimental data [14], t_1 in metallic magnetic materials does not exceed 10–30 nm in the range of photon energies from 0.5 to 6 eV. In our case, the thickness of a probed near-surface layer was on the order of 20 nm. The surface hysteresis loops on both contact and free sides of the ribbon samples were measured using the equatorial (transverse) Kerr effect. The magnitude of this effect is

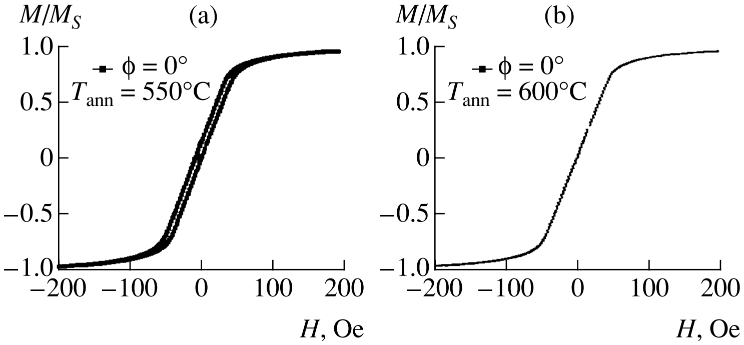

Fig. 1. The volume hysteresis loops observed in samples (a) 1 and (b) 2 in the magnetic field applied in the sample plane and oriented at an angle $\phi = 0°$ relative to the sample axis coinciding with the direction of melt spinning.

determined as $\delta = (I - I_0)/I_0$, where I and I_0 are the intensities of light reflected from the magnetized and nonmagnetized sample, respectively. In fact, we studied the behavior of the $\delta(H)/\delta_S \sim M(H)/M_S$ ratio (where δ_S is the value of the Kerr effect in the state of saturated magnetization and M_S is the saturation magnetization) in the course of cyclic variation of the magnetic field (from $+H$ to $-H$ and vice versa) applied in the plane parallel to the sample surface and perpendicular to the plane of light incidence. The anisotropy of magnetic properties was studied by rotating a sample around the normal to its surface. The angle between the direction along the ribbon length (the direction of spinning) and the orientation of magnetic field H is denoted by ϕ. The volume magnetic properties of samples were measured using a vibrating-sample magnetometer. All data presented below were obtained on round samples with a diameter of 6 mm cut from annealed ribbons, which eliminated the effect of shape anisotropy on the magnetic properties of samples.

Results and discussion. It was found that the aforementioned difference in the microstructure of samples 1 and 2 is accompanied by significant differences in their magnetic behavior. Data obtained using the vibrating-sample magnetometer showed that both samples possess a weak planar magnetic anisotropy and magnetically soft properties. Figure 1 shows the volume hysteresis loops observed in the field H oriented at $\phi = 0°$. As can be seen, the loops have a usual shape. The values of coercive force H_C^{vol} for samples 1 and 2 are 4.3 and 0.5 Oe, respectively. According to the random magnetic anisotropy model generalized so as to include the case of two-phase systems [12], an increase in the volume fraction of bcc Fe grains in sample 2 leads to a more effective intergranular interaction, which accounts for the decrease in the coercive force.

It was established that the surface magnetic properties substantially differ from the volume characteristics. The surface hysteresis loops measured in the magnetic fields oriented at $\phi = 0°$ and 90° are significantly different, which is evidence of a strong surface magnetic anisotropy (Fig. 2). No such anisotropy was observed in the initial sample. The surface coercive force H_C^{sur} is significantly higher than the volume value. In sample 2, H_C^{sur} is almost two orders of magnitude higher than H_C^{vol}. This fact can be explained by inhomogeneities in the microstructure and chemical composition in the surface layers of samples. The degree of inhomogeneity increases upon heat treatment, which is characteristic of materials prepared as described above [12, 13]. In addition, it was found that H_C^{sur} on the free side of the ribbon is smaller than that on the contact side. For example, on the free side of sample 2, $H_C^{\mathrm{sur}} = 12$ and 46 Oe for $\phi = 0°$ and 90°, respectively, while the corresponding values on the contact side are $H_C^{\mathrm{sur}} = 54$ and 76 Oe. This is explained by the difference in residual stresses developed on the two sides in the course of manufacture and heat treatment of an $Fe_{81}Nb_7B_{12}$ ribbon and by the difference between surface morphologies on the contact and free sides.

Of special importance is the unusual shape of the surface hysteresis loops (Fig. 2), which can be explained by inhomogeneous magnetic structure of the samples, in particular, by the coexistence of amorphous and nanocrystalline phases characterized by different values of magnetic anisotropy, saturation magnetization, and coercive force. It is a substantial result that the two-phase character of annealed $Fe_{81}Nb_7B_{12}$ alloy samples is manifested only in the behavior of their near-surface layers featuring most significant changes in microstructure as a result of annealing. The volume magnetic characteristics of both samples also change in accordance with their microstructure, but the shape of the hysteresis loop exhibits no significant variations (Fig. 1).

A more detailed analysis of the experimental data presented in Fig. 2 showed that the direct and reverse branches of the surface hysteresis loops measured for $\phi = 0°$ exchange places: negative residual magnetization is observed when the positive magnetic field decreases to zero and the magnetization reversal takes

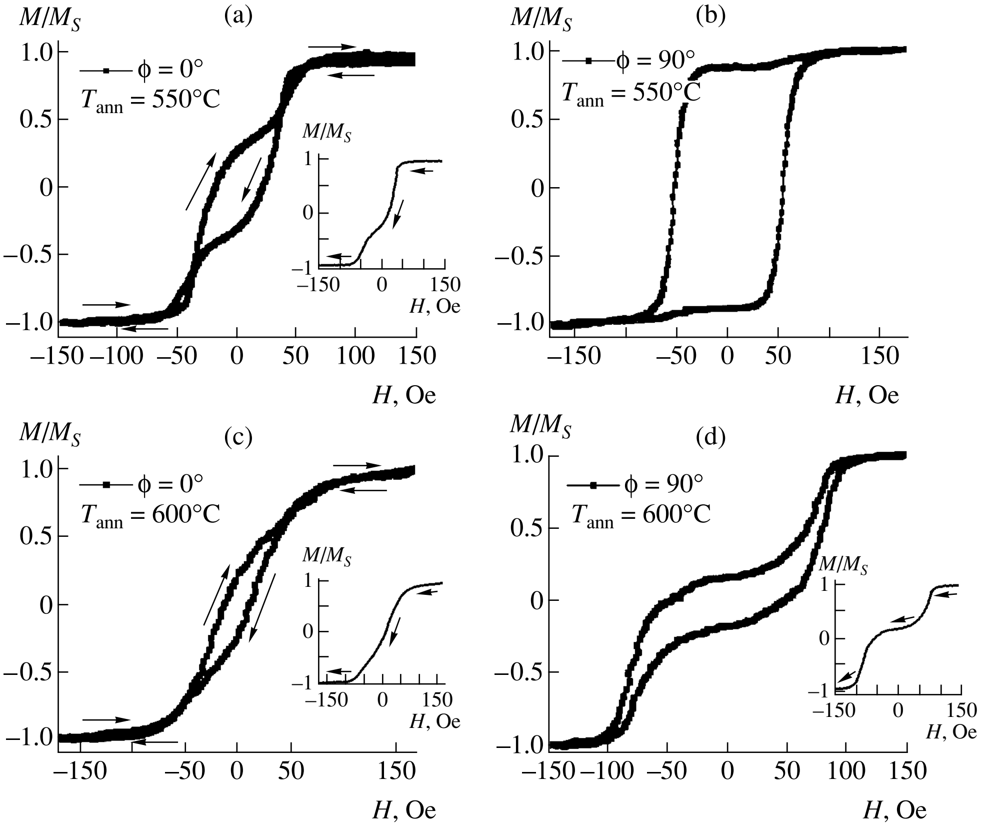

Fig. 2. The surface hysteresis loops observed for the free side of samples (a, b) 1 (annealed at 550°C) and (c, d) 2 (annealed at 600°C) in a magnetic field applied in the sample plane and oriented at an angle φ = 0° (a, c) and 90° (b, d). For the sake of clarity, the insets show the direct branches of the loops.

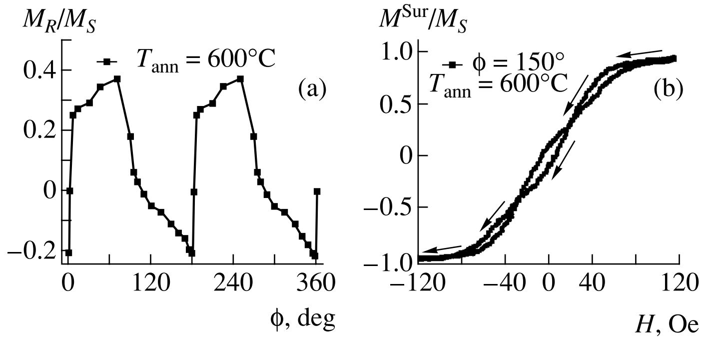

Fig. 3. Plots of (a) the reduced residual magnetization M_R/M_S versus the angle φ and (b) the partially inverted hysteresis loop observed at φ = 150° on the free side of the samples annealed at 600°C.

place at a positive value of the coercive force. This fact is clearly illustrated in the insets in Fig. 2, showing only one branch of the hysteresis loop (observed for the field varied from $+H$ to $-H$). According to the commonly accepted notions (see, e.g., [15]), such loops are referred to as inverted. It should be noted that the state with a negative value of the residual magnetization upon switching off the positive magnetic field is forbidden in homogeneous magnetic materials, where the magnetization is the order parameter in description of their thermodynamic state. According to Arrot [15], this effect can take place only in heterogeneous magnetic systems.

The results of measurements of the surface hysteresis loops for various orientations of the external magnetic field in the plane of a sample revealed unusual behavior of the residual magnetization as a function of the field orientation angle φ. For example, Fig. 3a shows the dependence of the reduced residual magnetization M_R/M_S on the φ value for the free side of sample 2. As can be seen, there is an interval of angles where M_R/M_S is negative. It was established that the surface hysteresis loops measured for such ϕ values are completely (Fig. 2) or partially (Fig. 3b) inverted. Analogous dependence of M_R/M_S on the angle ϕ was observed for sample 1. It should be noted that the initial amorphous $Fe_{81}Nb_7B_{12}$ alloy also exhibited a certain difference between the volume and surface hysteresis loops, but inverted loops were not observed.

The above experimental data can be qualitatively explained within the framework of a two-phase model according to which the heterogeneous alloys under consideration contain two dissimilar phases exhibiting uniaxial magnetic anisotropy and featuring antiferromagnetic exchange interaction. The total free energy of this system can be expressed as

$$\begin{aligned}E &= -M_1H\cos\varphi_1 - M_2H\cos\varphi_2 + K_1\sin^2(\varphi_1-\beta_1)\\ &\quad + K_2\sin^2(\varphi_2-\beta_2) + 2J_{12}M_1M_2\cos(\varphi_1-\varphi_2),\end{aligned} \quad (1)$$

where the first two terms represent the Zeeman magnetic energies of two phases with magnetizations M_1 and M_2; the third, fourth, and fifth terms describe the anisotropic energies of these phases and the exchange interaction between them (K_1 and K_2 are the constants of uniaxial magnetic anisotropy and J_{12} is the constant of antiferromagnetic exchange interaction); φ_1 and φ_2 are the angles between magnetization vectors $\mathbf{M}_1$ and $\mathbf{M}_2$ and the field direction; and β_1 and β_2 are the angles between magnetic anisotropy axes of the corresponding phases and the field direction (the magnetic field H is oriented in the sample plane). The magnetization of this system is given by the formula

$$M = M_1\cos\varphi_1 + M_2\cos\varphi_2. \quad (2)$$

The values of angles φ_1 and φ_2 as functions of the magnetic field H can be determined from the system of equations

$$\frac{\partial E}{\partial\varphi_1} = \frac{\partial E}{\partial\varphi_2} = 0. \quad (3)$$

Assuming that the anisotropic energies are much greater than the exchange interaction energy, $\beta_1 = \beta_2 = 0$, and $M_1 > M_2$ and taking into account the condition $\partial^2E/\partial(\varphi_1)^2 = \partial^2E/\partial(\varphi_2)^2 > 0$ determining stable solutions of Eqs. (3), we have calculated the hysteresis loop. It was found that the simplified two-phase model explains only partly inverted hysteresis loops. In order to obtain the completely inverted hysteresis, it is necessary to perform calculations without any simplifying assumptions, which meets considerable difficulties.

In conclusion, we have studied the surface and volume magnetic properties of heterogeneous (nanocrystalline/amorphous) $Fe_{81}Nb_7B_{12}$ alloys and revealed a strong influence of structural changes in annealed samples on their magnetic characteristics. Completely and partly inverted hysteresis loops were observed for the first time. The experimental results were qualitatively explained within the framework of a two-phase model, according to which the heterogeneous alloys contain two dissimilar phases characterized by uniaxial magnetic anisotropy and antiferromagnetic exchange interaction.

Acknowledgments. This study was supported by the Russian Foundation for Basic Research, project no. 02-02-16627.

REFERENCES

1. Y. Yoshizawa, S. Oguma, and K. Yamauchi, J. Appl. Phys. **64**, 6044 (1988).
2. K. Suzuki, A. Makino, A. Inoue, and T. Masumoto, J. Appl. Phys. **74**, 3316 (1993).
3. A. Makino, T. Hatanai, A. Inoue, and T. Masumoto, Mater. Sci. Eng. A **226–228**, 594 (1997).
4. K. Suzuki, A. Makino, A. Inoue, and T. Masumoto, J. Appl. Phys. **70**, 6232 (1991).
5. I. Škorvánek, J. Kováč, J. Marcin, *et al.*, J. Magn. Magn. Mater. **203**, 226 (1993).
6. M. Kopcewicz, A. Grabias, I. Škorvánek, *et al.*, J. Appl. Phys. **85**, 4427 (1999).
7. M. Miglierini, M. Kopcewicz, B. Idzikowski, *et al.*, J. Appl. Phys. **85**, 1014 (1999).
8. I. Škorvánek, C. G. Kim, J. Kováč, *et al.*, J. Magn. Magn. Mater. **215–216**, 440 (2000).
9. I. Škorvánek, S. Skwirblies, and J. Kötzler, Phys. Rev. B **64**, 184437 (2001).
10. I. Škorvánek, P. Švec, J. M. Grenéche, *et al.*, J. Phys.: Condens. Matter **14**, 4717 (2002).
11. E. E. Shalyguina, L. M. Bekoeva, and N. I. Tsidaeva, Sens. Actuators **81**, 216 (2000).
12. A. Hernando, M. Vasques, T. Kulik, and C. Prados, Phys. Rev. B **51**, 3581 (1995).
13. E. E. Shalyguina, V. V. Molokanov, and M. A. Komarova, Zh. Éksp. Teor. Fiz. **122**, 593 (2002) [JETP **95**, 511 (2002)].
14. E. E. Shalyguina and K. H. Shin, J. Magn. Magn. Mater. **220**, 167 (2000).
15. A. S. Arrot, in *Nanomagnetism*, Ed. by A. Hernando (Kluwer, Dordrecht, 1993), p. 73.

Translated by P. Pozdeev

Technical Physics Letters, Vol. 30, No. 7, 2004, pp. 595–597. Translated from Pis'ma v Zhurnal Tekhnicheskoĭ Fiziki, Vol. 30, No. 14, 2004, pp. 46–52.
Original Russian Text Copyright © 2004 by Kapliy, Prokaznikov, Rud'.

A Discrete Model of Adsorption with Three States

S. A. Kapliy, A. V. Prokaznikov, and N. A. Rud'
Yaroslavl State University, Yaroslavl, Russia
e-mail: rnrgio@yandex.ru

Received January 19, 2004

Abstract—A model of adsorption with recharge and allowance of the lateral interaction between molecules has been constructed within the framework of the theory of probabilistic cellular automata. Realization of this model reveals the organized behavior of the system with global synchronization of its parameters. The transition from turbulent (chaotic) to ordered regime passes through a state of local order involving the formation of leading centers (pacemakers). The appearance of self-organized behavior results from the development of intrinsic instability in the system. The process of ordering is related to the collective behavior of subsystems forming the whole system. *© 2004 MAIK "Nauka/Interperiodica".*

Investigations into the phenomenon of adsorption of various substances on the surface of solids have received much attention for a long time because the surface is the only channel for penetration into the bulk of a crystal [1]. In addition, modification of the surface properties significantly changes the behavior of solids, especially in the case of small grains, for which the roles of the surface and volume are comparable.

In the course of anodization of silicon semiconductor crystals in hydrofluoric acid under certain conditions, the dynamic characteristics of the process were found to exhibit periodic variations with time [2–5]. Analogous phenomena were observed in the experiments with porous-silicon-based electroluminescent devices [6] placed in a medium containing surfactants (usually, polar molecules) [7, 8]. A continuous model describing average values of the surface density of adsorbed molecules and the oscillation phenomena observed in the course of adsorption of surfactant molecules was recently developed in [8]. The model was mostly based on the physical notions developed previously [9] in the theoretical description of the kinetics of processes on the silicon surface during its plasmachemical etching with fluorine. In [9], we presented the energy diagrams of fluorine atoms (ions) adsorbed on silicon, formulated a system of kinetic equations, and obtained their solution for the process of silicon etching with atomic fluorine.

Within the framework of the developed model, it was demonstrated [8] that the system of equations describing the adsorption of molecules (atoms) on the surface can be reduced (provided that the adsorbed particles remain in the charged state) to a one-dimensional Van der Pol equation describing oscillations of a certain global averaged value (surface concentration of adsorbed molecules). A necessary condition for this reduction to the one-dimensional Van der Pol equation is the allowance for a lateral interaction between the adsorbed molecules (atoms), which leads to nonlinear current–voltage characteristics of the system with a region of negative differential conductivity [2–5].

This study is based on the model developed for the adsorption system described in detail in [8]. According to this model, the adsorbed atoms or molecules (in what follows, the adsorbed species will be referred to as adatoms) on a solid surface may occur in two states: neutral and charged due to the tunneling electron exchange between these adatoms and the solid [9]. We consider an elementary cell on the solid surface, which may occur in one of the three states: without adatom, with a neutral adatom, and with a charged adatom. The elementary cell can change its state, depending on the state of neighboring cells, thus being involved in the lateral interaction between adatoms. The proposed model is two-dimensional and is related to the solid surface assumed to be ideal, that is, free of defects and inhomogeneities.

The computer model developed in this study is based on the theory of probabilistic cellular automata. In contrast to the model of classical cellular automata described by Oono [10], our model is two-dimensional and belongs to the class of probabilistic cellular automata. The field of events on the solid surface is divided into elementary square cells, each occurring in one of the three states: empty (white or –1), occupied by a neutral adatom (gray or 0), and occupied by a charged adatom (black or +1). In order to take into account the lateral interaction between adatoms, the probability of a cell passing to one or another state is assumed to depend on the number of nearest neighbors occurring in

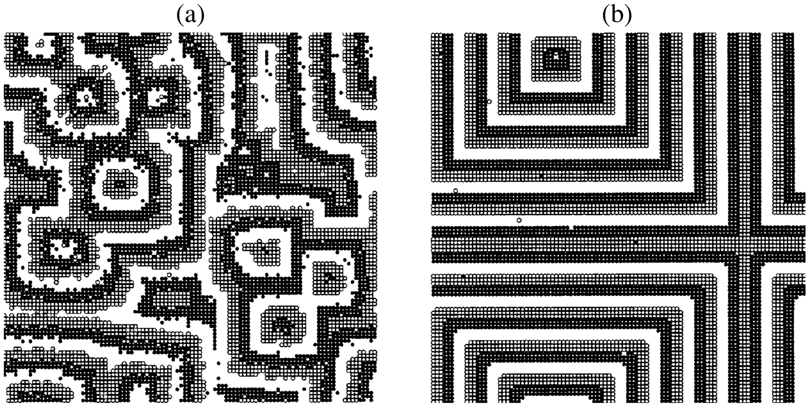

Fig. 1. Realizations of the model system with three states showing the patterns of phase waves propagating over the surface in the presence of several pacemakers possessing (a) nearly spherical and (b) square shape.

a certain state. The system evolves according to the following local transition rules:

$$X(i, j, t+1) = F(\overline{X}(i, j, t)), \tag{1}$$

$$\overline{X}(i, j, t) = \sum_{(k,l) \in O} \frac{X(k, l, t)}{N} + X(i, j, t), \tag{2}$$

where O denotes the nearest vicinity (usually, $|i - k| = 1$ and $|j - l| = 1$) of the central cell with the coordinates (i, j) and N is the number of cells in this vicinity (typically, $N = 8$). In our model, the rules of the passage to a new state are not limited by strict conditions (in contrast to the classical cellular automaton used, e.g., in [10, 11]) and involve the transition probabilities depending on the states of nearest neighbors $\overline{X}(i, j, t)$. Therefore, the $F(x)$ value in each subsequent step acquires certain values with the corresponding probabilities described by the transition probability matrix P_{ij},

$$F(x) = \begin{pmatrix} -1 \\ 0 \\ 1 \end{pmatrix}, \tag{3}$$

$$P_{ij} = \begin{pmatrix} w_{11} & w_{12} & w_{13} \\ w_{21} & w_{22} & w_{23} \\ w_{31} & w_{32} & w_{33} \end{pmatrix}, \tag{4}$$

provided that the x values fall within definite intervals $A_l' < x < A_l$. Here, $l = 1, 2$, or 3 is the number of possible states of the elementary cell and $A_l(A_l')$ is a certain number determined by the transition rules and related to the presence of a certain number of nearest neighbors in a definite state. The quantities w_{ij} are the probabilities of transitions between states i and j ($w_{13} = 0$ because an empty cell cannot pass to a state with charged adatom (ion)). Thus, $F(x)$ acquires the values –1, 0, +1 in accordance with the probabilities described by the matrix P_{ij}.

Realization of the relatively simple algorithm described above leads to a large number of various dynamical regimes, which can be classified according to the four main groups of cellular automata introduced by Wolfram [12]. In particular, the model describes periodic regimes differing by the oscillation periods and the characters of attaining stationary states. There also exists a region of turbulent (chaotic) behavior characterized by various types of the output parameters corresponding to numerous turbulent regimes. A characteristic feature of our model is the existence of regimes with leading centers (pacemakers) featuring different types of evolution.

The behavior of our model system in the presence of pacemakers exhibits a considerable variety. Figure 1a shows an "instantaneous" image of the system with several operating pacemakers interacting by means of waves of the soliton type traveling over the system. Figure 1b shows the system with pacemakers possessing a square symmetry. In a system of the type under consideration, this regime results from the competition of several pacemakers. With time, a pacemaker operating with the maximum frequency is retained; in this case, no instantaneous synchronization of various points in the space is observed.

Figure 2 shows the time variation of the number of black cells in different regimes. These curves can be obtained by varying the control parameters of the model. It should be noted that a phase diagram (analogous to that reported in [10]) for our system cannot be constructed, because there are several control parameters (rather than two as in [10]). The behavior of the model adsorption system with three states obeying the local transition rules (1) is richer than the behavior of averaged global characteristics described by the one-dimensional Van der Pol equation [8], which is related for the most part to the effective dimension of the sys-

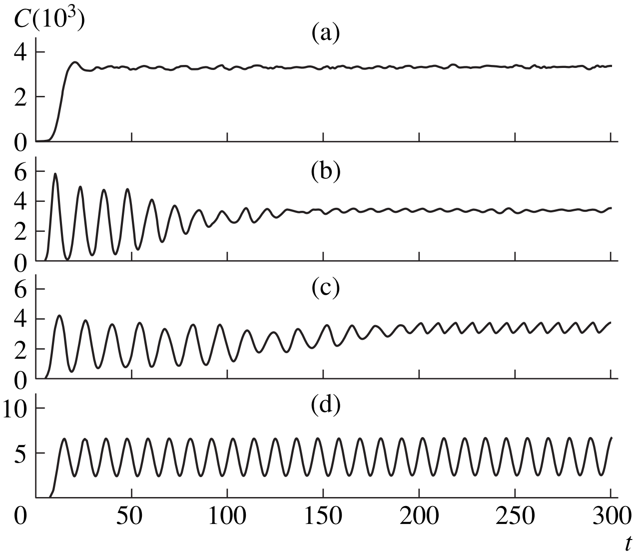

Fig. 2. Time variation of the number of black cells in different regimes of the model system (a) with chaotic dynamics, (b) with pacemakers of nearly spherical shape (soliton I), (c) with nearly square pacemakers (soliton II), and (d) with regular periodic dynamics.

tem. As is known, generalization of the one-dimensional Van der Pol equation to the three-dimensional case [13] leads to the appearance of solutions corresponding to stochastic (strange) attractors. The generalized equations describe an oscillator with inertial nonlinearity (Anishchenko–Astakhov oscillator) [13].

It is important to note that an analysis of the one-dimensional adsorption problem with two states for the probabilistic cellular automata does not lead to such a variety of solutions [14]. In particular, oscillating solutions and the solutions involving pacemakers are completely absent. It was pointed out [11] that an approach to determining local conditions under which a manifold of individual elements will reproduce a desired dynamics is still not developed.

Various structures observed in an oscillatory regime of pore formation experimentally studied in [15] could be identified with the result of operation of pacemakers possessing different configurations—both spherical and rectangular. The fronts of phase waves formed by the pacemakers of these two types travel in the radial directions and at right angles. As can be seen in Fig. 1, our model presented above also describes the pacemakers of both types observed in [15].

It should be noted that one of the most interesting conclusions from the results of this study is that the transition from chaos to global synchronization proceeds via local synchronization in the regime of pacemakers. This implies the formation of local oscillating centers with certain characteristic frequencies. The most convenient parameter characterizing various dynamical regimes of the system under consideration is the entropy of the dynamical system (Kolmogorov–Sinai entropy) related to the Lyapunov exponents [16]. This entropy reaches maximum in the regimes of chaotic oscillations, is zero in the regimes of regular oscillations, and acquires intermediate values in the regimes with pacemakers.

In conclusion, we have constructed and studied as two-dimensional model of a non-Hamiltonial system possessing all the characteristic properties of active media with self-organization. The results of our investigation can be used for prediction and interpretation of the operation of various sensor devices (see, e.g., [7, 8]).

Acknowledgments. The authors are grateful to Prof. H. Fell and Dr. J.K. Claussen (University of Kiel, Germany) for attracting their attention to the given problem.

REFERENCES

1. A. W. Adamson, *The Physical Chemistry of Surfaces* (Wiley, New York, 1976; Mir, Moscow, 1979).
2. F. Ozanam, J. N. Chazalviel, A. Radi, *et al.*, Phys. Chem. **95**, 98 (1991).
3. J. Carstensen, R. Prange, G. S. Poprikov, *et al.*, Appl. Phys. A **67**, 459 (1998).
4. R. L. Smith and S. D. Collins, J. Appl. Phys. **71** (8), R1 (1992).
5. É. Yu. Buchin and A. V. Prokaznikov, Pis’ma Zh. Tekh. Fiz. **23** (5), 1 (1997) [Tech. Phys. Lett. **23**, 169 (1997)].
6. Yu. E. Babanov, A. V. Prokaznikov, N. A. Rud’, *et al.*, Phys. Status Solidi A **162** (1), R7 (1997).
7. A. N. Laptev, A. V. Prokaznikov, and N. A. Rud’, Pis’ma Zh. Tekh. Fiz. **26** (23), 47 (2000) [Tech. Phys. Lett. **26**, 1049 (2000)].
8. A. N. Laptev, A. V. Prokaznikov, and N. A. Rud’, Mikrosistemnaya Tekh., No. 6, 31 (2002).
9. Yu. E. Babanov, A. V. Prokaznikov, and V. B. Svetovoy, Vacuum **41**, 902 (1990).
10. Y. Oono, Phys. Rev. Lett. **55**, 2927 (1985).
11. V. K. Vanag, Usp. Fiz. Nauk **169**, 481 (1999) [Phys. Usp. **42**, 413 (1999)].
12. S. Wolfram, Rev. Mod. Phys. **55**, 601 (1983).
13. V. S. Anishchenko, *Complex Oscillations in Simple Systems* (Nauka, Moscow, 1990) [in Russian].
14. H. Fuks, nlin.CG/0302015 (2003).
15. E. Yu. Buchin and A. V. Prokaznikov, Phys. Low-Dimens. Struct. **7–8**, 69 (2003).
16. G. Benettin, L. Galgani, and J. M. Strelcyn, Phys. Rev. A **14**, 2338 (1976).

Translated by P. Pozdeev

Technical Physics Letters, Vol. 30, No. 7, 2004, pp. 598–599. Translated from Pis'ma v Zhurnal Tekhnicheskoĭ Fiziki, Vol. 30, No. 14, 2004, pp. 53–55.
Original Russian Text Copyright © 2004 by Borodin, Trukhacheva.

Thermal Stability of Fullerenes

V. I. Borodin* and V. A. Trukhacheva
Petrozavodsk State University, Petrozavodsk, Karelia, Russia
** e-mail: borvi@karelia.ru*

Received January 14, 2004

Abstract—We have studied the thermal stability of fullerenes, for which there are discrepancies in available literature. A critical temperature of the thermal stability of C_{60} and C_{70} molecules was determined by thermodynamic calculations as a function of the pressure and the ratio of carbon to a buffer gas (helium or argon). *© 2004 MAIK “Nauka/Interperiodica”.*

The knowledge of the temperature interval of stability of C_{60} and C_{70} fullerenes is necessary both for the development of their production and purification technology and for their use in applications. Although this problem has been extensively studied, it is not possible to draw unambiguous conclusions from the available published data.

Eletskii *et al.* [1] with reference to Millican *et al.* [2] states that C_{60} molecule is stable in an inert (argon) atmosphere at temperatures up to ~1200 K. In other publications [3–5], with reference to the same paper of Kolodney *et al.* [6], it is ascertained that C_{60} retains thermal stability up to 1700 K. Some other papers indicate even higher maximum boundaries of thermal stability for fullerenes, for example, indicating that the decomposition of C_{60} and C_{70} molecules in the gas phase begins at 2650 and 2440 K, respectively ([7] with reference to [8]), or citing cases of anomalously high thermal stability of C_{60} molecules, losing their structure only on heating above 3000 K ([3] with reference to [9, 10]).

In order to evaluate the thermal stability of fullerenes, it is possible to use their thermodynamic characteristics. This Letter presents the results of thermodynamic calculations of the state of a mixture of carbon with an inert gas (argon or helium) based on sufficiently reliable thermodynamic data for C_{60} and C_{70} fullerenes [7]. Using these data and the program package ASTRA [11], we have calculated the composition of quasi-equilibrium (with neglect of a condensed carbon phase) gaseous system including first clusters of carbon, C_{60} fullerene molecules, and a buffer gas (argon or helium).

Figure 1 shows the typical results of thermodynamic calculations of the temperature dependence of the gas phase composition for the mixtures studied. As can be seen, the first clusters are more stable at elevated temperatures than C_{60} fullerene molecules. Nevertheless, C_{60} molecules remain stable in such mixtures even at high temperatures exceeding 3000 K. The results of our thermodynamic calculations showed that the upper boundary of the temperature interval of stability is not constant but depends on the parameters of the carbon mixture and a buffer gas. Figure 2 shows a plot of the temperature of stability of C_{60} versus the mass ratio of carbon to buffer gas (helium or argon) at various pressures. The temperature of stability was determined as the temperature at which 10% of the total fullerene content is subject to decomposition (i.e., at which the degree of dissociation is 0.1). As can be seen, the thermal stability of C_{60} fullerene in the carbon-inert gas mixture increases with the total carbon content in the mixture; under otherwise equal conditions, the thermal stability of C_{60} is higher in a mixture with argon than with helium.

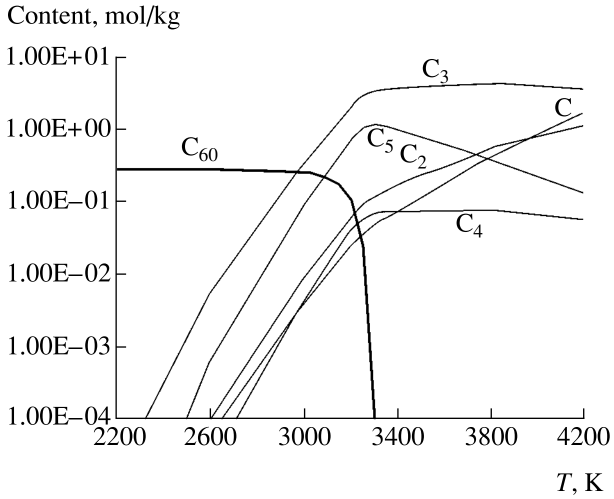

Fig. 1. The results of thermodynamic calculations of the quasi-equilibrium composition of a carbon–argon mixture at a pressure of $P = 0.1$ MPa and a carbon-to-argon mass ratio of 1 : 4.

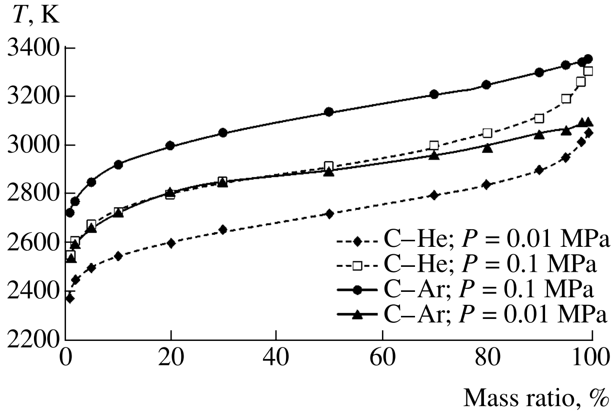

Fig. 2. A plot of the temperature of stability of C_{60} molecules versus carbon to inert gas (helium or argon) mass ratio in the mixture at various pressures.

The results of analogous calculations for fullerene C_{70} differ from the values for C_{60} to within several tens of degrees.

Acknowledgments. This study was supported by the “Plasma” Scientific Center.

REFERENCES

1. A. V. Eletskii and B. M. Smirnov, Usp. Fiz. Nauk **163** (2), 33 (1993) [Phys. Usp. **36**, 202 (1993)].
2. J. Millican *et al.*, Chem. Mater. **3**, 386 (1991).
3. A. V. Eletskii and B. M. Smirnov, Usp. Fiz. Nauk **165**, 977 (1995) [Phys. Usp. **38**, 935 (1995)].
4. G. N. Churilov, Prib. Tekh. Éksp., No. 1, 5 (2000).
5. L. N. Sidorov, Sorosovskiĭ Obrazovatel’nyĭ Zh., No. 3, 65 (1998).
6. E. Kolodney, B. Tsipinyuk, and A. Budrevich, J. Chem. Phys. **100**, 8542 (1994).
7. V. V. Dikiĭ and G. Ya. Kabo, Usp. Khim. **69**, 107 (2000).
8. T. Sommer, T. Kruse, and P. Roth, J. Phys. B **29**, 4955 (1996).
9. B. L. Zhang *et al.*, Phys. Rev. B **48**, 11381 (1993).
10. S. G. Kim and D. Tomanek, Phys. Rev. Lett. **72**, 2418 (1994).
11. *Low-Temperature Plasma*, Vol. 3: *Plasma Chemistry* (Nauka, Novosibirsk, 1991) [in Russian].

Translated by P. Pozdeev

Technical Physics Letters, Vol. 30, No. 7, 2004, pp. 600–602. Translated from Pis'ma v Zhurnal Tekhnicheskoĭ Fiziki, Vol. 30, No. 14, 2004, pp. 56–62.
Original Russian Text Copyright © 2004 by Aslanyan.

Linear *s*-Polarized Surface Waves in a Medium Inhomogeneous in One Dimension

L. S. Aslanyan
Yerevan State University, Yerevan, Armenia
e-mail: leon@ysu.am

Received December 2, 2003

Abstract—Linear *s*-polarized surface waves can exist at the boundary between an isotropic homogeneous medium and a medium inhomogeneous in one dimension (1D-inhomogeneous medium). This is related to deformation of the spatial envelope of the electric and magnetic components of the surface wave propagating in the 1D-inhomogeneous medium (in particular, in a plane-stratified medium). Such linear *s*-polarized surface waves can appear only provided that the refractive index of the inhomogeneous medium increases with the distance from the interface. © *2004 MAIK "Nauka/Interperiodica".*

Introduction. As is known, a sharp interface between two isotropic media may feature surface electromagnetic waves (SEWs) exponentially decaying with the distance from the interface. If both media are homogeneous, such waves may exist, provided that the permittivity of one medium is negative and the wave is *p*-polarized (i.e., the electric vector **E** occurs in the plane of incidence) [1].

In special cases, however, surface waves of other types can appear. In particular, D'yakonov showed [2] that a sharp interface between isotropic and anisotropic media admit some new types of surface waves existing due to the difference in the symmetry of these media, rather than due to the negative permittivity. It was also shown [3, 4] that nonlinearity of one of the contacting media makes possible the existence of *s*-polarized SEWs forbidden within the framework of linear optics. A special feature of the nonlinear problem is the conversion of the initially homogeneous medium into a medium inhomogeneous in one dimension (in the case of SEWs), whereby the parameters of the nonlinear medium depend on the intensity of propagating light. Therefore, analogous phenomena can be expected in the case when one of the contacting media is spatially inhomogeneous.

The effect of inhomogeneity on the character of SEW propagation was studied in [5–7] (see also [8]). Previously [9], it was shown that linear *s*-polarized SEWs can be excited at the interface between an isotropic medium and a medium inhomogeneous in one dimension (1D-inhomogeneous medium). Later, Monchicourt [10] reported on the registration of linear *s*-polarized SEWs at the interfaces in a granular medium, while Schwarzburg [8] derived a dispersion relation for SEWs in inhomogeneous plasma.

This study was aimed at the theoretical analysis of the conditions of existence and the wave characteristics of linear *s*-polarized surface waves appearing at the interface of two media, one of which is a plane-stratified medium.

Model calculations. Consider an *s*-polarized surface wave appearing at the interface of two isotropic media. Let the halfspace $z < 0$ be occupied by a homogeneous medium with the permittivity $\varepsilon_1 > 0$, and the halfspace $z > 0$, by a plane-stratified medium with a permittivity profile $\varepsilon_2(z) = \varepsilon_0 + az$, so that the xy plane coincides with the interface. Representing the surface wave in the form

$$E(x, z, t) = E(z)\exp[i(k_x x - \omega t)],$$

we obtain the equation

$$\frac{d^2E_j}{dz^2} - \left(k_x^2 - \frac{\omega^2}{C^2}\varepsilon_j(z)\right)E_j = 0, \qquad (1)$$

where $j = 1, 2$ is the number of the medium. Since the surface wave is *s*-polarized, the electric vector can be written as $\mathbf{E}_j = \{0, E_j, 0\}$. Introducing dimensionless variables

$$\xi = \frac{\omega}{c}z, \quad \eta_x = \frac{c}{\omega}k_x, \quad \varepsilon_2(\xi) = \varepsilon_0 + b\xi, \qquad (2)$$

where $b = (c/\omega)a$, we can rewrite Eq. (1) as

$$\frac{d^2E_j(\xi)}{d\xi^2} - (\eta_x^2 - \varepsilon_j(\xi))E_j(\xi) = 0. \qquad (3)$$

Assuming that the dielectric properties of the 1D-inhomogeneous medium vary in a slow manner, a solution

1063-7850/04/3007-0600$26.00 © 2004 MAIK "Nauka/Interperiodica"

to Eq. (3) in the Wentzel–Kramers–Brillouin (WKB) approximation has the following form:

$$\begin{aligned} E_2(\xi) &= \frac{A}{\sqrt[4]{\eta_x^2 - \varepsilon_2(\xi)}}\exp\left[-\int_0^{\xi}\sqrt{\eta_x^2 - \varepsilon_2(\xi)}\,d\xi\right] \\ &+ \frac{B}{\sqrt[4]{\eta_x^2 - \varepsilon_2(\xi)}}\exp\left[\int_0^{-\xi}\sqrt{\eta_x^2 - \varepsilon_2(\xi)}\,d\xi\right], \end{aligned} \tag{4}$$

where *A* and *B* are the amplitudes of the direct wave and the wave reflected from inhomogeneities, respectively. Substituting the expression for $\varepsilon_2(\xi)$ and integrating, we obtain

$$\begin{aligned} E_2(\xi) &= \frac{A}{\sqrt[4]{\eta_x^2 - \varepsilon_2(\xi)}}\exp[\varphi(\xi) - \varphi(0)] \\ &+ \frac{B}{\sqrt[4]{\eta_x^2 - \varepsilon_2(\xi)}}\exp[\varphi(0) - \varphi(\xi)], \end{aligned} \tag{5}$$

where $\varphi(\xi) = 2(\eta_x^2 - \varepsilon_0 - b\xi)^{3/2}/3b$. However, a solution within the framework of the first WKB approximation does not describe wave reflection from smooth inhomogeneity of the medium. This reflection can be adequately described, for example, using the Bremmer approximation of geometric optics [12].

Let us use an alternative approximate method. Denoting the primary wave amplitude at the interface by $A(\xi = 0) = A_0$, taking into account that the counterpropagating wave appears only due to the reflection from inhomogeneities, and using the Van der Pol method, we can write a solution to Eq. (3) in the following form:

$$\begin{aligned} E_2(\xi) &= \frac{A(\xi)}{\sqrt[4]{\eta_x^2 - \varepsilon_2(\xi)}}\exp[\varphi(\xi) - \varphi(0)] \\ &+ \frac{B(\xi)}{\sqrt[4]{\eta_x^2 - \varepsilon_2(\xi)}}\exp[\varphi(0) - \varphi(\xi)]. \end{aligned} \tag{6}$$

Since we use two variables, $A(\xi)$ and $B(\xi)$, instead of $E_2(\xi)$, we can introduce one arbitrary relationship between these variables. Let us assume that

$$\begin{aligned} &\left(\frac{A(\xi)}{\sqrt[4]{\eta_x^2 - \varepsilon_2(\xi)}}\right)'\exp[\varphi(\xi) - \varphi(0)] \\ &+ \left(\frac{B(\xi)}{\sqrt[4]{\eta_x^2 - \varepsilon_2(\xi)}}\right)'\exp[\varphi(0) - \varphi(\xi)] = 0. \end{aligned} \tag{6a}$$

Substituting expression (6) into Eq. (3) and taking into account additional condition (6a), we obtain a system of differential equations for determining the functions $A(\xi)$ and $B(\xi)$:

$$\left.\begin{aligned} B'(\xi) &= -\frac{A(\xi)}{4(\eta_x^2 - \varepsilon_2(\xi))}\varepsilon'(\xi)\exp[-2[\varphi(0) - \varphi(\xi)]] \\ A'(\xi) &= -\frac{B(\xi)}{4(\eta_x^2 - \varepsilon_2(\xi))}\varepsilon'(\xi)\exp[2[\varphi(0) - \varphi(\xi)]] \end{aligned}\right\}. \tag{7}$$

Note that Eqs. (7) are exact. For a weak inhomogeneity, whereby ε' is small compared to ε, $A(\xi)$ and $B(\xi)$ are slowly varying functions. In the zero-order approximation for $A(\xi)$, we can assume that $\varepsilon' = 0$ and $A(\xi) = A_0$. Then, $B(\xi)$ is obtained by integration as

$$B(\xi) = -A_0 b\int\frac{\exp[-2[\varphi(0) - \varphi(\xi)]]}{4(\eta_x^2 - \varepsilon_0 - b\xi)}d\xi, \tag{8}$$

where the integration constant is taken equal to zero because we consider the surface wave. Integral (8) can be expressed in terms of the integral exponential function $E_i(\xi)$. A simpler expression is obtained taking into account the smallness of parameter *b* and expanding the integrand in (8) into a series with respect to this parameter. To within the terms $0(b^2)$, we obtain

$$B(\xi) = -\frac{A_0 b}{8(\eta_x^2 - \varepsilon_0)^{3/2}}\exp[-2\sqrt{\eta_x^2 - \varepsilon_0}\,\xi]. \tag{9}$$

Using analogous expansion in Eq. (6) and substituting expression (9), we eventually arrive at the following expression:

$$\begin{aligned} E_2(\xi) &= \frac{A_0}{\sqrt[4]{\eta_x^2 - \varepsilon_2}}\left\{1 + \frac{b}{8(\eta_x^2 - \varepsilon_0)^{3/2}} + \frac{b}{4(\eta_x^2 - \varepsilon_0)}\xi\right. \\ &\left. + \frac{b}{4(\eta_x^2 - \varepsilon_0)^{1/2}}\xi^2\right\}\exp[-\sqrt{\eta_x^2 - \varepsilon_0}\,\xi]. \end{aligned} \tag{10}$$

This is a solution of Eq. (3) in the inhomogeneous medium ($j = 2$) under consideration. In the homogeneous medium ($j = 1$), the solution is

$$E_1(\xi) = D\exp[k_1\xi], \tag{11}$$

where $k_1 = \sqrt{\eta_x^2 - \varepsilon_1}$ and *D* is the surface wave amplitude in the first medium. The condition of existence (or the dispersion relation) for this surface wave is obtained by imposing the following boundary conditions on the solutions (10) and (11):

$$\left.\begin{aligned} E_1(\xi = 0) &= E_2(\xi = 0) \\ \frac{dE_1}{d\xi}(\xi = 0) &= \frac{dE_2}{d\xi}(\xi = 0) \end{aligned}\right\}. \tag{12}$$

Using relations (10)–(12), we obtain the following

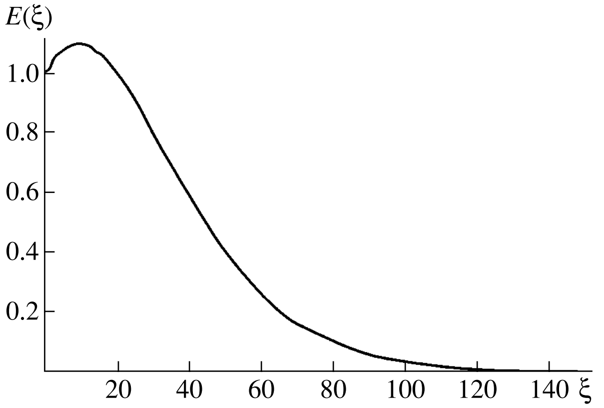

Normalized electric field structure in the inhomogeneous medium.

dispersion relation:

$$\sqrt{\eta_x^2-\varepsilon_1}+\sqrt{\eta_x^2-\varepsilon_0} = \frac{b}{4(\eta_x^2-\varepsilon_0)}. \quad (13)$$

Let us obtain some numerical estimates, assuming that the first medium is a glass with a refractive index of $n = 1.57$ and the second medium is a hybrid oriented liquid crystal (e.g., MBBA) with a thickness of 10 μm ($\varepsilon_{\|} = 3.24$ and $\varepsilon_{\perp} = 2.46$ for $\lambda = 0.53$ μm). This cell can be considered to a good approximation as a plane-stratified medium with $b = 0.05$. The shape of the wave (10) depicted in the figure exhibits an interesting feature: the maximum of the field intensity is localized inside the inhomogeneous layer rather than at the interface. Therefore, similar to the case of a nonlinear medium [13], the excitation of a linear *s*-polarized surface wave is possible only provided that $E_2(\xi)$ increases with the distance from the interface (the maximum intensity is reached at a distance on the order of the wavelength) but eventually vanishes at infinity. This condition can be satisfied with a plane-stratified medium with $b > 0$. Using a graphical solution of Eq. (3), we can determine the wave vector for the surface wave under consideration (for the above parameters, $\eta_x = 1.573$).

Conclusions. According to the results of analysis, linear *s*-polarized surface waves can exist at the boundary between an isotropic homogeneous dielectric medium and a plane-stratified medium. This is related to deformation of the spatial envelope of the electric and magnetic components of the surface wave propagating in the medium inhomogeneous in one dimension (in particular, in a plane-stratified medium). Such linear *s*-polarized surface waves can appear only provided that the refractive index of the inhomogeneous medium increases with the distance from the interface ($b > 0$).

Acknowledgments. The author is grateful to Yu.S. Chilingaryan for fruitful discussions.

This study was supported by the Government of the Republic of Armenia (project no. 1073).

REFERENCES

1. V. M. Agranovich and D. L. Mills, Surface Polaritons, in: *Electromagnetic Waves at Surfaces and Interfaces*, Ed. by V. M. Agranovich and D. L. Mills (North-Holland, Amsterdam, 1982; Nauka, Moscow, 1985).
2. M. I. D’yakonov, Zh. Éksp. Teor. Fiz. **94** (3), 118 (1988) [Sov. Phys. JETP **67**, 714 (1988)].
3. W. J. Tomlinson, Opt. Lett. **5** (7), 323 (1980).
4. W. Chen and A. A. Maradudin, J. Opt. Soc. Am. B: Opt. Phys. **5** (2), 529 (1988).
5. E. M. Conwell, Phys. Rev. B: Condens. Matter. **11**, 1508 (1975).
6. L. S. Aslanyan, N. N. Badalyan, A. A. Petrosyan, and Yu. S. Chilingaryan, Opt. Spektrosk. **63** (5), 1080 (1987) [Opt. Spectrosc. **63**, 637 (1987)].
7. L. S. Aslanyan, N. N. Badalyan, A. A. Petrosyan, and Yu. S. Chilingaryan, Izv. Akad. Nauk ArmSSR, Fiz. **23** (5), 265 (1988).
8. F. B. Schwarzburg, Usp. Fiz. Nauk **170** (12), 1297 (2000) [Phys. Usp. **43**, 120 (2000)].
9. L. S. Aslanyan, Uch. Zap. Yerevan. Gos. Univ., No. 1, 52 (1992).
10. P. I. Monchicourt, J. Phys.: Condens. Matter **9**, 5765 (1997).
11. M. I. Rabinovich and D. I. Trubetskov, *Introduction to the Theory of Oscillations and Waves* (Nauka, Moscow, 1984).
12. L. M. Brekhovskikh, *Waves in Layered Media* (Nauka, Moscow, 1973; Academic, New York, 1960).
13. A. C. Newell and I. V. Moloney, *Nonlinear Optics* (Addison Wesley, 1992), p. 432.

Translated by P. Pozdeev

Technical Physics Letters, Vol. 30, No. 7, 2004, pp. 603–604. Translated from Pis'ma v Zhurnal Tekhnicheskoĭ Fiziki, Vol. 30, No. 14, 2004, pp. 63–67.
Original Russian Text Copyright © 2004 by Remnev, Pushkarev, Furman.

Matching a Double Forming Line to Explosive-Emission Diode

G. E. Remnev, A. I. Pushkarev*, and É. G. Furman
Institute of High Voltage Research, Tomsk Polytechnic University, Tomsk, Russia
** e-mail: aipush@mail.ru*

Received October 13, 2003; in final form, February 17, 2004

Abstract—The regime of operation of an explosive-emission diode is affected by a matching transformer between this diode and a double forming line of a high-current electron accelerator. Preliminary forced demagnetization of the transformer core makes the shape of the voltage pulse applied to the cathode close to the optimum, corresponding to a decrease in the resistance of the anode–cathode gap related to expansion of the explosive-emission plasma. In addition, matching of the double forming line to the explosive-emission diode significantly decreases the amplitude of parasitic prepulses and increases (to 90–92%) the fraction of energy supplied to the diode during the main current pulse. *© 2004 MAIK "Nauka/Interperiodica".*

Pulsed electron accelerators producing electron bunches with energies above 100 keV usually employ explosive-emission cathodes [1]. In accelerators with a power exceeding 1 kW, it is important to provide for the optimum matching between all units in order to avoid energy losses and increase the working life of the accelerator. During the formation of pulsed electron beams with pulse energies above several tens of joules, the most energy-stressed unit is the explosive-emission diode. It is necessary not only to match the resistance of the anode–cathode gap to the wave impedance of a nanosecond oscillator by the moment of application of a high-voltage pulse but also to take into account a decrease in the resistance of the anode–cathode gap related to expansion of the explosive-emission plasma in the gap.

Recently [2], it was demonstrated for an explosive-emission diode with flat electrodes and the current–voltage characteristic described by the Child–Langmuir relation that the optimum shape of the voltage pulse taking into account the gap reduction as a result of the plasma expansion is described by the formula

$$U(t) = U_0\left(1 - \frac{4vt}{d}\right), \tag{1}$$

where U_0 is the initial voltage, v is the cathode plasma velocity, and d is the anode–cathode distance. Formula (1) describes a triangular pulse with the voltage fall rate

$$k = \frac{4v}{d}. \tag{2}$$

In order to increase the efficiency of a nanosecond high-current accelerator and the working life of its output window, we used a matching transformed between the explosive-emission diode and a water-filled double forming line. The transformer was analogous to the inductor described in [3] but was operated with forced demagnetization of the core in the course of pulse formation, which allowed the voltage applied to the forming line and the Arkadiev–Marx oscillator to be reduced by half and a parasitic prepulse to be suppressed without using a sharpening discharge gap. The accelerator generated pulsed electron beams with a pulse energy of 180–200 J, an electron energy of 500 keV, and full width at half maximum (FWHM) of 60 ns. The accelerator had the classical design comprising an Arkadiev–Marx oscillator, a double forming line, and a planar vacuum diode with a 60-mm-diam graphite explosive-emission cathode.

The gas-filled pulsed voltage oscillator according to the Arkadiev–Marx scheme contained seven capacitor steps, each step comprising a pair of K75-74 capacitors (0.047 μF, 40 kV). The first step had a controlled discharge gap initiated by a trigatron. The water-filled forming line had an electrical length of 30 ns and an arm capacitor of $C_1 = C_2 = 6.5 \times 10^{-9}$ F and a total capacitance equal to the output capacitance of the pulsed voltage generator. The forming line was commutated by a gas-filled discharger with a gap width of 11 mm and a technical-purity nitrogen pressure of up to 8 bar. The matching transformer was immersed in oil. The transformer had four K360 × 150 × 25 cores made of 50NP-0.01 alloy, with 12 turns (uniformly spaced in azimuth) soldered to electrodes of the double forming line. An additional turn formed by the cathode holder and the case of the accelerator chamber was connected to the coils of the matching transformer (i.e., the anode–cathode gap). Thus, the diode is connected according to the autotransformer scheme with voltage doubling relative to the output voltage of the double forming line.

In order to reduce the prepulse amplitude and optimize the shape of the main voltage pulse formed by the nanosecond oscillator, we used the method of forced demagnetization of the transformer core, which provides for the saturated state of the ferromagnetic steel core. The design of the electron accelerator with the matching transformer and the forced demagnetization unit, as well as the system operation in the regime with

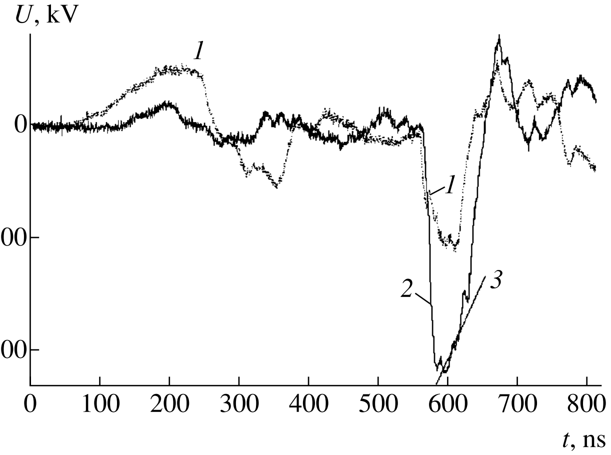

Fig. 1. Typical oscillograms of the voltage applied to the explosive-emission diode operating in the regimes (*1*) without and (*2*) with forced demagnetization of the matching transformer core. Line *3* shows the pulse slope determining the voltage fall rate.

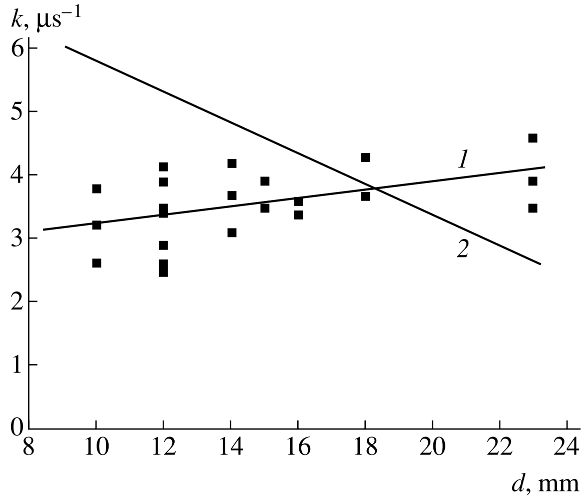

Fig. 2. Plot of (*1*) the diode voltage fall rate and (*2*) the optimum voltage fall rate versus the anode-cathode gap width in a diode with graphite explosive-emission cathode.

preliminary demagnetization of the ferromagnetic core of the matching transformer, were considered in detail elsewhere [4, 5].

Figure 1 shows the typical oscillograms of the voltage applied to the anode–cathode gap in two regimes with the same charging voltage in the forming line. As can be seen, preliminary demagnetization of the ferromagnetic core (curve *2*) allowed the amplitude of the main pulse to be doubled, the prepulse amplitude to be reduced from 50 to 5%, and the pulse shape to be optimized. Use of forced demagnetization increased the working life of the output foil up to 10^4 pulses (foil breakage was caused in most cases by malfunction of the demagnetization scheme).

The shape of the voltage pulse generated by the forming line with the matching transformer in the regime of forced demagnetization was close to that described by relation (1) in a broad range of the anode–cathode gap widths. Figure 2 shows a plot of the diode voltage fall rate versus the gap width. The voltage fall rate was calculated by the formula

$$k = \frac{1}{U_m}\frac{dU(t)}{dt}, \qquad (3)$$

where U_m is the maximum voltage.

For comparison, Fig. 2 also shows a plot of the optimum voltage fall rate (line *2*) calculated using formula (2) assuming the graphite cathode plasma to expand at a velocity of 1.5×10^6 cm/s [2, 6]. As can be seen, the shape (fall rate) of the diode voltage for an anode–cathode gap width of 17–19 mm coincides with the optimum, thus providing for the matching of the nanosecond oscillator with the explosive-emission diode during the voltage pulse. The diode voltage fall during the pulse is related to the magnetization current pulse in the ferromagnetic core, the shape of which is close to triangular.

The results of our investigation showed that matching of the explosive-emission diode to the forming line by means of the step-up transformer ensures that 92–95% of the energy supplied to the diode to be consumed during the main pulse (provided forced demagnetization of the transformer core). In the case of operation without preliminary demagnetization, no more than 75% of the energy stored in the forming line is spent for the main pulse formation. Analogous measurements were performed for the same accelerator with the double forming line loaded on the diode via a sharpening discharge gap without matching transformer (i.e., by the scheme analogous to that used in accelerators of the TEMP type [7]). The results showed that only 60–70% of the energy stored in the forming line is spent for the main pulse formation. The remaining energy is spent for the generation of parasitic prepulse (4–5%) and afterpulses.

REFERENCES

1. G. A. Mesyats, *Generation of High-Power Nanosecond Pulses* (Sov. Radio, Moscow, 1974).
2. G. A. Mesyats, Pis'ma Zh. Tekh. Fiz. **28** (13), 36 (2002) [Tech. Phys. Lett. **28**, 550 (2002)].
3. V. M. Bystritskiĭ, I. B. Ivanov, Ya. E. Krasik, *et al.*, Prib. Tekh. Éksp., No. 5, 122 (1987).
4. G. E. Remnev, É. G. Furman, A. I. Pushkarev, *et al.*, Prib. Tekh. Éksp., No. 2 (2004) (in press).
5. G. Remnev, E. Furman, A. Pushkarev, *et al.*, in *Proceedings of the 4th International Symposium on Pulsed Power and Plasma Applications, Nagaoka, 2003*, pp. 172–175.
6. A. S. Bugaev, V. I. Gushenets, A. A. Nikolaev, *et al.*, Zh. Tekh. Fiz. **70** (9), 37 (2000) [Tech. Phys. **45**, 1135 (2000)].
7. G. E. Remnev, I. F. Isakov, M. S. Opekunov, *et al.*, Izv. Vyssh. Uchebn. Zaved. Fiz., No. 4 (Suppl.), 92 (1998).

Translated by P. Pozdeev

Technical Physics Letters, Vol. 30, No. 7, 2004, pp. 605–608. Translated from Pis'ma v Zhurnal Tekhnicheskoĭ Fiziki, Vol. 30, No. 14, 2004, pp. 68–74.
Original Russian Text Copyright © 2004 by Tyukhtin.

Radiation of a Charge Moving in a Waveguide Filled with a Dielectric Medium Possessing Resonance Dispersion

A. V. Tyukhtin
Institute of Radiophysics, St. Petersburg State University, St. Petersburg, Russia
e-mail: tyukhtin@niirf.spbu.ru

Received January 20, 2004

Abstract—The radiation of a point charged particle moving along the axis of a round waveguide filled with a dielectric medium possessing resonance dispersion is theoretically studied. It is shown that the dispersion significantly influences the frequencies of excited harmonic modes and the energy of radiation. Allowance for dispersion leads to suppression of all excited harmonics to an extent increasing with the order of harmonics. *© 2004 MAIK "Nauka/Interperiodica".*

The radiation of charged particles moving in waveguide structures has been extensively studied for a long time (see, e.g., [1–6]). This direction of research is still of importance, in particular, in the context of development of particle accelerators employing wake fields [4–6]. It should be noted that previous investigations of these phenomena did not take into account the effect of dispersion characteristics of a medium on the radiation process. However, an analysis of such problems in the case of infinite media showed that a dispersion of the resonance type (characteristic of dielectrics) substantially affects parameters of the Vavilov–Cherenkov radiation [7, 8]. Apparently, we may expect that such dispersion will also significantly influence the radiation of a particle moving in a bounded dispersive medium.

This study is devoted to an analysis of the role of a resonance dispersion in the problem of radiation of a point charge q moving at a constant velocity $v = c\beta$ along the z axis of a round waveguide with the ideal conducting wall. The waveguide is assumed to be filled with a homogeneous, isotropic nonabsorbing dielectric medium.

Let us use general expressions for the frequencies of excited modes and the radiation energy (see, e.g., review [1]). The frequencies are given by the formula

$$\omega_m = \frac{v\chi_m}{a\sqrt{n^2\beta^2 - 1}}, \tag{1}$$

where a is the waveguide radius, $n = \sqrt{\varepsilon\mu}$ is the refractive index of the medium, and χ_m are the roots of the zero-order Bessel function ($J_0(\chi_m) = 0$). In the presence of dispersion, relation (1) with $n(\omega_m)$ on the right-hand side becomes the equation for determining frequencies.

The radiation energy per unit pathlength of the charged particle can be written as

$$W = \sum_m W_m = \frac{2q^2}{a^2}\sum_m \frac{1}{\varepsilon_m[J_1(\chi_m)]^2(1+\delta_m)}, \tag{2}$$

where

$$\delta_m = \frac{\omega\beta^2}{2(n^2\beta^2 - 1)}\frac{dn^2}{d\omega}\bigg|_{\omega = \omega_m}, \tag{3}$$

and the sum is taken over all harmonics obeying the condition $n_m^2\beta^2 > 1$. It should be recalled that $W = -qE_z^{(0)}$, where $E_z^{(0)}$ is the longitudinal component of the electric field vector at the point where the charge is situated [1].

We will consider the case of a medium with the permittivity

$$\varepsilon = 1 + \frac{\omega_L^2}{\omega_r^2 - \omega^2} = \frac{\omega_r^2\varepsilon_0 - \omega^2}{\omega_r^2 - \omega^2}, \tag{4}$$

where ω_r and ω_L are the resonance and Langmuir frequencies, respectively, and $\varepsilon_0 = 1 + \omega_L^2/\omega_r^2$ is the permittivity at a zero frequency (in a constant field). The magnetic permeability μ of the medium is assumed to be unity. Formula (4) describes the medium with a resonance dispersion and negligibly small conductivity. The radiation of a charge moving in an infinite medium with such dispersion was studied by Afanasiev *et al.* [7, 8].

In accordance with the condition $\varepsilon(\omega)\beta^2 > 1$, the frequencies of radiated waves fall within the interval $\omega_c < \omega < \omega_0$, where $\omega_c = \omega_0\sqrt{(1-\varepsilon_0\beta^2)(1-\beta^2)^{-1}}$ for $\varepsilon_0\beta^2 < 1$ and $\omega_c = 0$ for $\varepsilon_0\beta^2 > 1$. Substituting expression (4) into Eq. (1) and solving the equation, we obtain

$$\omega_m = \frac{\omega_r}{\tilde{a}\sqrt{2(1-\beta^2)}}\sqrt{\tilde{a}^2 - \beta^2(\varepsilon_0\tilde{a}^2 + \chi_m^2) + \sqrt{[\tilde{a}^2 - \beta^2(\varepsilon_0\tilde{a}^2 + \chi_m^2)]^2 + 4\beta^2\tilde{a}^2\chi_m^2(1-\beta^2)}}, \tag{5}$$

where $\tilde{a} = a\omega_r/c$. It can be readily shown that the harmonic mode frequency monotonically increases with its number and tends to the resonance frequency ω_r as $m \longrightarrow \infty$. The difference between adjacent harmonics $\omega_{m+1} - \omega_m$ decreases with increasing m and tends to zero as $m \longrightarrow \infty$. Using relations (3) and (4), the quantity δ_m in formula (2) can be expressed as

$$\begin{aligned}\delta_m &= \frac{(\varepsilon_0 - 1)\beta^2\omega_r^2\omega_m^2}{(\omega_r^2 - \omega_m^2)[\omega_m^2(1-\beta^2) + \omega_r^2(\varepsilon_0\beta^2 - 1)]} \\ &= \frac{\tilde{a}^2(\varepsilon_0 - 1)}{\chi_m^2}\left(\frac{\omega_m^2}{\omega_r^2 - \omega_m^2}\right)^2.\end{aligned} \tag{6}$$

Let us separately consider the important partial case of an ultrarelativistic charged particle, which corresponds to $1 - \beta \ll 1$. In this case, expression (5) reduces to

$$\omega_m \approx \frac{\omega_r\chi_m}{\sqrt{\tilde{a}^2(\varepsilon_0 - 1) + \chi_m^2}}. \tag{7}$$

Under the condition $\tilde{a}^2(\varepsilon_0 - 1) \ll \chi_m^2$, the harmonic frequency is close to the resonance frequency ω_r. In the case of a "thin" waveguide such that $\tilde{a}^2(\varepsilon_0 - 1) \ll 1$, the frequencies of all excited modes will be close to the resonance frequency. If the waveguide is not thin (in this sense), the frequencies of several first harmonics will substantially differ from ω_r, but the harmonics of sufficiently high orders will have frequencies close to ω_r.

It is interesting to compare the frequencies given by formula (7) to those for a nondispersive medium. According to Eq. (1) with $v \approx c$, the harmonic frequencies in the latter case are $\omega_m^{(c)} \approx c\chi_m/(a\sqrt{\varepsilon_c - 1})$, where ε_c is the permittivity of the nondispersive medium (the magnetic permeability is still assumed to be $\mu = 1$). Thus, the ratio of frequencies in the two cases is

$$\frac{\omega_m}{\omega_m^{(c)}} = \frac{\tilde{a}\sqrt{\varepsilon_c - 1}}{\sqrt{\tilde{a}^2(\varepsilon_0 - 1) + \chi_m^2}}. \tag{8}$$

For $\varepsilon_c = \varepsilon_0$, the ratio substantially differs from unity even for the first mode; the difference increases with the mode number. If the permittivity of the nondispersive medium is equal to that of the dispersive medium at the first mode frequency, $\varepsilon_c = \varepsilon(\omega_1) = \varepsilon_0 + \chi_m^2\tilde{a}^{-2}$, the first harmonic frequencies are equal but the others are different and the difference grows with the mode number.

For the quantity δ_m in the ultrarelativistic case, we have

$$\delta_m \approx \frac{\chi_m^2}{\tilde{a}^2(\varepsilon_0 - 1)} = \frac{\omega_m^2}{\omega_r^2 - \omega_m^2}. \tag{9}$$

The energy of the mth harmonic according to formula (2) is

$$\begin{aligned}W_m &\approx \frac{2q^2}{a^2}\frac{\tilde{a}^4(\varepsilon_0 - 1)}{(\varepsilon_0\tilde{a}^2 + \chi_m^2)[(\varepsilon_0 - 1)\tilde{a}^2 + \chi_m^2][J_1(\chi_m)]^2} \\ &= \frac{2q^2}{a^2}\frac{(\omega_r^2 - \omega_m^2)^2}{\omega_r^2(\varepsilon_0\omega_r^2 - \omega_m^2)[J_1(\chi_m)]^2}.\end{aligned} \tag{10}$$

In the nondispersive medium, this expression simplifies to

$$W_m^{(c)} = \frac{2q^2}{a^2}\frac{1}{\varepsilon_c[J_1(\chi_m)]^2}. \tag{11}$$

It should be noted that the series $\Sigma W_m^{(c)}$ diverges, which is a manifestation of the well-known "energy paradox" in the theory of radiation of a charge moving in the nondispersive medium. By analogy with the case of the infinite medium, the problem is solved by making allowance for the dispersion: the series ΣW_m converges since the terms with large numbers are on the order of $\chi_m^{-3} \sim m^{-3}$ (see the first equality in expression (10)).

The ratio of energies of the mth harmonic excited in the media with and without dispersion in the case of $\beta \approx 1$ is

$$\frac{W_m}{W_m^{(c)}} \approx \varepsilon_c\frac{(\omega_r^2 - \omega_m^2)^2}{\omega_r^2(\varepsilon_0\omega_r^2 - \omega_m^2)} = \frac{\varepsilon_c}{\varepsilon_m}\left(1 - \frac{\omega_m^2}{\omega_r^2}\right), \tag{12}$$

where $\varepsilon_m = \varepsilon(\omega_m)$. As can be seen, even for $\varepsilon_c = \varepsilon_1$, the radiation energy for any mode in the medium with dispersion is lower than that in the nondispersive medium. This difference holds for all harmonics including the first mode. For the first harmonics, the difference is related to the fact that the radiation energy depends not only on the permittivity but on its derivative as well. As can be seen from formulas (2) and (3), the radiation energy in the region of normal dispersion (where $dn^2/d\omega > 0$) is always smaller than that in the nondispersive medium (provided that the refractive indices at the given frequencies are equal). As the mode number increases, ratio (12) decreases for two reasons: (i) because ε_m grows and (ii) because the frequency ω_m tends to the resonance value.

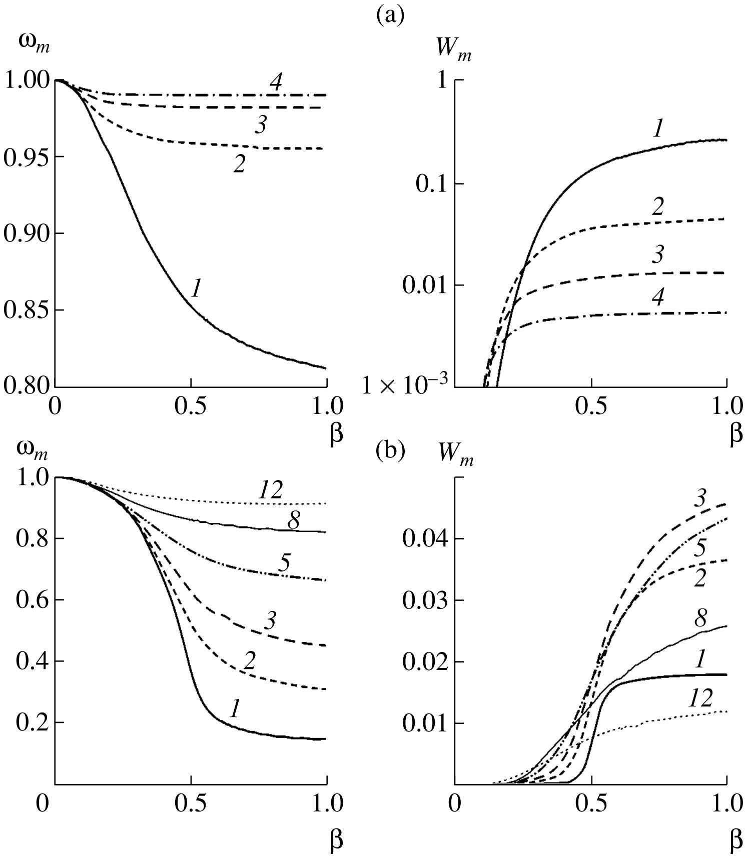

Fig. 1. Plots of the frequencies ω_m and energies W_m versus the charge velocity β for $\varepsilon_0 = 4$ at (a) $\tilde{a} = 1$ and (b) $\tilde{a} = 10$. The frequencies are expressed in the units of ω_r, and the energies W_m are expressed in the units of $q^2\omega_r^2c^{-2}$.

Let us consider the dependence of the energy W_m spent for the excitation of one harmonic on the mode number m. According to formula (11) the W_m value in the medium without dispersion increases with m. In a dispersive medium, the situation is substantially different. For $\varepsilon_0\tilde{a}^2 \ll 1$ (thin waveguide), we have $W_m \sim \chi_m^{-4}[J_1(\chi_m)]^{-2}$ for any harmonic and the energy exhibits a rapid and monotonic decrease with increasing mode number m. For $(\varepsilon_0 - 1)\tilde{a}^2 \gg 1$ ("thick" waveguide), the condition $(\varepsilon_0 - 1)\tilde{a}^2 \gg \chi_m^2$ is valid for not very large m. This implies that $W_m \sim [J_1(\chi_m)]^{-2}$ and the energy increases with the mode number. However, for sufficiently large m, $\varepsilon_0\tilde{a}^2 \ll \chi_m^2$ and the energy decreases with increasing mode number according to the same law as in the case of thin waveguide.

Figure 1 shows the mode frequencies and energies as functions of the charged particle velocity for $\varepsilon_0 = 4$ and two values of the dimensionless radius $\tilde{a}$. It should be emphasized that the absolute value of the resonance frequency is insignificant since the frequencies are expressed in ω_r units, and the energies, in the units of $q^2\omega_r^2c^{-2}$. Figure 1a shows the first four harmonics (mode numbers are indicated at the curves) for $\tilde{a} = 1$; Fig. 1b presents the data for m = 1, 2, 3, 5, 8, and 12 in the case of $\tilde{a} = 10$. As can be seen, the greater the waveguide thickness, the faster the frequencies decay with increasing velocity and the greater the difference between adjacent mode frequencies for the same β. For example, when $\beta \approx 1$ and the waveguide radius $\tilde{a} = 1$, the frequencies of harmonics with $m \geq 2$ differ from the resonance value by less than 5%. At the same time, in the waveguide with $\tilde{a} = 10$, only harmonics with $m \geq 14$ fall within this frequency interval.

The energy spent for the excitation of a given harmonic always increases with the velocity of a charged particle. If the velocity is sufficiently large and the waveguide radius is relatively small, the contribution of a given harmonic to the total radiation energy decreases with the mode number. For example, the W_2 value for a particle with $\beta \geq 0.5$ moving in a waveguide with $\tilde{a} = 1$ is one order of magnitude smaller than W_1, while W_3 is several times smaller than W_2 (see Fig. 1a). The field generated by the particle under these conditions is essentially single-mode. In a thick waveguide, the pattern is different. Indeed, for $\tilde{a} = 10$, the first mode is no longer the main one (see Fig. 1b). For example, the mode energies for a particle with $\beta \approx 1$ in this waveguide obey the relations $W_1 < W_2 < W_3 \approx W_4 > W_5 > W_6 > \ldots$. Thus, the field has a complicated multimode character: the 3rd and 4th modes are most significant and a few neighboring modes have comparable energies. With further increase in the waveguide radius, the maximum in this "energy distribution" shifts toward still greater mode numbers.

The above results show the considerable influence of a medium with resonance dispersion on the Vavilov–Cherenkov radiation generated by charged particles moving in waveguides. In practice, as a rule, waveguide structures have axisymmetric vacuum channels (which eliminate polarization energy losses). If the channel radius is not very large, the effects described above will also take place. Detailed description of the Vavilov–Cherenkov radiation process under such conditions falls outside the scope of this paper.

Acknowledgments. The author is grateful to A.D. Kanareikin for fruitful discussion.

REFERENCES

1. B. M. Bolotovskiĭ, Usp. Fiz. Nauk **75**, 295 (1961) [Sov. Phys. Usp. **4**, 781 (1961)].
2. V. P. Zrelov, *Cherenkov Radiation and Its Applications in the Physics of High Energies* (Atomizdat, Moscow, 1968), Chap. 1 [in Russian].
3. V. N. Tsytovich, Izv. Vyssh. Uchebn. Zaved. Radiofiz. **29**, 597 (1986).
4. W. Gai, P. Schoessow, B. Cole, *et al.*, Phys. Rev. Lett. **61**, 2756 (1988).
5. J. G. Power, M. E. Conde, W. Gai, *et al.*, Phys. Rev. ST Accel. Beams **3**, 101302 (2000).
6. A. S. Vardanyan and G. G. Oksuzyan, Zh. Tekh. Fiz. **72** (4), 76 (2002) [Tech. Phys. **47**, 448 (2002)].
7. G. N. Afanasiev and V. G. Kartavenko, J. Phys. D **31**, 2760 (1998).
8. G. N. Afanasiev, V. G. Kartavenko, and E. N. Magar, Physica B **269**, 95 (1999).

Translated by P. Pozdeev

Technical Physics Letters, Vol. 30, No. 7, 2004, pp. 609–611. Translated from Pis'ma v Zhurnal Tekhnicheskoĭ Fiziki, Vol. 30, No. 14, 2004, pp. 75–81.
Original Russian Text Copyright © 2004 by Gavrilov, Il'ichev, Poltoratskiĭ, Rychkov, Dvorkin, Dzbanovsky, Suetin.

Carbon Nanotube Field Emitters for Planar Emission Vacuum Micro- and Nanoelectronics

S. A. Gavrilov, É. A. Il'ichev, É. A. Poltoratskiĭ*, G. S. Rychkov,
V. V. Dvorkin, N. N. Dzbanovsky, and N. V. Suetin
State Research Institute of Physical Problems, Zelenograd, Moscow oblast, Russia
Research Institute of Nuclear Physics, Moscow State University, Moscow, Russia
** e-mail: polt@niifp.ru*

Received January 8, 2004; in final form, March 1, 2004

Abstract—The design and manufacturing technology of carbon nanotube field emitters for novel devices of planar emission vacuum micro- and nanoelectronics are described. Prototypes of diode structures with such emitters are obtained in which the threshold field strength amounts to ~2 V/μm and the direct to reverse current ratio exceeds 10^5. The obtained small scatter of characteristics points to the possibility of creating integrated circuits possessing high operation speed and a working temperature range expanded from –60 to +300°C. *© 2004 MAIK "Nauka/Interperiodica".*

The unique electrophysical properties of carbon nanotubes (CNTs) make them an excellent base for obtaining low-voltage field electron emitters capable of providing an emission current density of up to ~100 A/cm^2. For this reason, extensive effort of several research groups in various countries is devoted to realization of the high potential of CNTs for the development of matrix emitters for flat field-emission displays, high-frequency amplifiers, electron-beam lithography, etc. [1–4]. However, the existing matrix emitters based on CNT arrays still do not possess properties required for the fabrication of high-quality integrated devices. The main disadvantages include (i) low current densities achieved in these devices (in comparison with theoretically possible values), (ii) a strong scatter of emission currents over individual cells in a matrix, (iii) the lack of temporal stability of the characteristics, and (iv) considerable currents via control electrodes (reaching up to 20% of the useful emission current). The last drawback can be removed in some devices [1], but the solution of other problems still encounters considerable difficulties [4].

The aforementioned disadvantages are related for the most part to the design of a CNT emitter typically comprising a conducting square or round substrate bearing CNTs formed by one or another method. CNTs grown on a substrate form a continuous array appearing as a whole body, the emissive properties of which depend on the geometry of the entire array rather than of individual CNTs [3]. There were many attempts to form CNTs in an array so that each nanotube would grow separately from its neighbors. One possible approach consists in using porous oxide bases, but no significant achievements have been reported so far. The main reasons are that the density of pores in such oxides is sufficiently high, real CNTs grow in the pores in an irregular manner and acquire a rather involved shape on emerging from pores [5]. In all devices proposed in the available literature, the CNTs have to be straight, oriented perpendicularly to the substrate on which they are formed, and have identical length and diameters. However, it is impossible to fulfill these conditions in practice. Bending and canting of the nanotubes significantly increase the instability of the emission current [6] and make it necessary to increase the distance between control electrode and emitter and, as a result, to increase the control voltage up to 100 V and above. In addition, the described emitters having vertical design are not suited to planar integral circuits.

This Letter describes a flat CNT emitter of planar design. The general structure is schematically depicted in Fig. 1a. A dielectric substrate *1* bears a three-layer conducting structure *2*–*4* always including layer *3* of a catalytic material (iron, nickel, cobalt, etc.) confined between bottom and top layers *2* and *4* made of a noncatalytic material. All side edges of this three-layer structure, except that facing the anode *6*, are covered by a dielectric material *5*. Then, CNTs *7* are grown on the exposed edge of the catalytic layer *3*. The thickness of layer *3* is controlled in the range from 1 to 20 nm. Being fixed, this layer thickness poses limitations on the diameter of growing CNTs. In contrast to the case of a usual vertical emitter, CNTs in the planar structure have diameters not exceeding the thickness of catalytic layer *3*. The formation and local growth of CNTs in this structure is described in more detail in the proceedings of recent international meetings and conferences [7–9].

In the proposed emitter design, the dense growth of CNTs does not strongly limit the emissive properties of

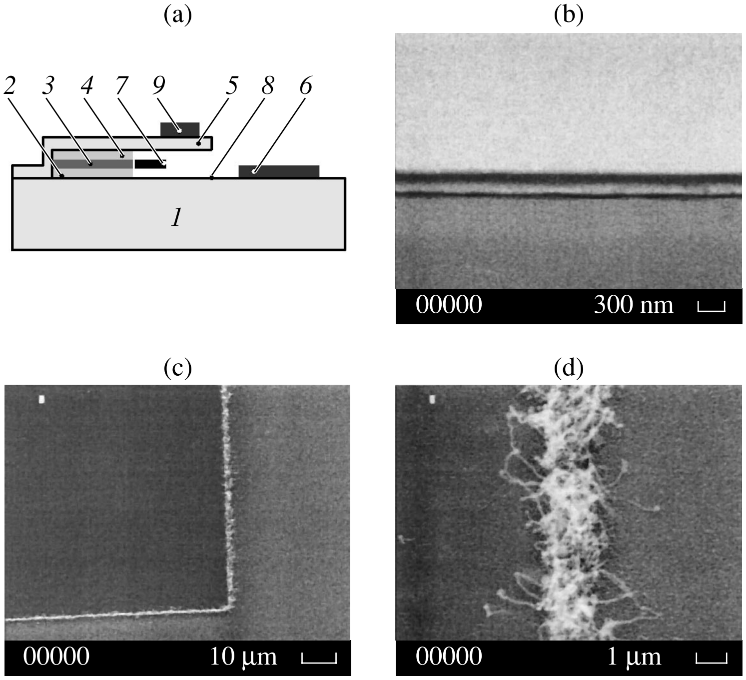

Fig. 1. Planar CNT field emitter design: (a) schematic diagram (see the text for explanations); (b–d) electron-microscopic images of (b) emitter and (c, d) test structures on different scales.

the device, since CNTs form a thin "blade" with a length equal to 10–25 thicknesses of layer *3* (this provides for amplification of the electric field strength near the blade edge). In order to favor the directional growth of CNTs in the plane of the catalytic layer *3*, this layer can be selectively etched from the edge side. In this case, the growing CNTs initially lie in the plane of layer *3*; subsequently, the CNT blade protruding out of the edge retains the growth direction over a length within ~10 thicknesses of the catalytic layer. If the CNT length exceeds this limiting value, the blade becomes a "fringe" composed of CNTs. For a catalytic layer thickness above 40 nm and a CNT length of ~3–10 μm, this fringe can be readily observed, representing a plurality of nanotubes emerging from the edge. The CNT diameter can be readily evaluated and compared to the catalytic layer thickness with the aid of a usual electron microscope. We have used structures with a catalytic layer thickness above ~40 nm and a CNT length of ~5–10 μm as the test samples for controlling the normal CNT formation regime.

For extending the functional possibilities of CNT emitters, the three-layer conducting structure is covered with insulator *5* (Fig. 1a) and (prior to CNT growth) etched from the open face *8*. After this pretreatment, it is possible to obtain a structure of the vacuum triode type. To this end, a gate *9* is formed on the dielectric surface by means of the standard electron-beam lithography or photolithography. In this structure, the anode and gate may be spaced from the CNT blade edge by a distance ranging from a fraction of a micron to several microns. Thus, it is possible to proceed with developing vacuum micro- and nanoelectronic devices.

The proposed CNT field emitter design was realized in a diode variant (Fig. 1a, without gate *9*). Layers *2* and *4* (20 nm thick) were made of vanadium and the catalytic layer *3* (20 nm thick) was made of nickel. The nickel layer thickness was checked by means of atomic force microscopy (AFM). For this purpose, the nickel layer formed in the diode structure was simultaneously deposited onto a control silicon substrate. Then, a nickel/silicon step was formed by lithographic techniques and measured by AFM to within ±1 nm. The CNTs were grown by chemical vapor deposition [7–9].

Figure 1b shows an electron-microscopic image of the typical CNT field emitter, in which the CNT blade is clearly manifested as a bright band on a dark shadow area formed by the upper edge layer and nanotubes. Estimates of the blade thickness from these data with allowance of the experimental conditions give ~0.2 μm. Figures 1c and 1d show images of the test structure measured at different magnifications. As can be seen, CNTs are actually formed only on the edge where the catalytic layer emerges. In the test structure, the grown objects possess sufficiently large length and diameter (see Fig. 1d) to be identified as CNTs. The nanotubes have approximately the same diameters estimated at 40 nm, which coincides with the thickness of a catalytic layer used in these test structures.

We have measured the current–voltage characteristics of four CNT field emitters, each having a length of 500 μm, situated on the edges of a square with a side

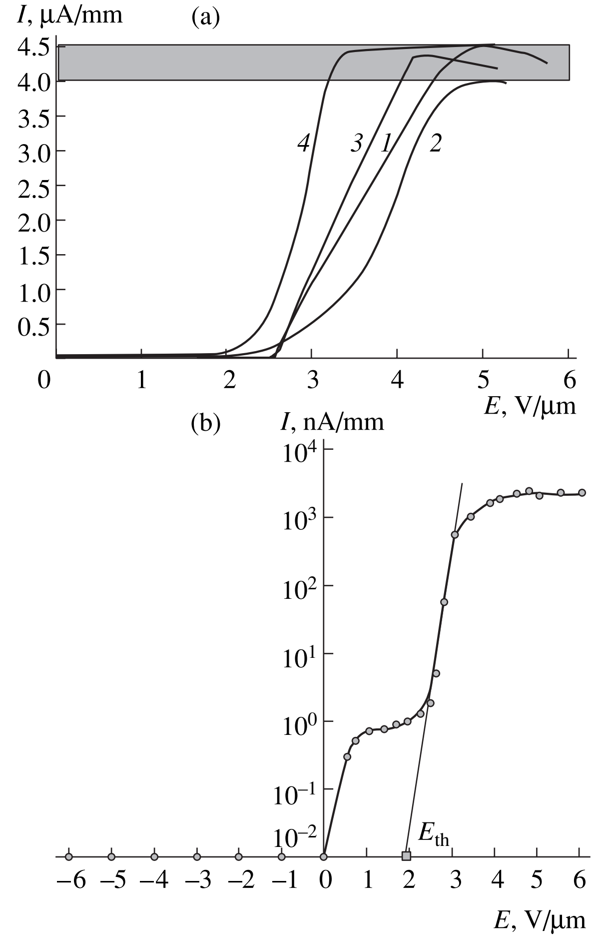

Fig. 2. Plots of the emission currents versus applied field strength for (a) four CNT field emitters in a common base structure and (b) one CNT field emitter illustrating determination of the threshold field strength E_{th}.

length of 5 mm. The scatter of emission currents at an applied field strength of 5 V/μm was ±0.25 μA/mm for an average value of 4.25 μA/mm (Fig. 2a). This scatter is sufficiently small that makes it a quite realistic task to develop a technology of integrated CNT field emitters on an area exceeding 1 cm^2. Another important characteristic of field emitters in diode structures is the direct to reverse current ratio. Figure 2b shows a plot of the specific (linear) emission current versus applied field strength (varied from –6 to +6 V/μm) for a 500-μm-long CNT field emitter. As can be seen, the threshold voltage in this case is about E_{th} ~ 2 V/μm and the direct to reverse current ratio exceeds 10^5, which is much greater than the corresponding values known in usual semiconductor devices.

Taking into account these properties of CNT field emitters, such devices can be used for the creation of programmable ROM of a high capacity (~10^{12} bit) capable of operating at a readout rate of ~100 Mbit/s in a temperature range from –60 to +300°C. Such a ROM design comprises two systems of mutually perpendicular buses, one of which bears CNT field emitters formed as described above. The data are written by applying bias voltage to a memory cell where logical zero has to be written. At a field strength of ~10–20 V/μm, the nanotubes are decomposed and the current is not conducted through the given cell at usual voltages creating a field of ~5 V/μm.

Another interesting possible application of field CNT emitters is the development of flat thin (with a thickness not exceeding 1 mm) color displays with a pixel size of 15 × 50 μm.

Acknowledgments. This study was supported in part by the NATO “Science for Peace” Program (grant SfP-974354) and the Federal Program “Physics of Solid State Nanostructures.”

REFERENCES

1. David S. Y. Hsu, Appl. Phys. Lett. **80**, 2988 (2002).
2. D. Li and J. Zhang, J. Vac. Sci. Technol. B **19**, 1820 (2001).
3. J. I. Sohn and S. Lee, Appl. Phys. A **74**, 287 (2002).
4. J. K. Ha, B. H. Chung, S. Y. Han, *et al.*, J. Vac. Sci. Technol. B **20**, 2080 (2002).
5. T. Iwasaki, T. Motoi, and T. Den, Appl. Phys. Lett. **75**, 2044 (1999).
6. L. Wang, R. P. Gao, W. A. Heer, *et al.*, Appl. Phys. Lett. **80**, 856 (2002).
7. V. V. Dvorkin, N. N. Dzbanovsky, E. A. Poltoratsky, *et al.*, in *Proceedings of the 203rd ECS Meeting, Paris, 2003*, PV 2003-15<ISBN1-56677-397-0> *Fullerenes*, Vol. 13: *Fullerenes and Nanotubes: The Building Blocks of Next Generation Nanodevices*, pp. 405–410.
8. S. A. Gavrilov, N. N. Dzbanovsky, V. V. Dvorkin, *et al.*, in *Proceedings of the 11th International Symposium “Nanostructures: Physics and Technology,” St. Petersburg, 2003*, pp. 234–236.
9. S. A. Gavrilov, N. N. Dzbanovsky, V. V. Dvorkin, *et al.*, in *Proceedings of the International Conference “Micro- and Nanoelectronics,” Moscow–Zvenigorod, 2003*, O1-27.

Translated by P. Pozdeev

Technical Physics Letters, Vol. 30, No. 7, 2004, pp. 612–614. Translated from Pis'ma v Zhurnal Tekhnicheskoĭ Fiziki, Vol. 30, No. 14, 2004, pp. 82–88.
Original Russian Text Copyright © 2004 by Kuksenko, Makhmudov.

Effect of Mechanical Stress on the Polarization of Natural Dielectrics (Rocks)

V. S. Kuksenko* and Kh. F. Makhmudov
Ioffe Physicotechnical Institute, Russian Academy of Sciences, St. Petersburg, 194021 Russia
** e-mail: victor.kuksenko@mail.ioffe.ru*

Received March 3, 2004

Abstract—A sample of marble not possessing piezoelectric properties was subjected to uniaxial compressive loading and the response electric field potential was measured by a contactless method using a high-sensitivity electrometer. In the second experiment, weak electric potentials were applied via special electrodes to the opposite sides of the sample subjected to the same mechanical load. The electric potentials measured under the conditions of mechanical loading significantly change upon weak electrostatic polarization of the sample. *© 2004 MAIK "Nauka/Interperiodica".*

Electromechanical phenomena in natural dielectrics are not only of purely basic interest but can be of considerable practical significance in the context of investigations of the electromagnetic precursors of earthquakes [1–3]. In addition, this knowledge may help us understand the nature of physical processes involving high-power response to weak actions (e.g., electromagnetic response to seismic activity) [4] and some special states of solids [5, 6]. Previously [7], it was demonstrated that the appearance of an electric field in the course of mechanical loading of solid dielectrics has much in common with their polarization in weak electric fields.

We have studied the effect of mechanical stress on the polarization of solid dielectrics in weak electric fields. For the sake of simplicity, the electric potential measured in a mechanically loaded sample will be referred to as mechanoelectric potential (MEP), in contrast to the electric potential (EP) observed in the case of usual polarization of a sample in the electric field. This Letter reports on the results of investigation of the MEP of marble samples. This mineral, possessing all the main properties of solid dielectrics, is widely used in laboratory investigations. Another circumstance important for our experiments is that marble does not possess piezoelectric properties.

A prismatic sample of marble with dimensions 40 × 40 × 100 mm was loaded via insulating spacers in a hydraulic press. Electrodes made of an epoxy resin filled with silver powder (which allowed the contact potential difference to be significantly reduced) were fixed on the opposite side faces and connected to a source of dc voltage or to the ground. The electric field potential (both EP and MEP) in the sample was measured by a contactless method with the aid of a special high-sensitivity electrometer. The electrometer probe was fixed on a holder with a micrometric screw drive for scanning along the sample surface at a 2-mm-wide gap between the sample surface and the probe.

Uniaxial compression of a marble sample gives rise to an induced MEP field. In the absence of a mechanical load, a potential difference applied to electrodes leads to polarization of the sample. The induced EP field is symmetric relative to the middle of the sample, so that it is possible to determine the sample surface regions possessing positive and negative potentials.

Figure 1 shows the pattern of MEP and EP variation in the course of sequential measurements performed at a fixed position of the electrometer probe. At the time moment t_1, a uniaxial load P amounting to 0.3 of the breaking limit was applied to the sample for a very short time and immediately removed. During this impulse, a positive MEP value ($+F_m$) was measured. At the time moment t_2, a potential difference of 2 V was applied to the electrodes with a polarity selected so that the EP ($+F_e$) measured by the probe would have the same (i.e., positive) sign as that of MEP in the first measurement. When the F_e value attained a stationary level (in the time interval from t_2 to t_3), the sample was subjected to the same loading impulse. In the polarized sample, the MEP acquired an increment ΔF. The total potential (EP + MEP) will be denoted $+\Psi$. Upon unloading, the sample potential changed back from $+\Psi$ to $+F_e$. At the time moment t_4, the applied dc voltage was switched off and the electrodes were grounded for some time to provide for electric neutralization of the sample.

At the time moment t_5, the same voltage (2 V) was applied to the sample but in the opposite polarity. The electrometer probe measured a negative response EP attaining a stationary level $-F_e$. Then, the sample was again uniaxially loaded by the same impulse (at $t = t_6$). The MEP value measured by the probe was decreased by ΔF and the total potential was $-\Psi$. Upon unloading, the potential was restored on a level of $-F_e$. Eventually, the dc voltage was switched off and the electrodes were grounded to neutralize the sample. The entire procedure was repeated with stepwise increase either in the mechanical load (at a constant applied dc voltage) or in the potential difference between electrodes.

Figure 2a shows the plots of MEP (F_m) versus load in various polarization states. Curve *1* was obtained in the absence of polarization, curve *2* corresponds to the same polarity of responses to the electric (EP) and mechanical (MEP) polarization (F_e and F_m have the same signs), and curve *3* reflects the case of opposite EP and MEP signs. As can be seen, all three dependences are linear but exhibit different slopes.

Formally, the results can be considered by introducing an electromechanical modulus θ (analogous to the piezoelectric modulus):

$$\theta = \Delta F_m / \Delta P.$$

It should be noted that this quantity is by no means an absolute characteristic of the sample material, since it depends on the probe type and geometry, the distance from probe to sample, and some other parameters. Nevertheless, the relative variation of θ may objectively characterize the influence of mechanical loading on the MEP in the presence of electric polarization. We can ascertain that the electromechanical modulus increases when the EP and MEP signs coincide and decreases when their polarities are opposite.

Figure 2b shows the plot of MEP measured for the same mechanical load in the course of variation of the magnitude and sign of electric polarization. We can distinguish three regions in the observed dependence. The intercept with the ordinate axis corresponds to the MEP value at $F_e = 0$. Region *1* reflects the sample behavior for the electric and mechanical polarization of the same sign. In this region, the sample response to a fixed load (i.e., the electromechanical modulus) is greater. In regions *2* and *3*, the responses to electric and mechanical polarization have opposite signs. As a result, the modulus decreases and, under certain conditions, the sample is "insensitive" to mechanical loading. It is interesting to note that, as the negative potential of the polarizing electric field increases in absolute value above F^*, the mechanical loading leads to the appearance of a negative response potential. Therefore, the fields of electric and mechanical polarization are involved in a rather complex interaction.

Figure 1 shows that there is another characteristic of the observed phenomenon, which is especially important from the practical standpoint. When the EP and MEP polarities coincide, the total potential Ψ increases upon loading (this corresponds to the upper part of Fig. 2b). For the opposite polarities (the lower part of

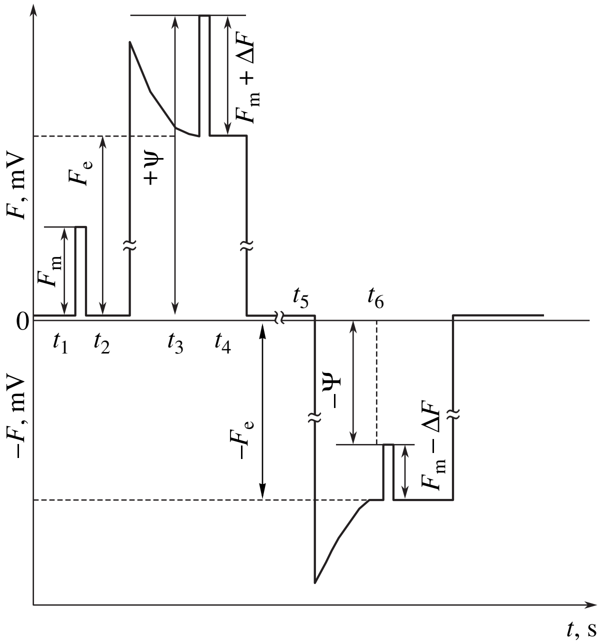

Fig. 1. The pattern of MEP and EP variation under the action of mechanical and electric fields applied to the sample studied (see the text for explanations).

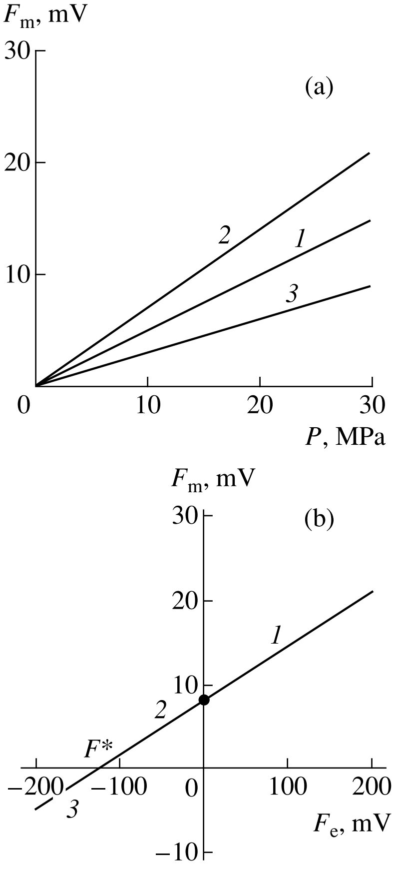

Fig. 2. Plots of the MEP versus (a) the mechanical compressive stress and (b) magnitude and sign of the electric potential.

Fig. 2b), the total potential Ψ decreases upon loading. Let us consider the behavior of the sum

$$\psi = F_e + F_m.$$

The parameter ψ, obtained by summing the response potentials during simultaneous action of the mechanical load and the electric field for the same values and opposite signs of the applied voltage, is equal to the sum of potentials measured under the applied load. The dependence of ψ on the load is linear, representing the sum of two linear functions (plots *2* and *3* in Fig. 2a). The ψ value weakly depends on the electric polarization. As the polarizing electric field increases, the slope of line *2* increases and that of line *3* decreases, which makes this dependence useful for determining unknown mechanical stresses (e.g., in rock masses). Difficulties in the evaluation of mechanical stresses by this method are related to relaxation of the MEP value [7]. For this reason, the proposed approach is probably more suited for determining changes in the mechanical stresses, which is also of considerable importance for the prognosis of dynamic manifestations of a macroscopic fracture (in particular, during the active development of the earthquake focus).

The above results provide convincing evidence of the interaction of responses to mechanical (MEP) and electric (EP) polarization. This interaction has a quite complex nature, not being restricted to trivial addition of the field potentials. Phenomenological investigations performed in our study cannot provide for a deep insight into this phenomenon. It is probably necessary to develop a theoretical microscopic model for materials possessing a simpler structure. Nevertheless, even this study allows some useful practical conclusions to be made, in particular, concerning controlled modification of the electromechanical modulus of solid dielectrics and evaluation of the mechanical stresses and their variation in loaded solids. Such estimates can be useful for the interpretation of electromagnetic precursors of large-scale fracture events, including mountain shocks and earthquakes.

Acknowledgments. This study was supported by the Russian Foundation for Basic Research (project nos. 01-05-64893, 02-05-08003-INNO), and 02-05-39017-GFEN) and the International Scientific-Technological Center (grant no. 1745).

REFERENCES

1. D. A. Lockner, J. D. Byerlee, V. S. Kuksenko, and A. V. Ponomarev, PAGEOPH **123**, 601 (1986).
2. V. S. Kuksenko, R. Sh. Kil'keev, and M. I. Miroshnichenko, Dokl. Akad. Nauk SSSR **260**, 841 (1981).
3. G. A. Sobolev, *Fundamentals of the Prediction of Earthquakes* (Nauka, Moscow, 1993) [in Russian].
4. N. T. Tarasov, Dokl. Akad. Nauk **353**, 542 (1997).
5. E. G. Fateev, Zh. Tekh. Fiz. **71** (1), 92 (2001) [Tech. Phys. **46**, 89 (2001)].
6. E. G. Fateev, in *Proceedings of the 10th International Conference of the Physics and Chemistry of Ice, St. Johns, Newfoundland, Canada, 2002*, pp. 14–15.
7. V. S. Kuksenko, Kh. V. Makhmudov, and A. V. Ponomarev, Fiz. Tverd. Tela (St. Petersburg) **39**, 1202 (1997) [Phys. Solid State **39**, 1065 (1997)].

Translated by P. Pozdeev

Technical Physics Letters, Vol. 30, No. 7, 2004, pp. 615–617. Translated from Pis'ma v Zhurnal Tekhnicheskoĭ Fiziki, Vol. 30, No. 14, 2004, pp. 89–94.
Original Russian Text Copyright © 2004 by Sosnin, Lavrent'eva, Masterova, Erofeev, Tarasenko.

Bactericidal Iodine Lamp Excited by Capacitive Discharge

**É. A. Sosnin, L. V. Lavrent'eva, Ya. V. Masterova,
M. V. Erofeev, and V. F. Tarasenko**
Institute of High-Current Electronics, Siberian Division, Russian Academy of Sciences, Tomsk, Russia

Received January 12, 2004

Abstract—A new capacitive discharge lamp is created in which the main contribution to the output radiation is due to the iodine atomic emission line at 206 nm. The lamp has an average output power at λ = 206 nm reaching 6 W, an efficiency of 8% (with respect to the electric energy supplied to the discharge), and a working life exceeding 1700 h. The results of tests on *Escherichia coli* and *Staphylococcus aureus* bacterial cultures reliably confirmed the bactericidal action of radiation of the proposed lamp. *© 2004 MAIK "Nauka/Interperiodica".*

In recent years, there has been considerable progress in the technology of short-wavelength spontaneous radiation sources operating in the UVB (200–280 nm) and VUV (100–200 nm) spectral ranges, which find application in photochemistry, ecology, medicine, and photobiology [1, 2]. Most widely used are excimer lamps [3, 4] excited by electric discharges of various types. The main requirements to such sources requires imposed by practical applications include long working life and high stability of the output radiation power. The working life of glow-discharge excimer lamps can be increased up to several hundred hours by replacing chlorine by bromine- or iodine-containing working gas medium [5, 6]. Recently [7], it was reported that further increase up to several thousand hours can be achieved by using a barrier discharge. Comparable working life is provided by excitation of an inert gas–halogen mixture using a capacitive discharge scheme originally proposed in [8] and recently developed in [9–12]. As was pointed out in [3], good prospects for practical applications are offered by iodine vapor discharge lamps capable of simultaneously radiating at 206 and 253 nm and in the VUV range [13]. The chemical inertness of iodine must ensure a very long working life of such radiation sources.

This Letter presents the working characteristics of a new radiation source operating on iodine vapor excited by the capacitive discharge. We also report on the results of experimental evaluation of the bactericidal effect of this lamp.

The lamp bulb is made of a quartz tube with a diameter of 4 cm and a length of 30 cm. The optical transmission of quartz at a wavelength of 200 nm is 75%. The electrodes placed on the external surface of the quartz tube formed a 22-cm-long discharge gap. The lamp was powered by a high-frequency (130 kHz) bipolar meander with an amplitude of several kilovolts, sufficient to provide for stable breakdown of the discharge gap. The lamp power supply scheme was analogous to that described in [9]. The power supply unit consumed no more than 100 W for the typical current through discharge gap not exceeding 40 mA.

The current and voltage in the discharge tube were measured using a shunt and a voltage divider, respectively, and a double-beam oscillograph of the TDS-220 type. The electric power supplied to the discharge was determined as described in [3]. The average output power was determined as described in [14], using a vacuum photodiode of the FEK-22SPU type possessing known spectral sensitivity in the UV spectral range. The output radiation spectrum was measured with a setup comprising a monochromator (MDR-23, L = 1.3 nm/mm), a wideband photomultiplier (FEU-100), an oscillograph (TDS-3032), and a computer.

The discharge tube was filled with iodine vapor at a pressure not exceeding 1–2 Torr. Figure 1 shows the typical spectrum of radiation excited in this working medium under the conditions described above. As can be seen, the spectrum contains the iodine atomic emission line at 206 nm and a molecular band of I_2^* dimer peaked at 342 nm whose contribution to the total radiation power under these excitation conditions is rather insignificant. The average output power at λ = 206 nm reached 6 W at an efficiency of 8% (with respect to the electric energy supplied to the discharge). The lamp operated for more than 1700 h without visible decrease in the output intensity. Recently, Shuaibov *et al.* [6] reported on an excimer lamp using a Xe–I working mixture, which also exhibited intense iodine atomic emission line at 206 nm in addition to the $B \longrightarrow X$ emission bands of XeI* (253 nm) and I_2^* (342 nm). Judging by the data reported in [6], the UV output power at λ = 206 nm was 3–3.5 W and the efficiency in the entire emission band of 206–342 nm did not exceed 5%, while the working life in the static gas phase oper-

1063-7850/04/3007-0615$26.00 © 2004 MAIK "Nauka/Interperiodica"

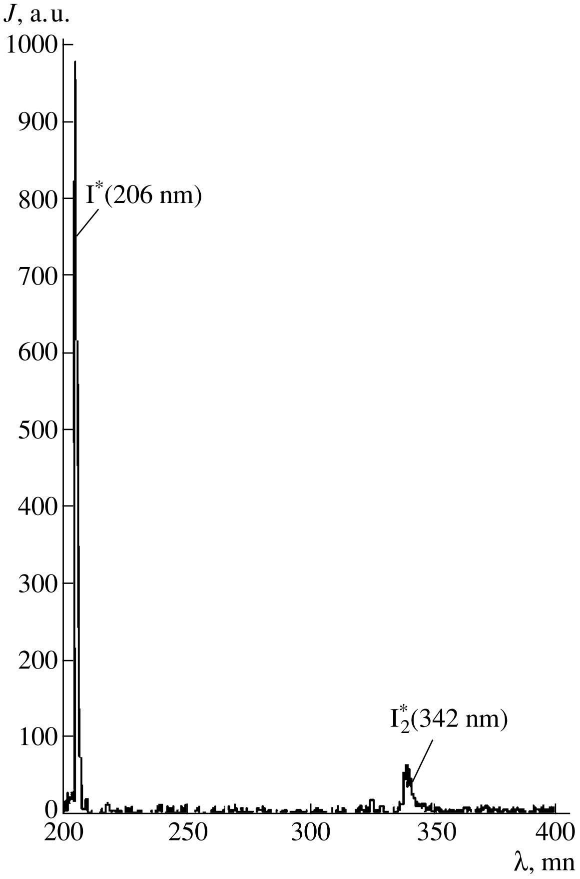

Fig. 1. Output radiation spectrum of the iodine lamp excited by capacitive discharge.

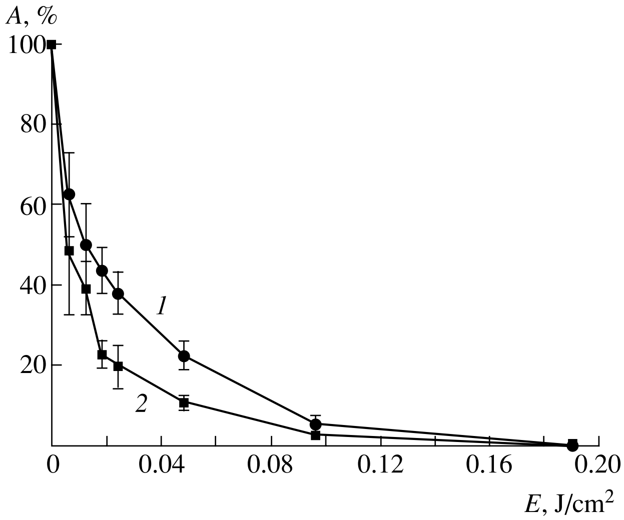

Fig. 2. Percentage survival *A* of (*1*) *E. coli* and (*2*) *Sr. aureus* cultures exposed to various doses *E* of radiation of the iodine lamp excited by capacitive discharge.

ation regime was not less than 300 h. It can be seen that, with respect to all these parameters, our iodine lamp excited by capacitive discharge is superior to the source described in [6].

It should also be noted that the lamp described in [6] was called bactericidal, although no results were presented for the action of its radiation on microbial species. On the one hand, the strong emission line of I* (206 nm) actually falls within the so-called bactericidal spectral range (traditionally defined as 200–310 nm). This radiation is strongly absorbed by both purine [adenine (A), guanine(G)] and pyrimidine [cytosine (C), thymine (T), uracil (U)] nucleotide bases, thus producing various disorders in the DNA structure and inhibiting the multiplication of microbes. An analysis shows that the effect of radiation in the bactericidal spectral range is primarily related to the formation of T–T, T–C, and C–C dimers (listed in the order of occurrence) in the DNA structure [15]. On the other hand, it is known that the photodimerization of thymine (T–T) can be reversible: the radiation with $\lambda < 280$ nm provides for the predominance of photodimerization, while the radiation with $\lambda > 250$ nm favors monomerization, so that both reactions proceed in the wavelength interval within $\lambda = 260$–280 nm. This circumstance has to be taken into account in the development of bactericidal lamps: the output radiation spectrum should contain the components favoring inactivation processes, while the components favoring the UV-induced DNA repair should be excluded as much as possible. From this standpoint, any lamp with long-wavelength components in the output radiation spectrum proposed for use as a source of bactericidal energy has to be experimentally tested for the action upon microorganisms.

We have assessed the bactericidal effect of the new capacitive-discharge iodine lamp by the method used previously for verification of the antibacterial action of excimer lamps operating on the $B \longrightarrow X$ emission bands of KrCl* (222 nm), XeCl* (308 nm), and XeBr* (283 nm) [16, 17]. The tests were performed on standard strains of *Escherichia coli* and *Staphylococcus aureus*. As is known, *E. coli* is characterized by the minimum sensitivity (among enterobacter species) to various factors and is considered as an important test object for evaluation of the sanitary-epidemiological state of the environment. The species of *St. aureus* are characterized by high adaptability to unfavorable conditions (due to the fast conjugation between cells) and are also widely used as test objects for evaluation of the effect of various disinfecting agents and antibiotics on Gram-positive bacteria.

The bacterial cultures were grown in meat-infusion agar medium. The optimum concentration of microbial species for the tests was determined preliminarily by method of double serial dilutions. In the main test, microbial cultures plated on glass substrates were exposed to the output radiation of the iodine discharge lamp for various periods of time. The radiation power density in all tests was 3.2 mW/cm^2. The test with each exposure was repeated four or five times. The plates with unirradiated cultures were used as the control samples. After exposure, the samples were incubated in a thermostat at 37°C for two days. The survival of test microbes was determined on the third day by counting techniques.

Figure 2 shows the curves of survival for the test cultures irradiated to various doses. As can be seen, an exposure of ~190 J/cm^2 leads to the complete loss of both bacterial species. Thus, the radiation of our iodine lamp excited by the capacitive discharge produces a pronounced bactericidal effect.

Thus, we have created a new source of bactericidal radiation with a high working life (above 1000 h), an average output power of 6 W, and an efficiency of 8%.

Acknowledgments. The authors are grateful to M.I. Lomaev, A.A. Lisenko, D.V. Shitts, and V.S. Skakun for technical support.

This study was supported by the International Scientific-Technological Center, project no. 1270.

REFERENCES

1. T. Oppenländer, *Photochemical Purification of Water and Air* (Wiley-VCH, Weincheim, 2003).
2. É. A. Sosnin, in *Proceedings of the 2nd Integration Interdisciplinary Conference of Young Scientists SO RAN and Students "Scientific Schools of Siberia: A Look to the Future"* (Izd. Inst. Geogr. SO RAN, Irkutsk, 2003), pp. 150–157.
3. M. V. Lomaev, V. S. Skakun, É. A. Sosnin, *et al.*, Usp. Fiz. Nauk **173**, 201 (2003).
4. I. W. Boyd, J.-Y. Zhang, and U. Kogelschatz, *Photo-Excited Processes, Diagnostics and Application* (Kluwer, Netherlands, 2003), Chap. 6, pp. 161–199.
5. M. I. Lomaev and V. F. Tarasenko, Proc. SPIE **4747**, 390 (2002).
6. A. K. Shuaibov, L. L. Shimon, and I. A. Grabovaya, Pis'ma Zh. Tekh. Fiz. **29** (20), 77 (2003) [Tech. Phys. Lett. **29**, 871 (2003)].
7. I. W. Boyd and J.-Y. Zhang, Appl. Surf. Sci. **168**, 296 (2003).
8. M. I. Lomaev, V. S. Skakun, É. A. Sosnin, *et al.*, Pis'ma Zh. Tekh. Fiz. **25** (21), 27 (1999) [Tech. Phys. Lett. **25**, 858 (1999)].
9. É. A. Sosnin, M. V. Erofeev, V. F. Tarasenko, and D. V. Shitts, Prib. Tekh. Éksp., No. 6, 118 (2002).
10. É. A. Sosnin, M. V. Erofeev, A. A. Lisenko, *et al.*, Opt. Zh. **69** (7), 77 (2002).
11. M. V. Erofeev, É. A. Sosnin, V. F. Tarasenko, and D. V. Shitts, Opt. Atmos. Okeana **13**, 862 (2000).
12. M. I. Lomaev, V. S. Skakun, É. A. Sosnin, and V. F. Tarasenko, RF Patent No. 2154323 C2, Byull. Izobret., No. 22 (2000).
13. J.-Y. Zhang and I. W. Boyd, Appl. Phys. B **71**, 177 (2000).
14. A. N. Panchenko and V. F. Tarasenko, Opt. Spektrosk. **84**, 389 (1998) [Opt. Spectrosc. **84**, 337 (1998)].
15. N. Giese and J. Darby, Water Res. **34**, 4007 (2000).
16. É. A. Sosnin, L. V. Lavrent'eva, M. R. Yusupov, *et al.*, in *Proceedings of the 2nd International Workshop on Biological Effects of Electromagnetic Fields, Rhodes, 2002*, pp. 953–957.
17. É. A. Sosnin, L. V. Lavrent'eva, Ya. V. Masterova, and V. F. Tarasenko, Patent Appl. No. 2001122943/13(024355), Russia.

Translated by P. Pozdeev